

Numerical Simulation Of Guided Waves In Thin Walled Composite Structures

by

Kalyan Sreenivas Nadella

A dissertation submitted in partial fulfillment
of the requirements for the degree of
Doctor of Philosophy
(Aerospace Engineering)
in the University of Michigan
2014

Doctoral Committee:

Professor Carlos E. S. Cesnik, Chair
Professor Daniel J. Inman
Associate Professor Jerome P. Lynch
Professor Anthony M. Waas

©Kalyan Sreenivas Nadella

2014

Dedication

To my parents.

Acknowledgments

Concluding my doctoral studies represents the completion of a significant part of my life's journey. This journey was made possible with the support and encouragement of many wonderful individuals.

I would first like to thank my mentor and advisor, Prof. Carlos E. S. Cesnik, for his patience and thoroughness in molding me into a scientific researcher. I am sincerely grateful for all the opportunities he has provided, including my first research opportunity in graduate school back in 2008. I have learned a lot from him about conducting research, and also about life in general, over the past 5 and half years, and I still believe that I have more to learn from him. He has always been cooperative and supportive of my goals and ambitions, and he allowed me to develop my skills at my own pace. His attention to research and presentation detail drove me to improve in a multitude of ways. I would also like to thank Prof. Daniel J. Inman, Prof. Jerome P. Lynch, and Prof. Anthony M. Waas for taking time out of their busy schedules to be on my committee and providing me with the valuable feedback and suggestions pertaining to my dissertation and research.

I will be forever indebted to my parents for all their support, encouragement and blessings over the years. I would never have reached this milestone without their love, passion and sacrifice to ensure my academic success. Today, they are really proud of me for being the first in my family to successfully attempt and complete a Ph.D. I would also like to thank my family members for their support and encouragement throughout my education.

I would like to recognize the many individuals that have helped me in developing my dissertation. First, Dr. Ken Salas (now at GE Global Research) was my Jedi Master; he taught me the ways of the Force (guided wave fundamentals, and experimental and manufacturing techniques). I could always count on him to provide me with insightful suggestions related to my research, and to be a supportive teacher and friend during my graduate life. Additionally, I would like to acknowledge him for conducting many of the experiments presented in this dissertation. Maj. Matt Obenchain was helpful in proofreading my manuscripts and participating in insightful discussions during the development of the numerical framework. Dr. Devesh Kumar (now at MSC Software) gave me valuable advice and company in the laboratory. I would also like to acknowledge him and Dr. Pavana

Prabhakar (now at UTEP) for their friendship, support and enjoyable memories during my graduate studies. I am also grateful for the support and intellectual inspiration I have obtained from various members of A²SRL during my doctoral studies. I would also like to thank numerous friends and colleagues at the Aerospace Department and in the Aero-lunch group for their support over the years. I would also like to thank Prof. Philip Roe and Dr. Marco Ceze for their valuable suggestions regarding some of the numerical studies.

On a personal level, I would also like to thank my housemates for 4 years, Dr. Srinivasa Siddhartha Nadukuru and Dr. Ravi Ranade, for their friendship, support and advice. My stay at Michigan was fortuitous because I met Qixin He, and I would like to thank her for the unwavering support and encouragement when I needed it the most and for nursing me through my knee surgeries. I would also like to thank Kate Meyer for being a wonderful friend, and editing my dissertation manuscript. I would also like to take this opportunity to thank some of the great friends for all the wonderful memories that I will cherish for the rest of my life. Living in student cooperative housing has provided me with a wonderful opportunity to meet students from various backgrounds and fields of study, which extended my social and intellectual horizons. Additionally, I am grateful to my numerous Indian and Brazilian friends that have made my graduate life more enjoyable and less stressful.

I would also like to express my gratitude to all the engineering and administrative staff members at the Aerospace Department, especially, Denise Phelps, Tom Griffin, Dave McLean and Suzanne Smith for all their help and support in numerous areas of my graduate life. They helped make it a pleasant experience.

The work presented in this dissertation was supported in part by the NASA University Institutes Project/ Lightweight Spacecraft, Structures, and Materials Program under grant Z634001. Ms. Claudia Meyer and Dr. Mark Shuart were the program managers. This work was also sponsored by the National Rotorcraft Technology Center (NTRC) Vertical Lift/Rotorcraft Center of Excellence (VLRCOE) at the University of Michigan with Mr. Mahendra J. Bhagwat as the technical monitor. I am grateful for the financial support provided by these agencies.

TABLE OF CONTENTS

Dedication	ii
Acknowledgments	iii
List of Figures	vii
List of Tables	xii
List of Abbreviations	xiii
List of Symbols	xv
Abstract	xvii
Chapter	
1 Introduction	1
1.1 Structural Health Monitoring	1
1.2 Waves and Structural Health Monitoring	3
1.2.1 Waves	3
1.2.2 Lamb Waves	4
1.2.3 Guided Waves for Structural Health Monitoring	4
1.2.4 Guided-wave Generation	5
1.3 Modeling Guided Waves	7
1.3.1 Analytical and Semi-analytical Modeling	7
1.3.2 Numerical Modeling	8
1.3.3 Local Interaction Simulation Approach	10
1.4 Research Objectives and Dissertation Overview	12
2 Theoretical Formulation	14
2.1 Original Formulation	14
2.2 UM-LISA Formulation: Layered Composite Laminates	15
2.2.1 Equations of Motion	16
2.2.2 Discretization	18
2.2.3 Finite Difference Transformations and Sharp Interface Model	20
2.2.4 Guided Wave Generation in Prescribed Displacement LISA	27
2.3 UM-LISA: Piezo-coupled Formulation	29
2.3.1 Governing Equations	30

2.3.2	Discretization, Finite Difference Transformations, and Sharp Interface Model	33
2.3.3	Guided Wave Generation in UM-LISA	40
2.4	Modeling for Guided Wave Sensing in UM-LISA	41
2.4.1	Basic Strain-based Sensor Modeling	41
2.4.2	Direct Piezo Coupled Field Modeling	43
3	Numerical Framework	45
3.1	Development	45
3.2	Architecture	47
3.2.1	Model Initialization	47
3.2.2	Pre-processing	49
3.2.3	Iterative Equations	52
3.2.4	Post-processing	53
4	Grid Convergence Studies	55
4.1	Effects of Spatial and Temporal Discretizations	55
4.2	Rate of Convergence	61
4.3	Convergence Error	63
4.3.1	Point Source Actuation	64
4.3.2	Piezo Actuation	65
4.3.3	Air Layer Error	70
4.4	Guidelines for Discretization Parameters	72
5	Numerical and Experimental Studies	74
5.1	Anisotropic Effects in Composite Laminates	74
5.1.1	Experimental Test Specimens	74
5.1.2	Experimental Setup	75
5.1.3	Simulation Parameters	77
5.1.4	Phase Slowness Diagrams	79
5.1.5	Piezoceramic Disk Actuator	79
5.1.6	CLOVER Actuator	83
5.1.7	Preliminary GW Studies in Sandwich Foam Core Panels	88
5.2	Simulated Damage: Concentrated Mass	91
5.3	Wave Generation Modeling	99
5.3.1	Displacement Behavior of Actuator Nodes	99
5.3.2	Validation of GW Generation	104
5.4	Frequency Response for Piezoelectric Sensor	110
6	Concluding Remarks	114
6.1	Summary	114
6.2	Key Contributions	117
6.3	Recommendations for Future Work	118
	Appendix	120
	Bibliography	127

LIST OF FIGURES

Figure

1.1	Distribution of defects on a UH-60 airframe during condition evaluation cycle [3].	3
1.2	Different transducers used for wave generation.	6
2.1	Overview of Local Interaction Simulation Approach (LISA)’s original formulation as presented in Ref. [92].	15
2.2	Overview of LISA’s theoretical formulation (orange colored blocks on the right and left represent the new implementation aspects to the basic formulation).	16
2.3	Schematic diagram showing the discretization in a three-dimensional (3D) LISA formulation. The black dots represent the nodes, and the cuboid between eight dots represents a unit cell.	19
2.4	A generic point C at location (i,j,k) with eighteen nearest neighbors and the Cartesian system used in the analysis.	20
2.5	For a generic point C at location (i,j,k) , (a) blue dots represent the 8 points chosen to enforce displacement continuity, and (b) additional points shown as black squares are used to enforce stress continuity conditions.	21
2.6	PZT wafers usually used for GW generation.	28
2.7	Schematic of PZT disc bonded on the top surface of a substrate for GW generation.	28
2.8	Different modeling schemes for piezoelectric actuators.	29
2.9	Overview of piezo-coupled University of Michigan Local Interaction Simulation Approach (UM-LISA) formulation. The blue colored boxes represent the modifications to include electromechanical coupling.	30
2.10	Modeling in UM-LISA for piezoelectric actuators.	40
2.11	Different mechanisms for modeling sensors in the LISA formulation.	41
2.12	Sample curved electrodes used in the CLoVER construction.	42
3.1	Block diagram showing Local Interaction Simulation Approach (LISA) framework.	47
3.2	Flowchart showing the time-marching scheme utilized in the LISA simulations.	53
4.1	Schematic of the simulation model used for point-source convergence study.	56

4.2	Out-of-plane displacement component for different spatial discretizations are compared at different distances from the center of excitation in an isotropic substrate. Each column corresponds to a specific distance from the center of the actuator, and each row corresponds to a particular timestep used for the numerical simulation.	59
4.3	Out-of-plane displacement component for different temporal discretizations are compared at different distances from the center of excitation in an isotropic substrate. Each column corresponds to a specific distance from the center of the actuator, and each row corresponds to a particular spatial discretization used for the numerical simulation.	60
4.4	Snapshots of the out-of-plane displacement component at $20 \mu s$ for different discretizations. The displacements have been normalized by the amplitude at the point $1.25h$ from the center of the excitation point along the X_1 direction.	62
4.5	(a) Error associated with spatial discretization. The reference case for calculating error is $\Delta_{xyz} = \frac{h}{64}$. (b) Log-log plot of the error, the slope of the connecting line “m” determines the rate of convergence.	63
4.6	Comparison of relative root mean square deviation (RRMSD) error estimates for (a) cube and (b) cuboidal cells for different frequency-thickness cases.	66
4.7	Comparison of error estimates between cubic and cuboidal discretization.	67
4.8	Schematic of the simulation model used for piezo actuator convergence study.	68
4.9	normalized root mean square deviation (NRMSD) metric for the isotropic substrate for different discretizations.	70
4.10	NRMSD metric for the uni-directional laminate substrate for different discretizations.	71
4.11	Error associated with number of air cells for different plates for (a) a single time step at peak excitation ($23 \mu s$) (b) averaged over $72 \mu s$	72
5.1	Two CLoVERs used in the experimental studies.	77
5.2	The input excitation chosen for the validation studies.	77
5.3	Experimental setup showing different components used in the laser vibrometry experiments to measure the guided waves propagation field.	78
5.4	IM7/977-3 material phase slowness for the antisymmetric mode at 75 kHz.	80
5.5	Out-of-plane normalized displacements in a uni-directional laminate $[0]_{12T}$ at (a)-(b) $58 \mu s$ and (c)-(d) $68 \mu s$. Distances from the center of the plate normalized by actuator radius ($R_O = 6.4 \text{ mm}$).	81
5.6	Out-of-plane normalized displacements in a cross-ply laminate $[0/90]_{3S}$ at (a)-(b) $55 \mu s$ and (c)-(d) $68 \mu s$. Distances from the center of the plate normalized by actuator radius ($R_O = 6.4 \text{ mm}$).	82
5.7	Out-of-plane normalized displacements in a quasi-isotropic laminate $[0/-45/45/90/90/-45/45/0]_s$ at (a)-(b) $68 \mu s$ and (c)-(d) $78 \mu s$. Distances from the center of the plate normalized by actuator radius ($R_O = 6.4 \text{ mm}$).	83
5.8	Out-of-plane displacement pattern for uni-directional $[0]_{12T}$ laminate when the input waves are incident along (a)-(d) 0 deg, (e)-(h) 45 deg and (i)-(l) 90 deg directions. Snapshots of the propagating waveform are shown at (a)-(b) $57 \mu s$, (c)-(d) $67 \mu s$, (e)-(f) $67 \mu s$, (g)-(h) $77 \mu s$, (i)-(j) $87 \mu s$ and (k)-(l) $97 \mu s$	84

5.9	Out-of-plane displacement pattern for cross-ply $[0/90]_{3S}$ laminate when the input waves are incident along (a)-(d) 0 deg, (e)-(h) 22.5 deg, (i)-(l) 45 deg and (m)-(p) 67.5 deg directions. Snapshots of the propagating waveform are shown at $67\mu s$ for the two columns on the left and $77\mu s$ for the two columns on the right.	85
5.10	Out-of-plane displacement pattern for quasi-isotropic laminate when the input waves are incident along (a)-(d) 0 deg, (e)-(h) 180+22.5 deg, (i)-(l) 180+45 deg and (m)-(p) 67.5 deg directions. Snapshots of the propagating waveform are shown at $68\mu s$ for the two columns on the left and $88\mu s$ for the two columns on the right.	86
5.11	(a) Schematic of GW-based damage detection architecture for sandwich panels. (b) Components of the sandwich foam core.	88
5.12	(a) Composite sandwich specimen with macro fiber composite (MFC) actuator and retro-reflective tape. (b) Cross section of the composite foam core sandwich. (c) Cross-sectional schematic of the sandwich panel in UM-LISA simulations.	89
5.13	Ratio of the amplitudes of signals on the bottom surface and top surface for different frequencies at a distance of (a) 40 mm, (b) 50 mm, (c) 60 mm and (d) 70 mm from the center of the MFC actuator.	91
5.14	(a) Details for the Lead Zirconium Titanate (PZT) disc and Composite Long-range Variable-length Emitting Radar (CLOVER) configuration used in the damage interaction studies on quasi-isotropic laminate. (b) Experimental setup for the damage interaction studies.	93
5.15	Out-of-plane displacement pattern comparison between pristine and simulated damage quasi-isotropic laminates. The black square represents the position of the damage.	94
5.16	Comparison between LISA simulations and experiments for the normalized peak-to-peak reflection amplitude recorded with the CLOVER transducer in quasi-isotropic $[0/45/-45/90/90/-45/45/0]_S$ laminate when the damage was aligned with (a) sector 1, (b) sector 2, (c) sector 3, and (d) sector 4	95
5.17	Comparison between LISA simulations and experiments for the normalized peak-to-peak reflection amplitude recorded with the CLOVER transducer in quasi-isotropic $[0/45/-45/90/90/-45/45/0]_S$ laminate, when the damage was aligned with (a) sector 5, (b) sector 6, (c) sector 7, and (d) sector 8, e) sector 9, (f) sector 10,	96
5.18	Comparison between LISA simulations and experiments for the normalized peak-to-peak reflection amplitude recorded with the CLOVER transducer in quasi-isotropic $[0/45/-45/90/90/-45/45/0]_S$ laminate, when the damage was aligned with (a) sector 11, and (b) sector 12, (c) sector 13, (d) sector 14, and (e) sector 15	97

5.19	In-plane displacement component along the X -direction in the quasi-isotropic plate. It is obtained by subtracting the displacement field of the pristine case from the damaged one. guided waves (GW) are generated by the PZT disc shown as yellow disc and the CLoVER is shown as a translucent annulus around it; the damage is indicated by the black square in the right side of the plate.	98
5.20	Snapshots of the in-plane displacement pattern for the actuator nodes for different actuator models for an isotropic substrate. Each row corresponds to a particular time step during the actuation. The first column represents the particular time step where the actuator nodes are compared. The second column shows the actuator nodes in the piezo-coupled actuation case. The third column is for the prescribed displacement method-I input, and the fourth column is for the prescribed displacement method-II input.	101
5.21	Snapshots of the out-of-plane displacement pattern for the actuator nodes for different actuator models for an isotropic substrate. Each row corresponds to a particular time step during the actuation. The first column represents the particular time step where the actuator nodes are compared. The second column shows the actuator nodes in the piezo-coupled actuation case. The third column is for the prescribed displacement method-I input, and the fourth column is for the prescribed displacement method-II input.	102
5.22	Snapshots of the in-plane displacement pattern for the actuator nodes for different actuator models for a uni-directional laminate. Each row corresponds to a particular time step during the actuation. The first column represents the particular time step where the actuator nodes are compared. The second column shows the actuator nodes in the piezo-coupled actuation case. The third column is for the prescribed displacement method-I input, and the fourth column is for the prescribed displacement method-II input.	103
5.23	Snapshots of the out-of-plane displacement pattern for the actuator nodes for different actuator models for a uni-directional laminate. Each row corresponds to a particular time step during the actuation. The first column represents the particular time step where the actuator nodes are compared. The second column shows the actuator nodes in the piezo-coupled actuation case. The third column is for the prescribed displacement method-I input, and the fourth column is for the prescribed displacement method-II input.	105
5.24	Comparison between experimental data and LISA simulations along the 0 deg azimuthal direction for different actuation methods at varying distances from the center of the actuator.	106
5.25	Comparison between experimental data and LISA simulations along the 90 deg azimuthal direction for various actuation methods.	107
5.26	Comparison between FFT of the experimental data and LISA simulations at 40 mm from the center of the actuator along various azimuthal directions. . . .	108
5.27	Comparison between the experimental data, UM-LISA (PC method) simulations and global matrix method for the out-of-plane displacement at 40 mm from the center of the actuator along 0 deg and 90 deg azimuthal direction. . .	108
5.28	Effect of density reduction on UM-LISA simulation of GW.	109

5.29	Schematic of the experiment of Raghavan and Cesnik [46].	111
5.30	Comparison between experimental and theoretical sensor response amplitudes in the rectangular actuator experiment at different center frequencies for: (a) S_o mode and (b) A_o mode [46].	112
5.31	Comparison between experimental, theoretical and UM-LISA (PC method) sensor response amplitudes in the rectangular actuator experiment at different center frequencies for: (a) S_o mode and (b) A_o mode.	112

LIST OF TABLES

Table

3.1	Input file parameters.	48
3.2	Actuation method flags in <i>ActuationFlags.txt</i>	49
3.3	Actuation dimensions in <i>ActuatorDimensions.txt</i>	50
3.4	Output files generated.	51
3.5	Simulated damage parameters in <i>Damage.txt</i>	52
3.6	Inputs and Outputs of the iterative equations.	52
4.1	Discretization parameters for convergence studies in an isotropic plate.	57
4.2	Discretization parameters for determining rate of convergence in an isotropic plate.	61
4.3	Discretization parameters for piezo actuator convergence studies.	69
4.4	Guidelines for parameter selection in UM-LISA.	72
5.1	Mechanical properties of different materials used in the simulations.	75
5.2	Transducer piezoelectric properties.	76

LIST OF ABBREVIATIONS

1D	one-dimensional
2D	two-dimensional
3D	three-dimensional
BEM	boundary element method
CFL	Courant-Friedrichs-Lewy number
CLoVER	Composite Long-range Variable-length Emitting Radar
FD	finite difference
FE	finite element
GM	global matrix
GPU	graphics processing unit
GW	guided waves
IE	iterative equation
LISA	Local Interaction Simulation Approach
MFC	macro fiber composite
NDE/NDT	nondestructive evaluation/testing
NRMSD	normalized root mean square deviation
ODE	ordinary differential equation
P	longitudinal waves
PC	piezo-coupled
PD	prescribed displacement
PDE	partial differential equation

PZT Lead Zirconium Titanate

RRMSD relative root mean square deviation

S shear waves

SEM spectral element method

SHM structural health monitoring

SIM sharp interface model

SH shear horizontal

SV shear vertical

UM-LISA University of Michigan Local Interaction Simulation Approach

LIST OF SYMBOLS

c_{max}	Maximum wave speed (m/s)
C_θ, S_θ	Cosine and Sine functions of the angle θ , respectively
D	Electric displacement (C/m ²)
e	Piezoelectric stress constants (C/m ²)
E	Electric field (V/m)
g	Piezoelectric material matrix (V m/N)
R	Rotation matrix
R_i	Inner radius (m)
R_o	Outer radius (m)
S	Stiffness tensor (N/m ²)
S_{max}	Maximum stiffness tensor component (N/m ²)
t	Time/time step
u	Number of nodes with induced potentials
v	Number of nodes with unique potentials
V_o	Constant depending on piezoelectric and elastic sensor material properties
V_s	Induced voltage in sensor (V)
V	Voigt notation
w_1	Displacement field component along X_1 (m)
w_2	Displacement field component along X_2 (m)
w_3	Displacement field component along X_3 (m)
X_1, X_2, X_3	Coordinate axes
α, β, γ	LISA position indices ± 1
β	Impermittivity constant matrix (C m/V)
δ	Kronecker delta function
Δt	Computational time step (s)
$\Delta \theta$	Azimuthal sector angle (rad)
$\Delta x_1^\alpha, \Delta x_2^\beta, \Delta x_3^\gamma$	Spatial discretizations (m)
δ	Intermediate discretization parameter 1 (m)
ϵ	Intermediate discretization parameter 2 (m)
ϵ	Strain tensor
θ	Angle between the ply material coordinate system and the laminate global coordinate system (rad)
$\Theta_{u \times 1}$	Material property and mechanical displacement dependent matrix
κ	Permittivity (C/Vm)

$\Lambda_{u \times v}$	Transformation matrix
ρ	Material density (kg/m ³)
τ	Stress tensor (N/m ²)
$\Phi_{u \times u}^o$	Material property dependent matrix
χ	Numerical constant ($\Delta t^2 / \rho$) (s ² m ³ /kg)
ψ	Electric potential (V)
$\psi_{u \times 1}^o$	Vector of the unknown potentials

Subscripts

,	Spatial derivative
k, l, m, n	Direction indices 1, 2, 3
s	Sensor
η, ζ	Voigt's indices (1, ..., 6)

Superscript

.	Temporal derivative
~	Shorthand to represent one of the eight cells surrounding a point
E	Constant electric field
i, j, k	Direction indices 1, 2, 3
o	Principal (material) axis reference frame
S	Constant strain
T	Transpose of a matrix
α, β, γ	LISA position indices ± 1
σ	Constant stress

ABSTRACT

Numerical Simulation Of Guided Waves In Thin Walled Composite Structures

by

Kalyan Sreenivas Nadella

Chair: Professor Carlos E. S. Cesnik

The success of guided waves (GW) in the area of nondestructive evaluation/testing (NDE/NDT) has spurred their utilization in structural health monitoring (SHM). GW present promising possibilities in developing SHM systems as they can travel long distances over the structure's surface, and also through its thickness. In addition to damage detection, GW are capable of providing the overall degradation state of the material in terms of stiffness change.

Wave propagation has been studied extensively for isotropic materials, but studies for composite structures are still in the beginning stages. A good understanding of the GW propagation is required to build robust and reliable SHM systems. It has been shown that Local Interaction Simulation Approach (LISA), a numerical method based on finite difference transformations, is capable of efficiently and accurately modeling GW generation, propagation, and damage interaction in engineering structures.

First, the basic theoretical development for the University of Michigan Local Interaction Simulation Approach (UM-LISA) is presented. Then LISA is extended to model three-dimensional (3D) multi-layered orthotropic structures with nonuniform cell aspect

ratios. The iterative equations for the simulations are extended for orthotropic materials in a non-principal axis frame, which will benefit in modeling generic laminated composite structures. The validation studies are performed against experimental data.

UM-LISA is further developed to model the piezoelectric actuator effects. The iterative equations are extended for piezoelectric materials by taking into account the electromechanical coupling of the governing equilibrium equations. New constitutive and compatibility conditions are considered to account for the coupling in the electrical and mechanical parameters. The iterative equations calculate mechanical displacements in an explicit time marching scheme, whereas the electric potentials are calculated using an implicit scheme. Studies are carried out to demonstrate the improvements in modeling GW generation using piezo-coupled version of the UM-LISA framework.

These studies demonstrate the advantages of UM-LISA as an advanced multiphysics numerical framework to model GW generation and propagation in thin-walled composite structures.

CHAPTER 1

Introduction

Functionality, endurance and lower cost of operation are some of the most desirable characteristics of engineered structures. To ensure these qualities, estimation of the mechanical system's overall condition and remaining life is critical. This can be achieved by employing appropriate damage prognosis systems. Structural health monitoring (SHM) is one of the main components of damage prognosis. It can monitor and provide information about the possible presence of damage in the structure. Foremost among active schemes for SHM are guided waves (GW)-based methods. These are capable of carrying out maintenance checks on demand. A good understanding of the GW characteristics in modern engineering structures is required to build robust and reliable structural health monitoring systems.

This chapter presents a brief introduction to SHM and GW. The current state of GW modeling is described and the need for an alternative flexible modeling tool is introduced along with an outline of the thesis.

1.1 Structural Health Monitoring

Damage prognosis of an engineering system can be defined as the estimation of the remaining useful life based on history of operation, existing state, future load conditions and possible damage events [1]. In aerospace structures, this estimation is highly critical in optimizing scheduled maintenance to reduce downtime.

More recently, a DOD Roadmap regarding structural health and usage monitoring indicated that it plans, “in the not too distant future, to transition from usage monitoring to individual component damage tracking, to enhance our health assessment capability with better prediction of fatigue for each dynamic component and fatigue critical area” [2]. Along with fatigue, wear and damage limit structural life are common reasons for replacement of critical rotorcraft components, such as rotor blades and fuselage parts. Damage and usage monitoring are essential to the development of timely and cost effective maintenance of rotorcraft. According to Ref. [3], it is estimated that 8% of any rotary-wing fleet should be overhauled each year to maintain maximum readiness and safety. Figure 1.1 shows the distribution of airframe defects encountered during the UH-60 airframe condition evaluation cycle, where the occurrence of cracks and loose fasteners were observed as prevalent defects. Effective monitoring of these hot-spots, along with those on the rotor, can substantially reduce inspection and maintenance costs and extend the operational life of an aircraft. Such monitoring relies on efficient, multifunctional sensors for loads monitoring and structural integrity estimation, which are key to the development of condition-based maintenance processes.

structural health monitoring (SHM) systems usually involve the integration of networks of transducers, data transmission, implementation of algorithms and processing ability within the structures. SHM systems can be broadly classified into active schemes and passive schemes depending on the use of external stimuli. Passive schemes usually implement fiber optic sensors or foil strain gauges. They do not require on-board actuators to operate but require high sensor densities on the structure, which is a severe drawback. Active schemes utilize transducers, which are capable of exciting the structure and inquiring for damages. Foremost among active schemes for SHM are GW-based methods.

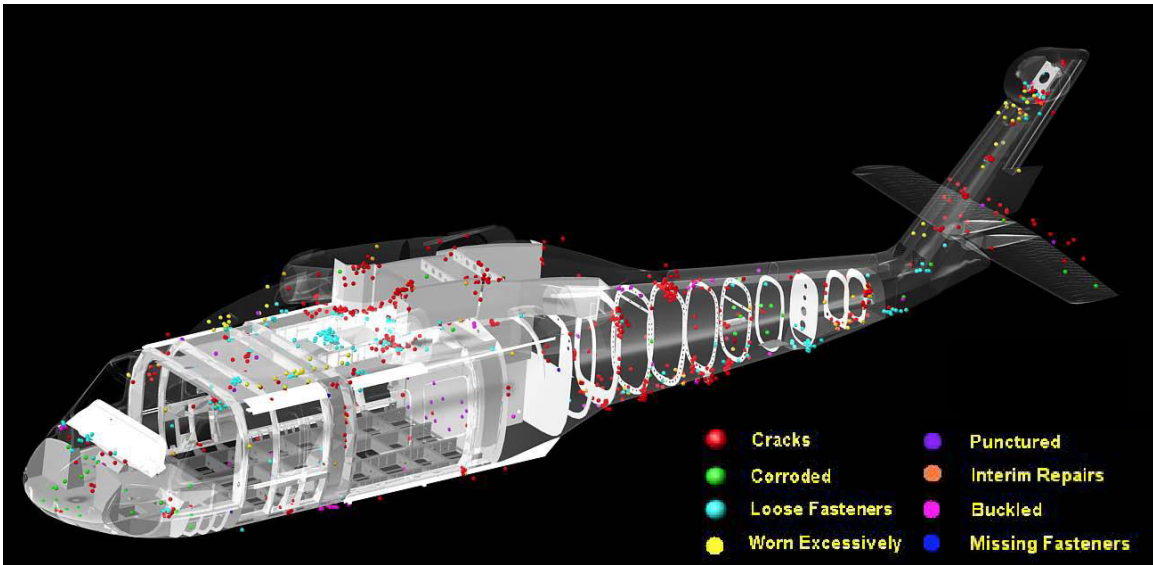


Figure 1.1: Distribution of defects on a UH-60 airframe during condition evaluation cycle [3].

1.2 Waves and Structural Health Monitoring

1.2.1 Waves

A mechanical wave can be described as a disturbance, vibration or oscillation that propagates through a medium, usually accompanied by energy transfer. The physical medium deforms to allow the wave propagation but there is no permanent transfer of mass associated with wave motion. Common examples of mechanical waves include sound waves, ocean waves and the vibration of membranes in percussion instruments.

Mechanical waves can be broadly classified based on the vibration direction of the particles in a medium. If the particles oscillate in the direction of the wave propagation, they are called longitudinal (P) waves (also known as primary waves or pressure waves). If the particles oscillate in the direction perpendicular to the wave propagation direction, they are called shear waves (S) (also known as secondary waves or transverse waves). More information regarding waves and wave propagation in solid media can be found in Ref. [4–10]

Surface waves are another class of waves that exist in nature. These waves are usually accompanied by circular motion of the surface particles, predominantly at the interfaces of two media. Most of the waves observed in bodies of water belong to this category. The surface waves can be further classified as Love waves and Rayleigh waves. Love waves have only transverse motion associated with the particles, whereas Rayleigh waves have both longitudinal and transverse components. Although Rayleigh waves have been used for damage detection in the past [11–17], they propagate on the surface of semi-infinite media, which makes them suitable in detecting only the surface and subsurface defects. In engineering structures, the damage can originate inside the structure and evolve to the surface just before the component fails catastrophically.

1.2.2 Lamb Waves

As presented in Sec. 1.2.1, waves travel in a solid medium in the form of longitudinal or shear waves. In a three-dimensional (3D) solid material, the shear waves can be further classified as shear horizontal (SH) or shear vertical (SV) waves [4,5] based on the direction of polarization. In thin-walled structures, coupling of the shear vertical and longitudinal waves results in a different class of waves called Lamb waves. They were first presented in 1917 by the British applied mathematician, Horace Lamb, and the waves were named after him. Lamb waves were not studied extensively until the 1960's when Gazis [18] and Viktorov [10] provided further details regarding the Lamb wave solution. Following this, Firestone [19,20] found a practical way to utilize Lamb waves for damage detection which spurred the utilization of Lamb wave-based GW for damage interrogation, in the fields of nondestructive evaluation/testing (NDE/NDT) and SHM.

1.2.3 Guided Waves for Structural Health Monitoring

GW are mechanical waves which follow a path determined by boundary conditions, usually in the form of geometrical features. The advantage of using GW is their ability

to be transmitted over long distances with little attenuation. Examples of guided waves include Rayleigh waves (surface of semi-infinite media), Stonely waves (interface of two elastic media) and Lamb waves (thin-walled structures). The success of guided waves in the area of NDE/NDT has spurred their utilization in SHM [21]. GW present promising possibilities in developing SHM systems as they can travel over the surface of the substrate, and also through the thickness of the structure. By controlling the testing parameters such as excitation frequency, GW can be sensitive to specific defects in terms of both their location and size. In addition to damage detection, GW are capable of providing the overall degradation state of the material in terms of stiffness change.

Although using GW for SHM is promising, there are several complications. At any given frequency, multiple modes co-exist and most of the waves are highly dispersive in nature. Propagation characteristics, such as wave speeds and amplitude, are dependent on the elastic properties of the material, which complicates the implementation of GW for composites. Wave propagation has been studied extensively for isotropic materials [4, 5], but studies for composite structures are limited. A good understanding of the GW propagation characteristics is required to build robust and reliable SHM systems. This is essential as there has been a gradual accretion of composite-based structures in modern manufacturing industries because of their superior physical attributes, such as high specific strength-to-weight and stiffness-to-weight ratios, as well as long fatigue life over metallic structures.

1.2.4 Guided-wave Generation

There are multiple options for the generation of GW in structures. A review of the recent developments in this field was presented by Raghavan and Cesnik [21]. Piezoelectric materials bonded to the surface or embedded in the structure are the most commonly used excitation methods. Piezoelectric transducers work on the principle of piezoelectricity, which can be defined as the ability of certain materials to generate electrical charge under

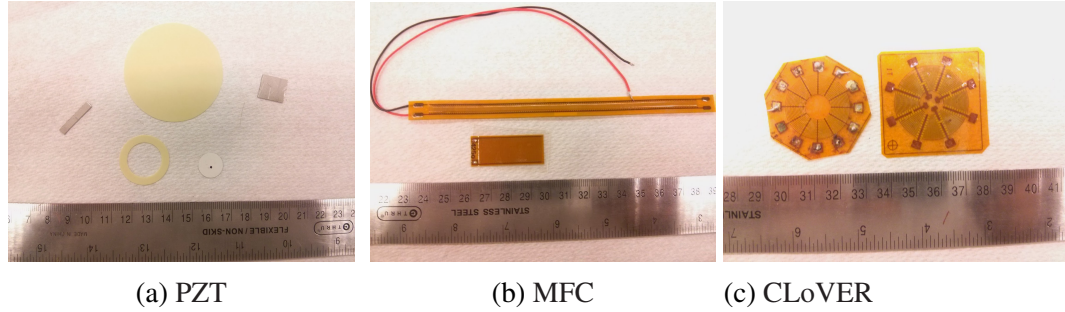


Figure 1.2: Different transducers used for wave generation.

mechanical stress. The most prominent of the piezoelectric materials used for the transduction of GW is an inorganic ceramic material called Lead Zirconium Titanate (PZT). PZT materials have been used in the form of surface-bonded wafers (Fig. 1.2(a)) to generate GW in structures, but their brittle nature and non-conformability have limited their use on highly curved surfaces. The macro fiber composite (MFC) (Fig. 1.2(b)) transducers, introduced by Wilkie et al. [22], have surmounted the shortcomings of the PZT wafers by providing a high-authority, flexible, and resilient transducer for a variety of applications.

An ideal SHM transducer is resistant to damage due to environmental conditions, can be easily bonded onto curved surfaces, and best exploits the limited input energy to maximize reflections from possible damage sites. Although MFCs have most of the required characteristics of an ideal transducer, including the ability to focus the emitted waves along a given direction (and, therefore, cover longer ranges or use less energy), they lack the ability to interrogate and receive signals from all directions. Focused waves and steering have been achieved with the help of transducer arrays [23–28]. These use construction/destruction of signals to generate the focused GW, which is inefficient due to the additional energy used for shaping and not to actually determine the level of damage. The Composite Long-range Variable-length Emitting Radar (CLOVER) [29, 30] transducer, illustrated in Figure 1.2(c), has been designed to leverage the strengths of traditional MFC transducers while adding 360-deg coverage in an efficient way.

1.3 Modeling Guided Waves

The utilization of GW for SHM systems requires an in-depth understanding of wave propagation. There are many factors affecting the wave characteristics in structures such as boundary conditions, initial conditions (temperature, pre-stress, etc.), transducer size and location, and the material properties of the substrate. In the past, 3D elasticity-based theories [4, 5] were used to describe the wave propagation in isotropic and anisotropic media. Obtaining dispersion relations of Lamb waves in anisotropic media was the focus of some researchers [31–33]. Theoretical models are restricted to infinite or semi-infinite media. Several analytical and numerical methods have been proposed to address wave propagation in practical structures.

1.3.1 Analytical and Semi-analytical Modeling

The use of Kirchhoff plate theory for wave propagation has been limited as shear deformation effects which are important in the wave propagation problems [34, 35] were disregarded in this theory. Mindlin plate theory [34] has been a popular choice for researchers in modeling wave propagation using analytical methods. Lin and Yuan [36] adopted Mindlin plate theory to model wave propagation by taking both transverse shear and rotary inertia effects into account. Classical laminate theory was used to address the stacking of the actuator and substrate by assuming linear distribution of strains across the substrate and PZT [37]. A constant strain field was considered inside the sensor area and the response was calculated based on an equivalent capacitor. The electromechanical coupling was not considered in the modeling. Rose and Wang [38] used Mindlin plate theory to derive expressions for a substrate's response to point force and point momentum input. Later, Rose et al. [39] used the same theory, along with components of diffraction tomography, for imaging some damage types observed in plate-like structures. This method is limited because only certain damages, which can be represented as flexural inhomogeneities, are able

to be modeled. Although there are advantages to using Mindlin plate theory, it is limited to flexural modes and only appropriate to resolve wavelengths greater than approximately twice the plate thickness [39].

Further down the line, higher order plate theories [40–42] and semi-analytical matrix methods [43–48] have been used to model wave propagation in composite-laminated infinite plates. Recently, Raghavan and Cesnik [46] developed an elasticity-based formulation for GW excitation by finite dimensional piezoelectric transducers in composite plates. This study aimed at investigating the excitation and propagation of GW by finite-dimensional piezoelectric-based transducers in composite plates through theoretical modeling and experimental testing. The model was able to capture the multi-modal nature of GW and is also valid at high frequency-thickness regions. Although analytical/semi-analytical models are able to predict the GW propagation, they are restricted to simple composite structural features and boundary conditions. Since modeling boundary reflections, damage interaction, and geometric complexities (joints, stiffeners, rivets, varying thicknesses, etc.) become difficult using analytical models, several numerical computational methods have been proposed to address them.

1.3.2 Numerical Modeling

Lee and Staszewski [49] provided a good review of numerical methods used for modeling GW. In the past, traditional methods utilized finite difference (FD) [50–55] and finite element (FE) [56–61] methods. FD methods for wave propagation have been traditionally used in the field of geophysics [55] and in seismic-wave propagation modeling [62–66]. Their utilization in the field of wave propagation in engineering structures has been limited because of the requirement of smoothing parameters for material interfaces with impedance differences which greatly increases the computational requirements and associated numerical errors [67]. The FE methods are implemented using an implicit scheme [68] or an explicit scheme [69]. Although implicit schemes are unconditionally stable, the larger com-

putational effort required to solve the linear system of equations has limited its utilization for wave propagation. Explicit schemes, on the other hand, might provide improved performance but require a smaller timestep to satisfy stability conditions, leading to numerical error accumulation [70] and spurious wave oscillations [70, 71].

Later on, the boundary element method (BEM) [72] was introduced. The method is based on converting the volume integrals used in traditional FE to surface integrals using Green's functions. The most advantageous feature of BEM is its ability to model infinite and semi-infinite domain problems, as it requires discretization of the surface rather than the volume. Although the method has shown promise in the field of wave propagation [73–80], it is not efficient for thin-walled structures and finite media because of the large surface/volume ratio and the close proximity of surface nodal points on either side, which can lead to inaccuracies.

Another derivative of the FE method is the spectral element method (SEM). SEM is further classified as either a subparametric approach [81] or frequency domain formulation [82]. The frequency domain formulation [83, 84] has been used for characterizing wave propagation in one-dimensional (1D) structures [85–87]. The shape functions in SEM are formulated by utilizing the exact solution for the governing equations in the frequency domain. The frequency transformation enables the conversion of transient wave equations defined by partial differential equation (PDE) into ordinary differential equation (ODE), which are solved easily. More details for SEM can be found in Refs. [88, 89]. Due to the exact form of the shape functions, SEM provides more accurate results with less computational time when compared with standard FE methods. Although SEMs are superior to FE methods, the advantages are limited for simple structures where the exact shape functions can be calculated. Some lesser known numerical methods for characterizing wave propagation are listed in Stepinski et al. [90] with appropriate references.

1.3.3 Local Interaction Simulation Approach

An efficient numerical alternative to accurately model wave propagation is the Local Interaction Simulation Approach (LISA). This method is based on iterative equation (IE) for “unit cells” that are used to represent/discretize the model. The material properties in LISA are assigned to the cells, whereas the field variables are calculated at nodes constituting the cells. The actual IEs are derived from the elastodynamic equilibrium equations. Although LISA is similar to FD methods in its resolution of spatial and temporal derivatives, it differs in the implementation of the sharp interface model (SIM), which allows for physical and unambiguous treatment of interface discontinuities without the use of smoothing parameters as in traditional FD methods [67]. The SIM enforces the continuity of displacement and stress field across the interfacial nodes.

The LISA formulation was introduced by Delsanto and co-workers. The first formulation was presented for 1D LISA [91] and subsequently the two-dimensional (2D) LISA [67] and three-dimensional (3D) LISA [92] formulations were presented. The equations are capable of modeling homogenous and non-homogeneous orthotropic media oriented in a principal reference frame. One of the initial motivations for the development of LISA was its capability of being deployed as a highly parallelized numerical tool for wave propagation.

Subsequently, the framework was adopted and implemented by several researchers, such as Agostini et al. [93, 94], to model orthotropic structures in a principal reference frame, and by Lee and Staszewski [49, 95], to model GW propagation and damage interaction in isotropic structures using the 2D LISA formulation. Ruzzene et al. [96] used the 2D LISA approach to model wave propagation in isotropic plates for simple damage interaction studies and compared the results with laser vibrometry data. The 2D LISA was later used by Dobie et al. [97] to model wave propagation and damage interaction using air-coupled ultrasonic scanners in aluminum plates and Borkowski et al. [98] to model GW interaction with damage in aluminum lug joints. Spencer et al. [99] utilized LISA to estimate material

elastic properties in multi-layered composite plates based on wave propagation. Stepinski et al. [100] used LISA to review the beampatterns of 2D actuator arrays.

Recently, LISA has also been used for studying wave propagation in non-classical materials, and newer physical/biological phenomenon. Hirsekorn et al. [101] studied wave characteristics in sonic crystals consisting of local resonators, and Scalerandi et al. [102–105] used modified LISA formulations to study vibrations in nonlinear elastic bars [102], growth of thin semiconducting films [105], and self-regulatory mechanisms in cell behavior [103].

The 3D LISA framework was extended by Sundararaman and Adams [106] to model orthotropic media with non-uniform spatial discretizations and a visco-elastic damping term. Although this LISA formulation has a wider application range, it was primarily utilized to model GW propagation and damage interaction in isotropic plates with uniform spatial discretization. The GW propagation and damage interaction studies with composites were limited and restricted to orthotropic layer rather than a laminate.

As previously mentioned, easy and efficient parallelization is one of the key advantages of LISA formulation. For several decades, Moore’s law [107] of doubling the transistor density on integrated circuits was driving computational prowess. Recently, however, such improvements are coming to an end [108, 109]. The new direction of computational advancement has been graphics processing unit (GPU) computing. Initially driven by the enormous market for video games, it is increasingly applied in scientific computing. GPU computing is especially useful in areas where computational requirements are large, sufficient scope for parallelization exists, and throughput is more important than latency [110]. Similar to other scientific communities, there has been an increased interest in utilization of GPU computing for wave propagation studies [111–116]. More recently, Paćko et al. [111] and Bielak et al. [117, 118] integrated LISA with GPU architecture and observed increased computational efficiency in simulating GW propagation.

1.4 Research Objectives and Dissertation Overview

The main objective of this dissertation is to develop a multi-physics-based numerical formulation to enable the efficient and accurate modeling of GW generation, propagation and sensing for the development of GW SHM. This was implemented in the University of Michigan Local Interaction Simulation Approach (UM-LISA) code. The simulation framework aims to model GW in layered orthotropic composite laminates including the electromechanical coupling effects between piezoelectric transducers and the substrate. The numerical tool is validated against experimental data.

Chapter 2 introduces the governing equations and constitutive relations used in the development of UM-LISA. The finite difference relations used to resolve the spatial derivatives are presented along with SIM, which enforces the continuity of displacements and stresses along different material interfaces. The iterative equations of UM-LISA framework are presented for generalized orthotropic laminates in non-principal reference axes. Later, the chapter describes the piezoelectric coupling between the transducers and the substrate using electromechanical constitutive relations and the final 3D iterative equations are presented for the piezoelectric coupled UM-LISA.

Chapter 3 gives an overview of the implemented multi-physics numerical analysis framework, UM-LISA. Contributions from different researchers are summarized. The main functions of the framework are presented in a block diagram. Details for model initialization, actuation type, excitation, and implementation are discussed. The chapter provides useful information for code migration for future developers to integrate it with mesh generation software or incorporate GPU based parallel computing.

Chapter 4 presents basic convergence studies for the UM-LISA framework. Preliminary studies are performed to determine the effect of spatial and temporal discretizations. Next, simulations are conducted to determine the convergence rate, and characterize the evolution of error for cubic and distorted (cuboid) grids. Simulations are also carried out for surface mounted actuators to determine the minimum discretization required for the ac-

tuator. Finally, suggestions regarding the optimal parameters while utilizing UM-LISA for wave propagation are presented.

Chapter 5 presents the numerical analysis results for several cases. The displacement field at the interaction between the actuator and substrate is studied for different substrates that highlight the effect of substrate's anisotropy in GW generation and also how the new piezo-coupled formulation differs from the traditional prescribed displacement methods. The ability of the UM-LISA to model electromechanical coupling between the transducer and the substrate is taken advantage of while simulating the frequency response of the piezo sensors. The numerical tool is also used for simulating damage interaction studies.

Finally, the results from this thesis are compiled in Chapter 6, where the key contributions in modeling GW for SHM are presented and suggestions for future research are noted.

CHAPTER 2

Theoretical Formulation

This chapter presents the formulation for the UM-LISA framework. Equilibrium equations, constitutive relations, and the compatibility conditions are derived for layered composite and later extended to piezo-coupled version of UM-LISA. The chapter also presents the FD transformations and the implementation of SIM in the derivation of the recursive relations. The final iterative equations are presented and the newly introduced terms in the iterative equations highlighted.

2.1 Original Formulation

The original formulation methodology for LISA [67,91,92] is presented as a flowchart in Fig. 2.1. The iterative equations were developed from the elastodynamic equilibrium equations in the displacement form. FD transformations were used to resolve the spatial derivatives, and SIM was employed to enforce displacement and stress continuity conditions to derive the recursive relations. It should be noted that the original formulation was presented for uniform cell size ($\Delta x_1 = \Delta x_2 = \Delta x_3$) and orthotropic media in a principal reference frame which limits its utilization for thin walled anisotropic composite structures.

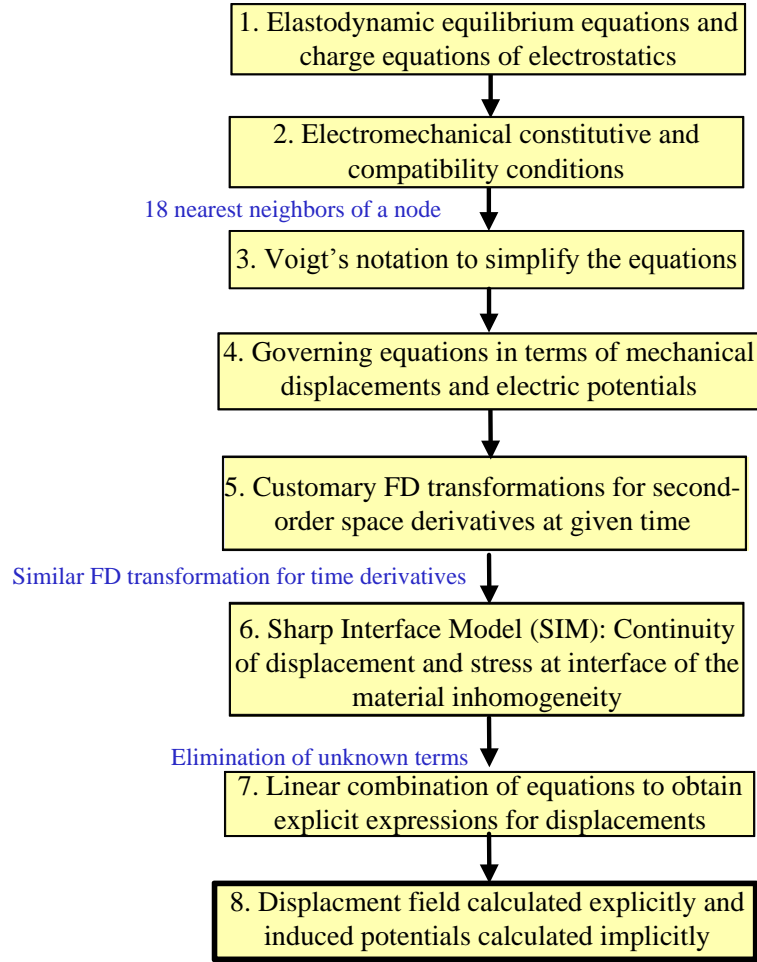


Figure 2.1: Overview of LISA’s original formulation as presented in Ref. [92].

2.2 UM-LISA Formulation: Layered Composite Laminates

This section presents the UM-LISA formulation for orthotropic layered composites in non-principal reference frames with non-uniform cell discretizations ($\Delta x_1 \neq \Delta x_2 \neq \Delta x_3$). The iterative equations which form the basis of the LISA method are developed from the elastodynamic equilibrium equations in the displacement form. Spatial and temporal derivatives are then resolved with FD transformations to obtain the IEs for a homogeneous medium. To address the inhomogeneity in practical applications, SIM is employed at the interface of different materials to derive the necessary recursive relations. Finally, the dis-

placement components at a particular node can be written as a function of displacements at previous two time steps of the neighboring nodes. The outline for the derivation is shown in Fig. 2.2, where the orange colored boxes indicate the augmentations to the basic theory [92, 119] introduced here.

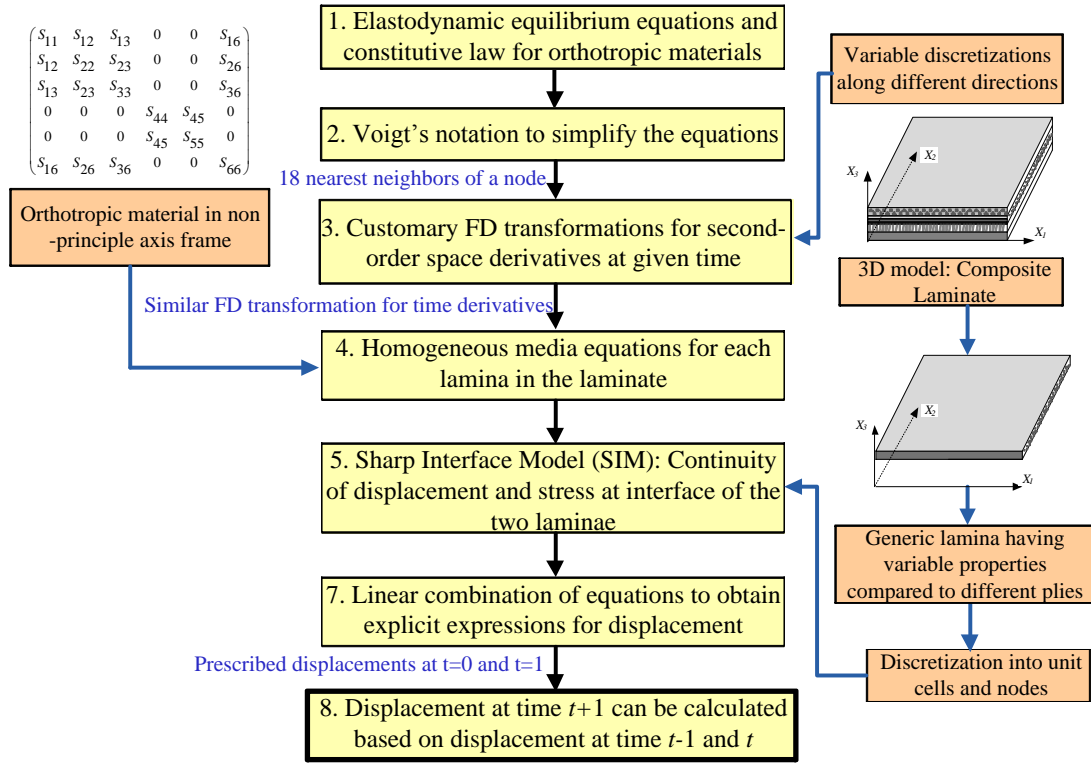


Figure 2.2: Overview of LISA's theoretical formulation (orange colored blocks on the right and left represent the new implementation aspects to the basic formulation).

2.2.1 Equations of Motion

The analysis begins with the elastodynamic equilibrium equations in the displacement form as:

$$\partial_l(S_{klmn}w_{m,n}) = \rho\ddot{w}_k \quad (k, l, m, n = 1, 2, 3) \quad (2.1)$$

where S is the stiffness tensor, ρ the material density, and w the displacement field. The first subscript in the displacement field indicates its component. Subscripts followed by a comma denote spatial differentiation, and the dot represents differentiation with respect to time. Voigt's notation is applied to Eq. 2.1, which combines two indices into a single index, i.e.,

$$\begin{aligned} V(kl) &= k\delta_{kl} + (1 - \delta_{kl})(9 - k - l) \quad V(kl) = 1, \dots, 6 \\ V(mn) &= m\delta_{mn} + (1 - \delta_{mn})(9 - m - n) \quad V(mn) = 1, \dots, 6 \end{aligned} \quad (2.2)$$

resulting in:

$$S_{V(kl)V(mn)}w_{m,nl} = \rho\ddot{w}_k \quad (2.3)$$

where the indices k, m, n and l assume values 1, 2 and 3. The indices $V(kl)$ and $V(mn)$ are calculated based on Eq. 2.2 and δ is the Kronecker-delta function. It should be noted that Einstein notation is used to represent summation of repeated indices. Wave propagation for non-isotropic media using LISA has been studied for laminates with orthotropic laminae oriented along the principal axes [93, 106] in which most of the off-diagonal terms in the associated stiffness matrix are zero, that is,

$$S^\circ = \begin{pmatrix} S_{11}^\circ & S_{12}^\circ & S_{13}^\circ & 0 & 0 & 0 \\ S_{12}^\circ & S_{22}^\circ & S_{23}^\circ & 0 & 0 & 0 \\ S_{13}^\circ & S_{23}^\circ & S_{33}^\circ & 0 & 0 & 0 \\ 0 & 0 & 0 & S_{44}^\circ & 0 & 0 \\ 0 & 0 & 0 & 0 & S_{55}^\circ & 0 \\ 0 & 0 & 0 & 0 & 0 & S_{66}^\circ \end{pmatrix} \quad (2.4)$$

where S° represents the material properties in the principal (material) axis reference frame. In most of the practical applications, laminae with different orientation are stacked to construct the required composite structure. To address this issue, in-plane rotation of the orthotropic medium is considered in the formulation. A rotation matrix (R) used for in-plane

(X_1X_2 -plane) rotation is given by:

$$R = \begin{pmatrix} C_\theta^2 & S_\theta^2 & 0 & 0 & 0 & -2 \cdot C_\theta \cdot S_\theta \\ S_\theta^2 & C_\theta^2 & 0 & 0 & 0 & 2 \cdot C_\theta \cdot S_\theta \\ 0 & 0 & 1 & 0 & 0 & 0 \\ 0 & 0 & 0 & C_\theta \cdot S_\theta & C_\theta \cdot S_\theta & 0 \\ 0 & 0 & 0 & -C_\theta \cdot S_\theta & C_\theta \cdot S_\theta & 0 \\ C_\theta \cdot S_\theta & -C_\theta \cdot S_\theta & 0 & 0 & 0 & C_\theta^2 - S_\theta^2 \end{pmatrix} \quad (2.5)$$

where C_θ is $\cos(\theta)$ and S_θ is $\sin(\theta)$, and θ is the angle between the ply material coordinate system and the laminate global coordinate system. The new transformed stiffness matrix S then becomes:

$$S = RS^\circ R^T \quad (2.6)$$

$$S = \begin{pmatrix} S_{11} & S_{12} & S_{13} & 0 & 0 & S_{16} \\ S_{12} & S_{22} & S_{23} & 0 & 0 & S_{26} \\ S_{13} & S_{23} & S_{33} & 0 & 0 & S_{36} \\ 0 & 0 & 0 & S_{44} & S_{45} & 0 \\ 0 & 0 & 0 & S_{45} & S_{55} & 0 \\ S_{16} & S_{26} & S_{36} & 0 & 0 & S_{66} \end{pmatrix} \quad (2.7)$$

where R^T is the transpose of the rotation matrix, R . Once the new laminate stiffness matrix is determined, FD transformations along with SIM are used to transform Eq. 2.3 into iterative equations.

2.2.2 Discretization

Unlike traditional FD methods, there is no need to model complex boundary conditions or to introduce smoothing parameters while deriving the IEs. Further, the method is devel-

oped for easy parallelization, as all displacement components can be calculated separately based on the displacement components at previous time steps of the surrounding nodes. The 3D structure can be discretized into nodes and unit cells as shown in Fig. 2.3. It should be noted that a given unit cell has a unique material property, so it cannot span across different layers. To resolve the double spatial derivatives in space using FD transformations, all eighteen nearest-neighboring points around a given point C (as shown in Fig. 2.4) are required.

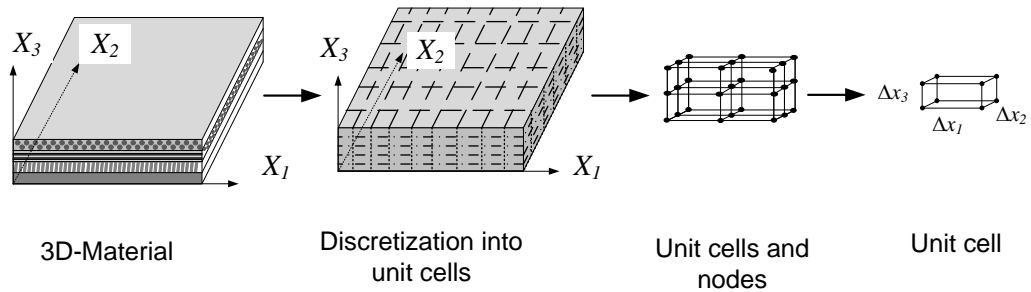


Figure 2.3: Schematic diagram showing the discretization in a 3D LISA formulation. The black dots represent the nodes, and the cuboid between eight dots represents a unit cell.

A grid with non-uniform spatial discretization is considered for the derivation. Finite difference relations are sufficient to transform the double spatial derivatives in space into recursive relations for homogenous materials. For heterogeneous structures, the SIM [92] is used to calculate the response at the “crosspoints” (the lattice points at the intersection of cells). The SIM assumes that the stress and displacement variables are uniform within a cell, and to maintain equilibrium and continuity, they are matched at the interface between cells. The extra conditions provided by the SIM incorporate the changes in stiffness, density, or attenuation properties into the iterative equations.

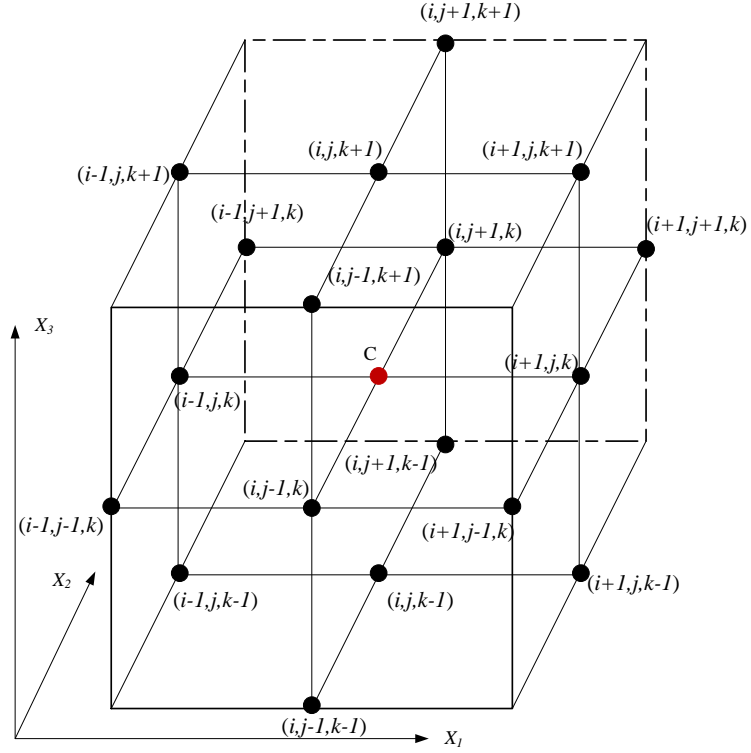


Figure 2.4: A generic point C at location (i, j, k) with eighteen nearest neighbors and the Cartesian system used in the analysis.

2.2.3 Finite Difference Transformations and Sharp Interface Model

In addition to the point C and its eighteen nearest-neighboring points (Fig. 2.4), eight points are considered as shown in Fig. 2.5(a) at a distance of $\delta \ll \Delta x_i$ ($i=1,2,3$), given by $(i + \alpha\delta, j + \beta\delta, k + \gamma\delta)$ for $\alpha, \beta, \gamma = \pm 1$. Equation 2.3 at the eight additional points for the displacement component w_k is represented as:

$$\sum_{m=1}^3 \sum_{\eta=1}^6 S_{\eta\xi}^{i+\alpha\delta, j+\beta\delta, k+\gamma\delta} w_{m,\xi}^{i+\alpha\delta, j+\beta\delta, k+\gamma\delta} = \rho \ddot{w}_k^{i+\alpha\delta, j+\beta\delta, k+\gamma\delta} \quad (2.8)$$

$$\alpha, \beta, \gamma = \pm 1$$

$$k = 1, 2, 3$$

Although the basic finite difference expressions for the derivation can be found in

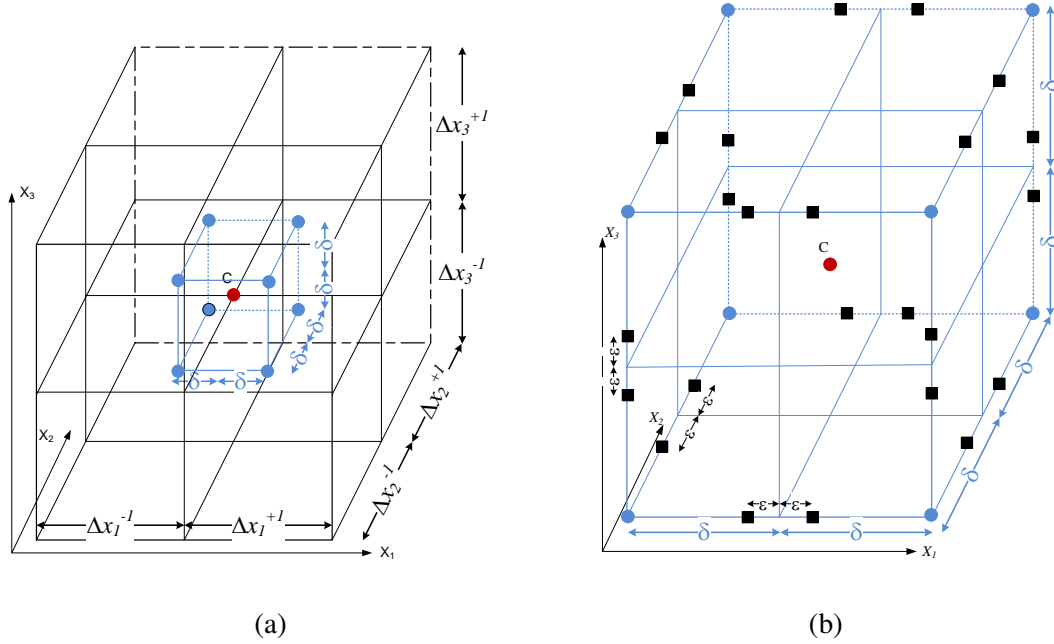


Figure 2.5: For a generic point C at location (i, j, k) , (a) blue dots represent the 8 points chosen to enforce displacement continuity, and (b) additional points shown as black squares are used to enforce stress continuity conditions.

Sinor [119], most of them are presented here for notational consistency and error rectification. The resulting equations for a particular component of displacement, w_k ($k = 1, 2, 3$), can be combined at these new points. Continuity of displacement, w_k , is obtained by prescribing displacements at two different timesteps (initialization steps) and then enforcing same acceleration \ddot{w}_k at subsequent timesteps [91]. The second-order derivatives in Eq. 2.8 are resolved as:

$$\begin{aligned}
w_{k,x_1x_1}^{i+\alpha\delta,j+\beta\delta,k+\gamma\delta} &= \frac{w_{k,x_1}^{i+\alpha/2,j,k} - w_{k,x_1}^{i+\alpha\delta,j+\beta\delta,k+\gamma\delta}}{\alpha\Delta x_1^\alpha/2} \\
w_{k,x_2x_2}^{i+\alpha\delta,j+\beta\delta,k+\gamma\delta} &= \frac{w_{k,x_2}^{i,j+\beta/2,k} - w_{k,x_2}^{i+\alpha\delta,j+\beta\delta,k+\gamma\delta}}{\beta\Delta x_2^\beta/2} \\
w_{k,x_3x_3}^{i+\alpha\delta,j+\beta\delta,k+\gamma\delta} &= \frac{w_{k,x_3}^{i,j,k+\gamma/2} - w_{k,x_3}^{i+\alpha\delta,j+\beta\delta,k+\gamma\delta}}{\gamma\Delta x_3^\gamma/2} \\
w_{k,x_1x_2}^{i+\alpha\delta,j+\beta\delta,k+\gamma\delta} &= \frac{w_k^{i+\alpha,j+\beta,k} - w_k^{i+\alpha,j,k} - w_k^{i,j+\beta,k} + w_k^{i,j,k}}{\alpha\beta\Delta x_1^\alpha\Delta x_2^\beta} \\
w_{k,x_2x_3}^{i+\alpha\delta,j+\beta\delta,k+\gamma\delta} &= \frac{w_k^{i,j+\beta,k+\gamma} - w_k^{i,j+\beta,k} - w_k^{i,j,k+\gamma} + w_k^{i,j,k}}{\beta\gamma\Delta x_2^\beta\Delta x_3^\gamma} \\
w_{k,x_3x_1}^{i+\alpha\delta,j+\beta\delta,k+\gamma\delta} &= \frac{w_k^{i+\alpha,j,k+\gamma} - w_k^{i+\alpha,j,k} - w_k^{i,j,k+\gamma} + w_k^{i,j,k}}{\alpha\gamma\Delta x_1^\alpha\Delta x_3^\gamma}
\end{aligned} \tag{2.9}$$

where the remaining spatial derivatives have similar form. The first-order derivatives in Eq. 2.9 are resolved as:

$$\begin{aligned}
w_{k,x_1}^{i+\alpha/2,j,k} &= \frac{w_k^{i+\alpha,j,k} - w_k^{i,j,k}}{\alpha\Delta x_1^\alpha} \\
w_{k,x_2}^{i,j+\beta/2,k} &= \frac{w_k^{i,j+\beta,k} - w_k^{i,j,k}}{\beta\Delta x_2^\beta} \\
w_{k,x_3}^{i,j,k+\gamma/2} &= \frac{w_k^{i,j,k+\gamma} - w_k^{i,j,k}}{\gamma\Delta x_3^\gamma}
\end{aligned} \tag{2.10}$$

where the superscript for w_k denotes a particular node in Fig. 2.4. It should be noted that, the first derivative of $w_k^{i+\alpha\delta,j+\beta\delta,k+\gamma\delta}$ for $\alpha, \beta, \gamma = \pm 1$ remains unevaluated and is eliminated when the stress continuity is enforced. To obtain continuity of stress, additional points are introduced: $(i + \alpha\varepsilon, j + \beta\delta, k + \gamma\delta)$, $(i + \alpha\delta, j + \beta\varepsilon, k + \gamma\delta)$ and $(i + \alpha\delta, j + \beta\delta, k + \gamma\varepsilon)$, with $\varepsilon \ll \delta \ll x_i$ ($i=1,2,3$) represented as black squares in Fig. 2.5(b). The derivatives associated with these points are resolved as:

$$\begin{aligned}
w_{k,x_1}^{i+\alpha\varepsilon,j+\beta\delta,k+\gamma\delta} &= w_{k,x_1}^{i+\alpha\delta,j+\beta\delta,k+\gamma\delta} \\
w_{k,x_2}^{i+\alpha\delta,j+\beta\varepsilon,k+\gamma\delta} &= w_{k,x_2}^{i+\alpha\delta,j+\beta\delta,k+\gamma\delta} \\
w_{k,x_3}^{i+\alpha\delta,j+\beta\delta,k+\gamma\varepsilon} &= w_{k,x_3}^{i+\alpha\delta,j+\beta\delta,k+\gamma\delta} \\
w_{k,x_1}^{i+\alpha\delta,j+\beta\varepsilon,k+\gamma\delta} &= w_{k,x_1}^{i+\alpha\delta,j+\beta\delta,k+\gamma\varepsilon} = \frac{w_k^{i+\alpha,j,k} - w_k^{i,j,k}}{\alpha\Delta x_1^\alpha} \\
w_{k,x_2}^{i+\alpha\varepsilon,j+\beta\delta,k+\gamma\delta} &= w_{k,x_2}^{i+\alpha\delta,j+\beta\delta,k+\gamma\varepsilon} = \frac{w_k^{i,j+\beta,k} - w_k^{i,j,k}}{\beta\Delta x_2^\beta} \\
w_{k,x_3}^{i+\alpha\varepsilon,j+\beta\delta,k+\gamma\delta} &= w_{k,x_3}^{i+\alpha\delta,j+\beta\varepsilon,k+\gamma\delta} = \frac{w_k^{i,j,k+\gamma} - w_k^{i,j,k}}{\gamma\Delta x_3^\gamma}
\end{aligned} \tag{2.11}$$

Similar expressions follow for the other terms. It should be noted that, in the manner discussed previously, the first derivative terms at the eight points shown in Fig. 2.5(a) remain unevaluated and are eliminated based on the stress continuity relations. The stress components (τ_{pl}) can be written as:

$$\tau_{pl} = S_{plmn}w_{m,n} \tag{2.12}$$

Next, the stress continuity is enforced with the help of the following relations:

$$\begin{aligned}
\tau_{p1}^{i+\varepsilon,j+\beta\delta,k+\gamma\delta} &= \tau_{p1}^{i-\varepsilon,j+\beta\delta,k+\gamma\delta} \\
\tau_{p2}^{i+\alpha\delta,j+\varepsilon,k+\gamma\delta} &= \tau_{p2}^{i+\alpha\delta,j-\varepsilon,k+\gamma\delta} \quad (p = 1, 2, 3) \\
\tau_{p3}^{i+\alpha\delta,j+\beta\delta,k+\varepsilon} &= \tau_{p3}^{i+\alpha\delta,j+\beta\delta,k-\varepsilon}
\end{aligned} \tag{2.13}$$

Using Eq. 2.8 at the eight surrounding points ($i+\alpha\delta, j+\beta\delta, k+\gamma\delta$) and the select group of stress continuity relations given in Eq. 2.13, the final IEs for the three-displacement components are derived for the 3D case as:

$$\begin{aligned}
w_1^{i,j,k,t+1} &= -w_1^{i,j,k,t-1} + 2w_1^{i,j,k} \\
&\quad - \frac{2\chi}{8} w_1^{i,j,k} \sum_{\alpha,\beta,\gamma=\pm 1} \left[\eta_x^2 \tilde{S}_{11} + \eta_y^2 \tilde{S}_{66} + \eta_z^2 \tilde{S}_{55} \right] \\
&\quad + \frac{\chi}{8} \sum_{\alpha,\beta,\gamma=\pm 1} \left[2\eta_x^2 \tilde{S}_{11} w_1^{i+\alpha,j,k} + 2\eta_y^2 \tilde{S}_{66} w_1^{i,j+\beta,k} + 2\eta_z^2 \tilde{S}_{55} w_1^{i,j,k+\gamma} \right] \\
&\quad + \frac{\chi}{8} \sum_{\alpha,\beta,\gamma=\pm 1} \left[\alpha\beta\eta_x\eta_y \left(\tilde{S}_{12} + \tilde{S}_{66} \right) \left(w_2^{i+\alpha,j+\beta,k} - w_2^{i,j,k} \right) \right] \\
&\quad + \frac{\chi}{8} \sum_{\alpha,\beta,\gamma=\pm 1} \left[\alpha\beta\eta_x\eta_y \left(\tilde{S}_{12} - \tilde{S}_{66} \right) \left(w_2^{i,j+\beta,k} - w_2^{i+\alpha,j,k} \right) \right] \\
&\quad + \frac{\chi}{8} \sum_{\alpha,\beta,\gamma=\pm 1} \left[\alpha\gamma\eta_x\eta_z \left(\tilde{S}_{13} + \tilde{S}_{55} \right) \left(w_3^{i+\alpha,j,k+\gamma} - w_3^{i,j,k} \right) \right] \\
&\quad + \frac{\chi}{8} \sum_{\alpha,\beta,\gamma=\pm 1} \left[\alpha\gamma\eta_x\eta_z \left(\tilde{S}_{13} - \tilde{S}_{55} \right) \left(w_3^{i,j,k+\gamma} - w_3^{i+\alpha,j,k} \right) \right] \\
&\quad - \frac{2\chi}{8} \sum_{\alpha,\beta,\gamma=\pm 1} \left[\alpha\beta\eta_x\eta_y \tilde{S}_{16} \left(w_1^{i,j,k} - w_1^{i+\alpha,j+\beta,k} \right) \right] \\
&\quad - \frac{2\chi}{8} w_2^{i,j,k} \sum_{\alpha,\beta,\gamma=\pm 1} \left[\eta_x^2 \tilde{S}_{16} + \eta_y^2 \tilde{S}_{26} \right] \\
&\quad - \frac{\chi}{8} \sum_{\alpha,\beta,\gamma=\pm 1} \left[\beta\gamma\eta_y\eta_z \left(\tilde{S}_{36} + \tilde{S}_{45} \right) w_3^{i,j,k} \right] \\
&\quad + \frac{2\chi}{8} \sum_{\alpha,\beta,\gamma=\pm 1} \left[\eta_x^2 \tilde{S}_{16} w_2^{i+\alpha,j,k} + \eta_y^2 \tilde{S}_{26} w_2^{i,j+\beta,k} \right] \\
&\quad + \frac{\chi}{8} \sum_{\alpha,\beta,\gamma=\pm 1} \left[\beta\gamma\eta_y\eta_z \tilde{S}_{36} \left(w_3^{i,j+\beta,k+\gamma} + w_3^{i,j,k+\gamma} - w_3^{i,j+\beta,k} \right) \right] \\
&\quad + \frac{\chi}{8} \sum_{\alpha,\beta,\gamma=\pm 1} \left[\beta\gamma\eta_y\eta_z \tilde{S}_{45} \left(w_3^{i,j+\beta,k+\gamma} - w_3^{i,j,k+\gamma} + w_3^{i,j+\beta,k} \right) \right] \\
&\quad + \frac{2\chi}{8} \sum_{\alpha,\beta,\gamma=\pm 1} \left[\eta_z^2 \tilde{S}_{45} \left(w_2^{i,j,k+\gamma} - w_2^{i,j,k} \right) \right]
\end{aligned} \tag{2.14}$$

$$\begin{aligned}
w_2^{i,j,k,t+1} = & -w_2^{i,j,k,t-1} + 2w_2^{i,j,k} \\
& - \frac{2\chi}{8} w_2^{i,j,k} \sum_{\alpha,\beta,\gamma=\pm 1} \left[\eta_x^2 \tilde{S}_{66} + \eta_y^2 \tilde{S}_{22} + \eta_z^2 \tilde{S}_{44} \right] \\
& + \frac{\chi}{8} \sum_{\alpha,\beta,\gamma=\pm 1} \left[2\eta_x^2 \tilde{S}_{66} w_2^{i+\alpha,j,k} + 2\eta_y^2 \tilde{S}_{22} w_2^{i,j+\beta,k} + 2\eta_z^2 \tilde{S}_{44} w_2^{i,j,k+\gamma} \right] \\
& + \frac{\chi}{8} \sum_{\alpha,\beta,\gamma=\pm 1} \left[\alpha\beta\eta_x\eta_y \left(\tilde{S}_{12} + \tilde{S}_{66} \right) \left(w_1^{i+\alpha,j+\beta,k} - w_1^{i,j,k} \right) \right] \\
& + \frac{\chi}{8} \sum_{\alpha,\beta,\gamma=\pm 1} \left[\alpha\beta\eta_x\eta_y \left(\tilde{S}_{12} - \tilde{S}_{66} \right) \left(w_1^{i+\alpha,j,k} - w_1^{i,j+\beta,k} \right) \right] \\
& + \frac{\chi}{8} \sum_{\alpha,\beta,\gamma=\pm 1} \left[\beta\gamma\eta_y\eta_z \left(\tilde{S}_{23} + \tilde{S}_{44} \right) \left(w_3^{i,j+\beta,k+\gamma} - w_3^{i,j,k} \right) \right] \\
& + \frac{\chi}{8} \sum_{\alpha,\beta,\gamma=\pm 1} \left[\beta\gamma\eta_y\eta_z \left(\tilde{S}_{23} - \tilde{S}_{44} \right) \left(w_3^{i,j,k+\gamma} - w_3^{i,j+\beta,k} \right) \right] \\
& - \frac{2\chi}{8} \sum_{\alpha,\beta,\gamma=\pm 1} \left[\alpha\beta\eta_x\eta_y \tilde{S}_{26} \left(w_2^{i,j,k} - w_2^{i+\alpha,j+\beta,k} \right) \right] \\
& - \frac{2\chi}{8} w_1^{i,j,k} \sum_{\alpha,\beta,\gamma=\pm 1} \left[\eta_x^2 \tilde{S}_{16} + \eta_y^2 \tilde{S}_{26} \right] \\
& + \frac{2\chi}{8} \sum_{\alpha,\beta,\gamma=\pm 1} \left[\eta_x^2 \tilde{S}_{16} w_1^{i+\alpha,j,k} + \eta_y^2 \tilde{S}_{26} w_1^{i,j+\beta,k} \right] \\
& - \frac{\chi}{8} \sum_{\alpha,\beta,\gamma=\pm 1} \left[\alpha\gamma\eta_x\eta_z \left(\tilde{S}_{36} + \tilde{S}_{45} \right) w_3^{i,j,k} \right] \\
& + \frac{\chi}{8} \sum_{\alpha,\beta,\gamma=\pm 1} \left[\alpha\gamma\eta_x\eta_z \tilde{S}_{36} \left(w_3^{i+\alpha,j,k+\gamma} + w_3^{i,j,k+\gamma} - w_3^{i+\alpha,j,k} \right) \right] \\
& + \frac{\chi}{8} \sum_{\alpha,\beta,\gamma=\pm 1} \left[\alpha\gamma\eta_x\eta_z \tilde{S}_{45} \left(w_3^{i+\alpha,j,k+\gamma} - w_3^{i,j,k+\gamma} + w_3^{i+\alpha,j,k} \right) \right] \\
& + \frac{2\chi}{8} \sum_{\alpha,\beta,\gamma=\pm 1} \left[\eta_z^2 \tilde{S}_{45} \left(w_1^{i,j,k+\gamma} - w_1^{i,j,k} \right) \right]
\end{aligned} \tag{2.15}$$

$$\begin{aligned}
w_3^{i,j,k,t+1} = & -w_3^{i,j,k,t-1} + 2w_3^{i,j,k} \\
& - \frac{2\chi}{8} w_3^{i,j,k} \sum_{\alpha,\beta,\gamma=\pm 1} \left[\eta_x^2 \tilde{S}_{55} + \eta_y^2 \tilde{S}_{44} + \eta_z^2 \tilde{S}_{33} \right] \\
& + \frac{\chi}{8} \sum_{\alpha,\beta,\gamma=\pm 1} \left[2\eta_x^2 \tilde{S}_{55} w_3^{i+\alpha,j,k} + 2\eta_y^2 \tilde{S}_{44} w_3^{i,j+\beta,k} + 2\eta_z^2 \tilde{S}_{33} w_3^{i,j,k+\gamma} \right] \\
& + \frac{\chi}{8} \sum_{\alpha,\beta,\gamma=\pm 1} \left[\beta\gamma\eta_y\eta_z \left(\tilde{S}_{23} + \tilde{S}_{44} \right) \left(w_2^{i,j+\beta,k+\gamma} - w_2^{i,j,k} \right) \right] \\
& + \frac{\chi}{8} \sum_{\alpha,\beta,\gamma=\pm 1} \left[\beta\gamma\eta_y\eta_z \left(\tilde{S}_{23} - \tilde{S}_{44} \right) \left(w_2^{i,j+\beta,k} - w_2^{i,j,k+\gamma} \right) \right] \\
& + \frac{\chi}{8} \sum_{\alpha,\beta,\gamma=\pm 1} \left[\alpha\gamma\eta_x\eta_z \left(\tilde{S}_{13} + \tilde{S}_{55} \right) \left(w_1^{i+\alpha,j,k+\gamma} - w_1^{i,j,k} \right) \right] \\
& + \frac{\chi}{8} \sum_{\alpha,\beta,\gamma=\pm 1} \left[\alpha\gamma\eta_x\eta_z \left(\tilde{S}_{13} - \tilde{S}_{55} \right) \left(w_1^{i+\alpha,j,k} - w_1^{i,j,k+\gamma} \right) \right] \\
& - \frac{\chi}{8} \sum_{\alpha,\beta,\gamma=\pm 1} \left[\beta\gamma\eta_y\eta_z \left(\tilde{S}_{36} + \tilde{S}_{45} \right) \left(w_1^{i,j,k} - w_1^{i,j+\beta,k+\gamma} \right) \right] \\
& - \frac{\chi}{8} \sum_{\alpha,\beta,\gamma=\pm 1} \left[\alpha\gamma\eta_x\eta_z \left(\tilde{S}_{36} + \tilde{S}_{45} \right) \left(w_2^{i,j,k} - w_2^{i+\alpha,j,k+\gamma} \right) \right] \\
& - \frac{\chi}{8} \sum_{\alpha,\beta,\gamma=\pm 1} \left[\beta\gamma\eta_y\eta_z \left(\tilde{S}_{36} - \tilde{S}_{45} \right) \left(w_1^{i,j,k+\gamma} - w_1^{i,j+\beta,k} \right) \right] \\
& - \frac{\chi}{8} \sum_{\alpha,\beta,\gamma=\pm 1} \left[\alpha\gamma\eta_x\eta_z \left(\tilde{S}_{36} - \tilde{S}_{45} \right) \left(w_2^{i,j,k+\gamma} - w_2^{i+\alpha,j,k} \right) \right] \\
& + \frac{2\chi}{8} \sum_{\alpha,\beta,\gamma=\pm 1} \left[\alpha\beta\eta_x\eta_y \tilde{S}_{45} \left(w_3^{i+\alpha,j+\beta,k} - w_3^{i,j,k} \right) \right]
\end{aligned} \tag{2.16}$$

where $\eta_x = 1/\Delta x_1^\alpha$, $\eta_y = 1/\Delta x_2^\beta$, $\eta_z = 1/\Delta x_3^\gamma$, and Δx_1^α , Δx_2^β , and Δx_3^γ are the spatial steps along X_1 , X_2 and X_3 axes (Fig. 2.5(a)), respectively. The current time t is assumed where it is not mentioned. $\tilde{S}_{11} = S_{11}(i + \alpha, j + \beta, k + \gamma)$ represents one of the eight cells surrounding the point C depending on the choice of (α, β, γ) from $(+1, -1)$, and similar expressions hold for the other stiffness terms. $\chi = (\Delta t^2/\bar{\rho})$, where Δt is the time step used in the simulation and $\bar{\rho}$ is the average density of all the eight cells surrounding point C as shown in Fig. 2.4. The part of the Eqs. 2.14-2.16 encapsulated in a color box represents the

newly introduced terms associated with the stiffness matrix rotation to capture laminated composites.

The parameters (cuboid grid sizes and time step) used in the discretization of the Eqs. 2.14-2.16 are selected based on the Courant-Friedrichs-Lewy (CFL) criterion. The CFL criterion is a constraint that bounds the time step and cell size by the relation:

$$\text{CFL} = c_{max} \Delta t \sqrt{\frac{1}{\Delta x_1^2} + \frac{1}{\Delta x_2^2} + \frac{1}{\Delta x_3^2}} \leq 1 \quad (2.17)$$

where c_{max} is the maximum wave speed. This criterion ensures proper capture of the wave propagation in time and space for a given time step and grid spacing. The spatial grid sizing should have at least 8 nodes per minimum wavelength, and according to Ref. [120], it is also recommended to have an upper limit of 20 nodes per wavelength to avoid excessively long run times and truncation errors. One important thing to note about c_{max} is that, it is the maximum wave velocity that is aimed to be captured. In most of the cases, it is safe to assume that the propagating wave speeds are lower than the maximum bulk velocity of the material system, i.e.,

$$c_{max} = \sqrt{S_{max}/\rho} \quad (2.18)$$

where S_{max} is the component of stiffness along the stiffest direction.

2.2.4 Guided Wave Generation in Prescribed Displacement LISA

As presented in Chapter 1, piezoelectric materials bonded to the surface or embedded in the structure are the most commonly used excitation methods. The PZT wafers (Fig. 2.6) are usually bonded onto the surface of the substrate to generate GW, as illustrated in Fig. 2.7.

In LISA, the input excitation has been traditionally modeled with prescribed displacements (PDs). A predetermined displacement pattern was enforced on the nodes constituting

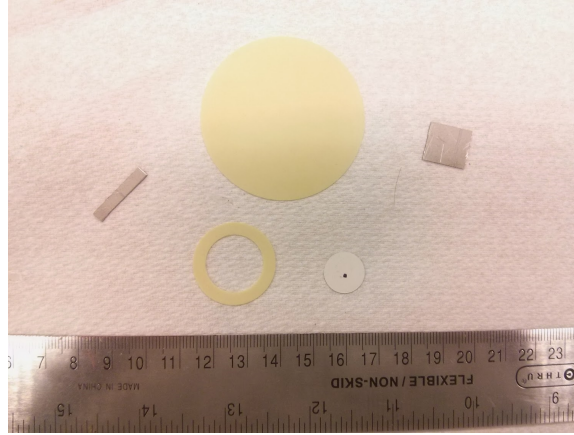


Figure 2.6: PZT wafers usually used for GW generation.

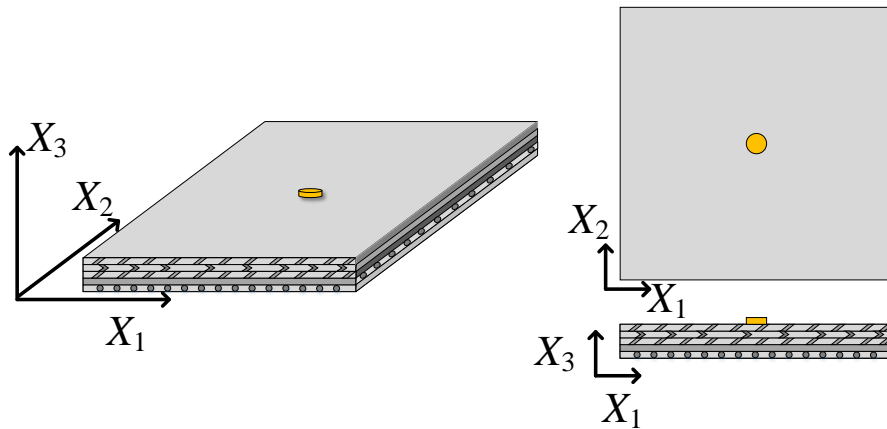
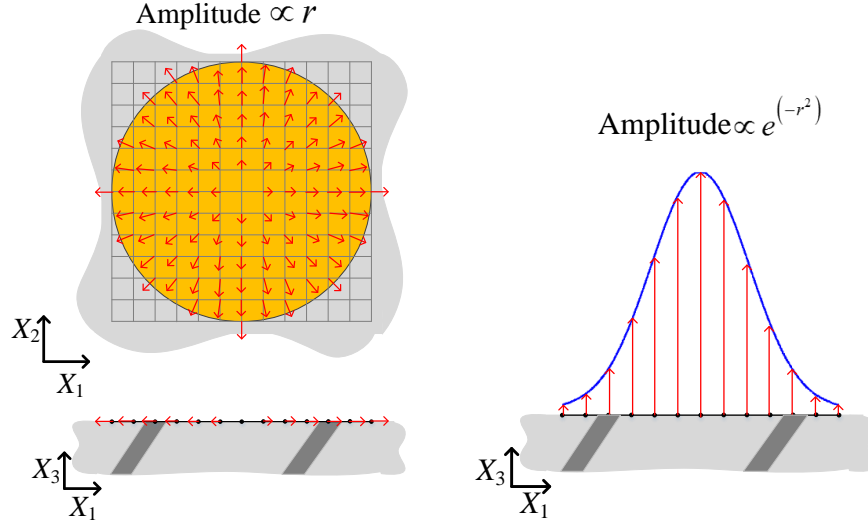


Figure 2.7: Schematic of PZT disc bonded on the top surface of a substrate for GW generation.

the actuator; more specifically, a 2D Gaussian energy distribution was considered for the input excitation [49, 106, 121]. This distribution translates into an out-of-plane distribution as shown in Fig. 2.8(b). More recently Nadella and Cesnik [122] implemented an in-plane PD field to model the transducer excitation as seen in Fig. 2.8(a). The direction of the PD for in-plane excitation is radial, and the magnitude is proportional to the distance from the center of the actuator. The in-plane PD takes into account the “pinching” effect [123] of the actuator which makes it a better representation of the piezoelectric effects than the out-of-plane displacement model.



(a) Prescribed displacements method-I (b) Prescribed displacements method-II

Figure 2.8: Different modeling schemes for piezoelectric actuators.

2.3 UM-LISA: Piezo-coupled Formulation

Traditionally, the representation of a surface-mounted piezoelectric actuator to generate GW in LISA has been achieved by imposing PD [49, 122, 124]. Although PD-based LISA formulation captured the essence of the GW propagation, it over-simplifies the GW generation by not accounting for the electromechanical coupling between the piezoelectric transducer and the substrate. Additionally, the anisotropic nature of the composite substrate is not accounted for while prescribing the predefined displacement patterns as an equivalent transducer response. In this section, LISA's capability is extended to model the actuator effects by accounting for piezoelectric material characteristics. This is achieved by including the electromechanical coupling in the governing equilibrium equations, and enforcing the coupling of the electrical and mechanical parameters by utilizing appropriate constitutive and compatibility conditions. The final iterative equations calculate mechanical displacements in an explicit time-marching manner, whereas the electric potentials are calculated using an implicit scheme. The overview of the different steps in the formulation

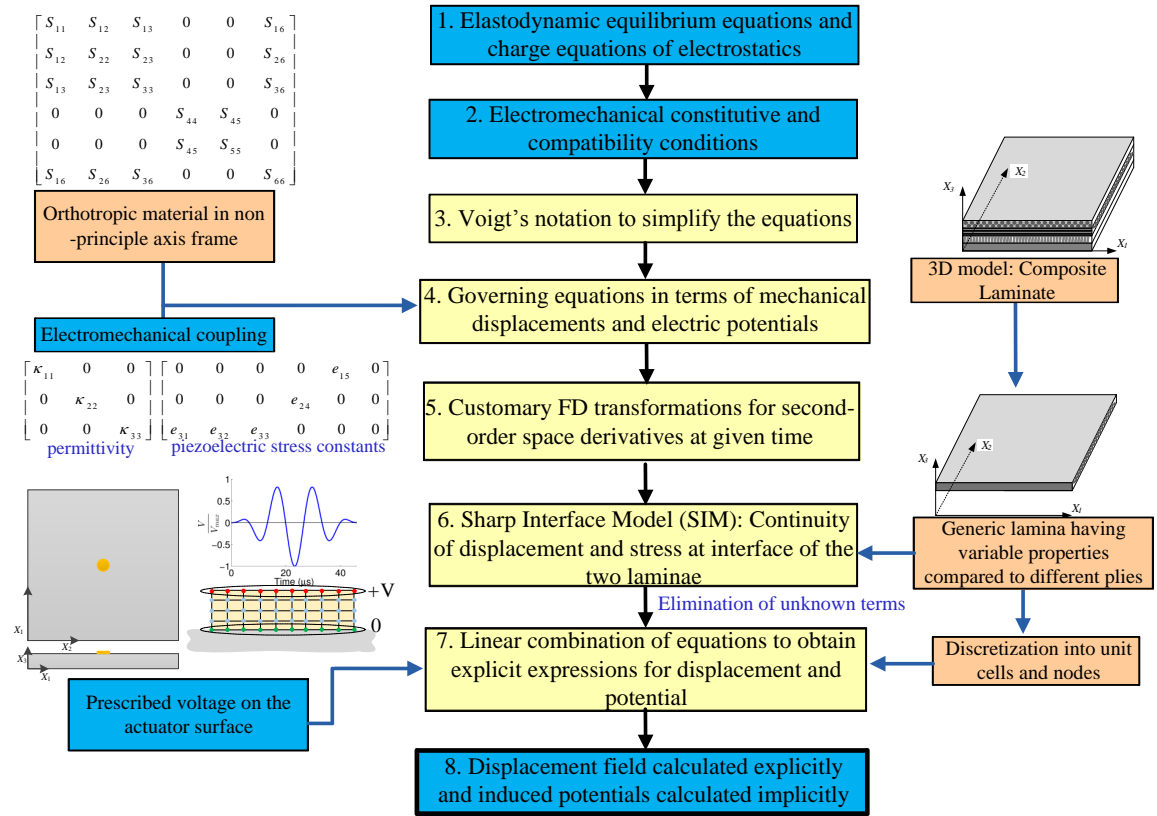


Figure 2.9: Overview of piezo-coupled UM-LISA formulation. The blue colored boxes represent the modifications to include electromechanical coupling.

is presented in the Fig. 2.9.

2.3.1 Governing Equations

Following the path similar to the basic LISA development as shown in Sec. 2.2.1, we begin with the elastodynamic equilibrium equations and the charge equations for electrostatics [125]:

$$\partial_t(\tau_{kl}) = \rho \ddot{w}_k \quad (k = 1, 2, 3) \quad (2.19)$$

$$\partial_t(D_l) = 0$$

where τ_{kl} is the stress tensor, D_l is the electric displacement, and the $\ddot{}$ represents double differentiation with respect to time. The two constitutive relations for mechanical-piezoelectric coupling are:

$$\tau_{kl} = S_{klmn}^E \varepsilon_{mn} - e_{klm} E_m \quad (2.20)$$

$$D_k = e_{klm} \varepsilon_{lm} + \kappa_{kl}^S E_l$$

where S_{klmn}^E is the stiffness tensor at constant electric field, ε_{mn} is the strain tensor, E_m is the electric field, κ_{kl}^S is the permittivity at constant strain, e_{klm} is the tensor of piezoelectric stress constants, and k, l, m and n are the indices for the tensors and vectors with a range of values 1, 2 and 3. The linear strain-mechanical displacement relations and the electric field-electric potential relations are given as:

$$\varepsilon_{kl} = \frac{1}{2} (w_{k,l} + w_{l,k}) \quad (2.21)$$

$$E_l = -\psi_{,l}$$

where ψ is the electric potential. From this point onward, the superscripts for the tensors are dropped for convenience. Voigt's notation, represented by 'V', is used to simplify the notation during the analysis, resulting in:

$$\begin{aligned}
S_{V(kl)V(mn)}w_{m,nl} + e_{V(kl)m}\psi_{,ml} &= \rho\ddot{w}_k \\
e_{kV(mn)}w_{m,nk} - \kappa_{km}\psi_{,mk} &= 0
\end{aligned} \tag{2.22}$$

As stated before, Einstein notation is used to represent summation of repeated indices. For the current analysis, the mechanical material properties are considered for a generic orthotropic medium with in-plane rotation as shown in the Sec. 2.2.1 and electro-mechanical properties for standard piezoelectric material, that is:

$$\begin{aligned}
[S_{V(kl)V(mn)}] &= \begin{bmatrix} S_{11} & S_{12} & S_{13} & 0 & 0 & S_{16} \\ S_{12} & S_{22} & S_{23} & 0 & 0 & S_{26} \\ S_{13} & S_{23} & S_{33} & 0 & 0 & S_{36} \\ 0 & 0 & 0 & S_{44} & S_{45} & 0 \\ 0 & 0 & 0 & S_{45} & S_{55} & 0 \\ S_{16} & S_{26} & S_{36} & 0 & 0 & S_{66} \end{bmatrix} \\
[e_{kV(mn)}] &= \begin{bmatrix} 0 & 0 & 0 & 0 & e_{15} & 0 \\ 0 & 0 & 0 & e_{24} & 0 & 0 \\ e_{31} & e_{32} & e_{33} & 0 & 0 & 0 \end{bmatrix} \\
[\kappa_{kl}] &= \begin{bmatrix} \kappa_{11} & 0 & 0 \\ 0 & \kappa_{22} & 0 \\ 0 & 0 & \kappa_{33} \end{bmatrix}
\end{aligned} \tag{2.23}$$

2.3.2 Discretization, Finite Difference Transformations, and Sharp Interface Model

Most of the 3D structures can be discretized into nodes and unit cells as shown in Fig. 2.3. As mentioned in Sec. 2.2.2, a given unit cell has unique material properties, so it cannot span across different layers, and to resolve the double spatial derivatives in space using FD transformations, all eighteen nearest-neighboring points around a given point C (as shown in Fig. 2.4) are required. Non-uniform spatial discretization is considered for the current derivation. Unlike homogeneous materials, heterogeneous materials require SIM to resolve the double spatial derivatives in space into recursive relations. The SIM enforces the continuity of stress field and displacement field across the interface cells. Similarly, in this formulation, the SIM is extended to the continuity of electric displacement and potentials. The extra conditions provided by the SIM incorporate the changes in mechanical and electrical properties into the iterative equations [126].

To ensure the continuity of mechanical displacements and potentials, in addition to the point C and its eighteen nearest neighbors (Fig. 2.5(a)), eight points are considered as shown in Fig. 2.5(a) at a distance of $\delta \ll \Delta x_i$ ($i=1,2,3$), given by $(i + \alpha\delta, j + \beta\delta, k + \gamma\delta)$ for $\alpha, \beta, \gamma = \pm 1$. Equation 2.22 can be represented as:

$$\begin{aligned}
 S_{V(kl)V(mn)}^{i+\alpha\delta, j+\beta\delta, k+\gamma\delta} w_{m, nl}^{i+\alpha\delta, j+\beta\delta, k+\gamma\delta} + e_{V(kl)m}^{i+\alpha\delta, j+\beta\delta, k+\gamma\delta} \psi_{, ml}^{i+\alpha\delta, j+\beta\delta, k+\gamma\delta} &= \rho \ddot{w}_k^{i+\alpha\delta, j+\beta\delta, k+\gamma\delta} \\
 e_{kV(mn)}^{i+\alpha\delta, j+\beta\delta, k+\gamma\delta} w_{m, nk}^{i+\alpha\delta, j+\beta\delta, k+\gamma\delta} - \kappa_{km}^{i+\alpha\delta, j+\beta\delta, k+\gamma\delta} \psi_{, mk}^{i+\alpha\delta, j+\beta\delta, k+\gamma\delta} &= 0
 \end{aligned} \tag{2.24}$$

The finite difference expressions used in the derivation are shown only for ψ , as the expressions for w_k ($k = 1, 2, 3$) are presented in Sec. 2.2.3. The resulting equations can be combined at these new points while the right-hand side of the equations are enforced to be

the same at the eight surrounding points to obtain the continuity of mechanical displacements and potentials. The second-order derivatives in Eq. 2.24 are resolved as:

$$\begin{aligned}
\psi_{x_1 x_1}^{i+\alpha\delta, j+\beta\delta, k+\gamma\delta} &= \frac{\psi_{x_1}^{i+\alpha/2, j, k} - \psi_{x_1}^{i+\alpha\delta, j+\beta\delta, k+\gamma\delta}}{\alpha\Delta x_1^\alpha/2} \\
\psi_{x_2 x_2}^{i+\alpha\delta, j+\beta\delta, k+\gamma\delta} &= \frac{\psi_{x_2}^{i, j+\beta/2, k} - \psi_{x_2}^{i+\alpha\delta, j+\beta\delta, k+\gamma\delta}}{\beta\Delta x_2^\beta/2} \\
\psi_{x_3 x_3}^{i+\alpha\delta, j+\beta\delta, k+\gamma\delta} &= \frac{\psi_{x_3}^{i, j, k+\gamma/2} - \psi_{x_3}^{i+\alpha\delta, j+\beta\delta, k+\gamma\delta}}{\gamma\Delta x_3^\gamma/2} \\
\psi_{x_1 x_2}^{i+\alpha\delta, j+\beta\delta, k+\gamma\delta} &= \frac{\psi^{i+\alpha, j+\beta, k} - \psi^{i+\alpha, j, k} - \psi^{i, j+\beta, k} + \psi^{i, j, k}}{\alpha\beta\Delta x_1^\alpha\Delta x_2^\beta} \\
\psi_{x_2 x_3}^{i+\alpha\delta, j+\beta\delta, k+\gamma\delta} &= \frac{\psi^{i, j+\beta, k+\gamma} - \psi^{i, j+\beta, k} - \psi^{i, j, k+\gamma} + \psi^{i, j, k}}{\beta\gamma\Delta x_2^\beta\Delta x_3^\gamma} \\
\psi_{x_3 x_1}^{i+\alpha\delta, j+\beta\delta, k+\gamma\delta} &= \frac{\psi^{i+\alpha, j, k+\gamma} - \psi^{i+\alpha, j, k} - \psi^{i, j, k+\gamma} + \psi^{i, j, k}}{\alpha\gamma\Delta x_1^\alpha\Delta x_3^\gamma}
\end{aligned} \tag{2.25}$$

The first-order derivatives in Eq. 2.25 are resolved as:

$$\begin{aligned}
\psi_{x_1}^{i+\alpha/2, j, k} &= \frac{\psi^{i+\alpha, j, k} - \psi^{i, j, k}}{\alpha\Delta x_1^\alpha} \\
\psi_{x_2}^{i, j+\beta/2, k} &= \frac{\psi^{i, j+\beta, k} - \psi^{i, j, k}}{\beta\Delta x_2^\beta} \\
\psi_{x_3}^{i, j, k+\gamma/2} &= \frac{\psi^{i, j, k+\gamma} - \psi^{i, j, k}}{\gamma\Delta x_3^\gamma}
\end{aligned} \tag{2.26}$$

It should be noted that the first derivative of $\psi^{i+\alpha\delta, j+\beta\delta, k+\gamma\delta}$ for $\alpha, \beta, \gamma = \pm 1$ remains unevaluated and are eliminated when the electric displacement continuity is enforced. To obtain continuity of stress and electric displacement, additional points are introduced: $(i + \alpha\epsilon, j + \beta\delta, k + \gamma\delta)$, $(i + \alpha\delta, j + \beta\epsilon, k + \gamma\delta)$ and $(i + \alpha\delta, j + \beta\delta, k + \gamma\epsilon)$ with $\epsilon \ll \delta \ll x_i$ represented as black squares in Fig. 2.5(b). The derivatives at these additional points are resolved as:

$$\begin{aligned}
\psi_{x_1}^{i+\alpha\varepsilon, j+\beta\delta, k+\gamma\delta} &= \psi_{x_1}^{i+\alpha\delta, j+\beta\delta, k+\gamma\delta} \\
\psi_{x_2}^{i+\alpha\delta, j+\beta\varepsilon, k+\gamma\delta} &= \psi_{x_2}^{i+\alpha\delta, j+\beta\delta, k+\gamma\delta} \\
\psi_{x_3}^{i+\alpha\delta, j+\beta\delta, k+\gamma\varepsilon} &= \psi_{x_3}^{i+\alpha\delta, j+\beta\delta, k+\gamma\delta} \\
\psi_{x_1}^{i+\alpha\delta, j+\beta\varepsilon, k+\gamma\delta} &= \psi_{x_1}^{i+\alpha\delta, j+\beta\delta, k+\gamma\varepsilon} = \frac{\psi^{i+\alpha, j, k} - \psi^{i, j, k}}{\alpha\Delta x_1^\alpha} \\
\psi_{x_2}^{i+\alpha\varepsilon, j+\beta\delta, k+\gamma\delta} &= \psi_{x_2}^{i+\alpha\delta, j+\beta\delta, k+\gamma\varepsilon} = \frac{\psi^{i, j+\beta, k} - \psi^{i, j, k}}{\beta\Delta x_2^\beta} \\
\psi_{x_3}^{i+\alpha\varepsilon, j+\beta\delta, k+\gamma\delta} &= \psi_{x_3}^{i+\alpha\delta, j+\beta\varepsilon, k+\gamma\delta} = \frac{\psi^{i, j, k+\gamma} - \psi^{i, j, k}}{\gamma\Delta x_3^\gamma}
\end{aligned} \tag{2.27}$$

It should be noted that in the manner discussed previously, the first derivative mechanical displacement and electric potential terms at the eight points shown in Fig. 2.5(a) remain unevaluated and are eliminated based on the stress and electric displacement continuity relations given as:

$$\begin{aligned}
\tau_{p1}^{i+\varepsilon, j+\beta\delta, k+\gamma\delta} &= \tau_{p1}^{i-\varepsilon, j+\beta\delta, k+\gamma\delta} \\
\tau_{p2}^{i+\alpha\delta, j+\varepsilon, k+\gamma\delta} &= \tau_{p2}^{i+\alpha\delta, j-\varepsilon, k+\gamma\delta} \quad (p = 1, 2, 3) \\
\tau_{p3}^{i+\alpha\delta, j+\beta\delta, k+\varepsilon} &= \tau_{p3}^{i+\alpha\delta, j+\beta\delta, k-\varepsilon} \\
D_1^{i+\varepsilon, j+\beta\delta, k+\gamma\delta} &= D_1^{i-\varepsilon, j+\beta\delta, k+\gamma\delta} \\
D_2^{i+\alpha\delta, j+\varepsilon, k+\gamma\delta} &= D_2^{i+\alpha\delta, j-\varepsilon, k+\gamma\delta} \\
D_3^{i+\alpha\delta, j+\beta\delta, k+\varepsilon} &= D_3^{i+\alpha\delta, j+\beta\delta, k-\varepsilon}
\end{aligned} \tag{2.28}$$

Using Eq. 2.8 at the eight surrounding points $(i + \alpha\delta, j + \beta\delta, k + \gamma\delta)$ and the select group of stress continuity relations given in Eq. 2.28 (details pertaining to the derivation can be found in the Appendix), the final IEs for the three-displacement components are derived for the 3D case as:

$$\begin{aligned}
w_1^{i,j,k,t+1} &= -w_1^{i,j,k,t-1} + 2w_1^{i,j,k} \\
&\quad - \frac{2\chi}{8} w_1^{i,j,k} \sum_{\alpha,\beta,\gamma=\pm 1} \left[\eta_x^2 \tilde{S}_{11} + \eta_y^2 \tilde{S}_{66} + \eta_z^2 \tilde{S}_{55} \right] \\
&\quad + \frac{\chi}{8} \sum_{\alpha,\beta,\gamma=\pm 1} \left[2\eta_x^2 \tilde{S}_{11} w_1^{i+\alpha,j,k} + 2\eta_y^2 \tilde{S}_{66} w_1^{i,j+\beta,k} + 2\eta_z^2 \tilde{S}_{55} w_1^{i,j,k+\gamma} \right] \\
&\quad + \frac{\chi}{8} \sum_{\alpha,\beta,\gamma=\pm 1} \left[\alpha\beta\eta_x\eta_y \left(\tilde{S}_{12} + \tilde{S}_{66} \right) \left(w_2^{i+\alpha,j+\beta,k} - w_2^{i,j,k} \right) \right] \\
&\quad + \frac{\chi}{8} \sum_{\alpha,\beta,\gamma=\pm 1} \left[\alpha\beta\eta_x\eta_y \left(\tilde{S}_{12} - \tilde{S}_{66} \right) \left(w_2^{i,j+\beta,k} - w_2^{i+\alpha,j,k} \right) \right] \\
&\quad + \frac{\chi}{8} \sum_{\alpha,\beta,\gamma=\pm 1} \left[\alpha\gamma\eta_x\eta_z \left(\tilde{S}_{13} + \tilde{S}_{55} \right) \left(w_3^{i+\alpha,j,k+\gamma} - w_3^{i,j,k} \right) \right] \\
&\quad + \frac{\chi}{8} \sum_{\alpha,\beta,\gamma=\pm 1} \left[\alpha\gamma\eta_x\eta_z \left(\tilde{S}_{13} - \tilde{S}_{55} \right) \left(w_3^{i,j,k+\gamma} - w_3^{i+\alpha,j,k} \right) \right] \\
&\quad - \frac{2\chi}{8} \sum_{\alpha,\beta,\gamma=\pm 1} \left[\alpha\beta\eta_x\eta_y \tilde{S}_{16} \left(w_1^{i,j,k} - w_1^{i+\alpha,j+\beta,k} \right) \right] \\
&\quad - \frac{2\chi}{8} w_2^{i,j,k} \sum_{\alpha,\beta,\gamma=\pm 1} \left[\eta_x^2 \tilde{S}_{16} + \eta_y^2 \tilde{S}_{26} \right] \\
&\quad - \frac{\chi}{8} \sum_{\alpha,\beta,\gamma=\pm 1} \left[\beta\gamma\eta_y\eta_z \left(\tilde{S}_{36} + \tilde{S}_{45} \right) w_3^{i,j,k} \right] \\
&\quad + \frac{2\chi}{8} \sum_{\alpha,\beta,\gamma=\pm 1} \left[\eta_x^2 \tilde{S}_{16} w_2^{i+\alpha,j,k} + \eta_y^2 \tilde{S}_{26} w_2^{i,j+\beta,k} \right] \\
&\quad + \frac{\chi}{8} \sum_{\alpha,\beta,\gamma=\pm 1} \left[\beta\gamma\eta_y\eta_z \tilde{S}_{36} \left(w_3^{i,j+\beta,k+\gamma} + w_3^{i,j,k+\gamma} - w_3^{i,j+\beta,k} \right) \right] \\
&\quad + \frac{\chi}{8} \sum_{\alpha,\beta,\gamma=\pm 1} \left[\beta\gamma\eta_y\eta_z \tilde{S}_{45} \left(w_3^{i,j+\beta,k+\gamma} - w_3^{i,j,k+\gamma} + w_3^{i,j+\beta,k} \right) \right] \\
&\quad + \frac{2\chi}{8} \sum_{\alpha,\beta,\gamma=\pm 1} \left[\eta_z^2 \tilde{S}_{45} \left(w_2^{i,j,k+\gamma} - w_2^{i,j,k} \right) \right] \\
&\quad + \frac{\chi}{8} \sum_{\alpha,\beta,\gamma=\pm 1} \left[\alpha\gamma\eta_x\eta_z \left(\tilde{e}_{15} + \tilde{e}_{31} \right) \left(\psi^{i+\alpha,j,k+\gamma} - \psi^{i,j,k} \right) \right] \\
&\quad - \frac{\chi}{8} \sum_{\alpha,\beta,\gamma=\pm 1} \left[\alpha\gamma\eta_x\eta_z \left(\tilde{e}_{15} - \tilde{e}_{31} \right) \left(\psi^{i,j,k+\gamma} - \psi^{i+\alpha,j,k} \right) \right]
\end{aligned} \tag{2.29}$$

$$\begin{aligned}
w_2^{i,j,k,t+1} &= -w_2^{i,j,k,t-1} + 2w_2^{i,j,k} \\
&\quad - \frac{2\chi}{8} w_2^{i,j,k} \sum_{\alpha,\beta,\gamma=\pm 1} \left[\eta_x^2 \tilde{S}_{66} + \eta_y^2 \tilde{S}_{22} + \eta_z^2 \tilde{S}_{44} \right] \\
&\quad + \frac{\chi}{8} \sum_{\alpha,\beta,\gamma=\pm 1} \left[2\eta_x^2 \tilde{S}_{66} w_2^{i+\alpha,j,k} + 2\eta_y^2 \tilde{S}_{22} w_2^{i,j+\beta,k} + 2\eta_z^2 \tilde{S}_{44} w_2^{i,j,k+\gamma} \right] \\
&\quad + \frac{\chi}{8} \sum_{\alpha,\beta,\gamma=\pm 1} \left[\alpha\beta\eta_x\eta_y \left(\tilde{S}_{12} + \tilde{S}_{66} \right) \left(w_1^{i+\alpha,j+\beta,k} - w_1^{i,j,k} \right) \right] \\
&\quad + \frac{\chi}{8} \sum_{\alpha,\beta,\gamma=\pm 1} \left[\alpha\beta\eta_x\eta_y \left(\tilde{S}_{12} - \tilde{S}_{66} \right) \left(w_1^{i+\alpha,j,k} - w_1^{i,j+\beta,k} \right) \right] \\
&\quad + \frac{\chi}{8} \sum_{\alpha,\beta,\gamma=\pm 1} \left[\beta\gamma\eta_y\eta_z \left(\tilde{S}_{23} + \tilde{S}_{44} \right) \left(w_3^{i,j+\beta,k+\gamma} - w_3^{i,j,k} \right) \right] \\
&\quad + \frac{\chi}{8} \sum_{\alpha,\beta,\gamma=\pm 1} \left[\beta\gamma\eta_y\eta_z \left(\tilde{S}_{23} - \tilde{S}_{44} \right) \left(w_3^{i,j,k+\gamma} - w_3^{i,j+\beta,k} \right) \right] \\
&\quad - \frac{2\chi}{8} \sum_{\alpha,\beta,\gamma=\pm 1} \left[\alpha\beta\eta_x\eta_y \tilde{S}_{26} \left(w_2^{i,j,k} - w_2^{i+\alpha,j+\beta,k} \right) \right] \\
&\quad - \frac{2\chi}{8} w_1^{i,j,k} \sum_{\alpha,\beta,\gamma=\pm 1} \left[\eta_x^2 \tilde{S}_{16} + \eta_y^2 \tilde{S}_{26} \right] \\
&\quad + \frac{2\chi}{8} \sum_{\alpha,\beta,\gamma=\pm 1} \left[\eta_x^2 \tilde{S}_{16} w_1^{i+\alpha,j,k} + \eta_y^2 \tilde{S}_{26} w_1^{i,j+\beta,k} \right] \\
&\quad - \frac{\chi}{8} \sum_{\alpha,\beta,\gamma=\pm 1} \left[\alpha\gamma\eta_x\eta_z \left(\tilde{S}_{36} + \tilde{S}_{45} \right) w_3^{i,j,k} \right] \\
&\quad + \frac{\chi}{8} \sum_{\alpha,\beta,\gamma=\pm 1} \left[\alpha\gamma\eta_x\eta_z \tilde{S}_{36} \left(w_3^{i+\alpha,j,k+\gamma} + w_3^{i,j,k+\gamma} - w_3^{i+\alpha,j,k} \right) \right] \\
&\quad + \frac{\chi}{8} \sum_{\alpha,\beta,\gamma=\pm 1} \left[\alpha\gamma\eta_x\eta_z \tilde{S}_{45} \left(w_3^{i+\alpha,j,k+\gamma} - w_3^{i,j,k+\gamma} + w_3^{i+\alpha,j,k} \right) \right] \\
&\quad + \frac{2\chi}{8} \sum_{\alpha,\beta,\gamma=\pm 1} \left[\eta_z^2 \tilde{S}_{45} \left(w_1^{i,j,k+\gamma} - w_1^{i,j,k} \right) \right] \\
&\quad + \frac{\chi}{8} \sum_{\alpha,\beta,\gamma=\pm 1} \left[\beta\gamma\eta_y\eta_z \left(\tilde{e}_{24} + \tilde{e}_{32} \right) \left(\psi^{i,j+\beta,k+\gamma} - \psi^{i,j,k} \right) \right] \\
&\quad - \frac{\chi}{8} \sum_{\alpha,\beta,\gamma=\pm 1} \left[\beta\gamma\eta_y\eta_z \left(\tilde{e}_{24} - \tilde{e}_{32} \right) \left(\psi^{i,j,k+\gamma} - \psi^{i,j+\beta,k} \right) \right]
\end{aligned} \tag{2.30}$$

$$\begin{aligned}
w_3^{i,j,k,t+1} &= -w_3^{i,j,k,t-1} + 2w_3^{i,j,k} \\
&\quad - \frac{2\chi}{8} w_3^{i,j,k} \sum_{\alpha,\beta,\gamma=\pm 1} \left[\eta_x^2 \tilde{S}_{55} + \eta_y^2 \tilde{S}_{44} + \eta_z^2 \tilde{S}_{33} \right] \\
&\quad + \frac{\chi}{8} \sum_{\alpha,\beta,\gamma=\pm 1} \left[2\eta_x^2 \tilde{S}_{55} w_3^{i+\alpha,j,k} + 2\eta_y^2 \tilde{S}_{44} w_3^{i,j+\beta,k} + 2\eta_z^2 \tilde{S}_{33} w_3^{i,j,k+\gamma} \right] \\
&\quad + \frac{\chi}{8} \sum_{\alpha,\beta,\gamma=\pm 1} \left[\beta\gamma\eta_y\eta_z \left(\tilde{S}_{23} + \tilde{S}_{44} \right) \left(w_2^{i,j+\beta,k+\gamma} - w_2^{i,j,k} \right) \right] \\
&\quad + \frac{\chi}{8} \sum_{\alpha,\beta,\gamma=\pm 1} \left[\beta\gamma\eta_y\eta_z \left(\tilde{S}_{23} - \tilde{S}_{44} \right) \left(w_2^{i,j+\beta,k} - w_2^{i,j,k+\gamma} \right) \right] \\
&\quad + \frac{\chi}{8} \sum_{\alpha,\beta,\gamma=\pm 1} \left[\alpha\gamma\eta_x\eta_z \left(\tilde{S}_{13} + \tilde{S}_{55} \right) \left(w_1^{i+\alpha,j,k+\gamma} - w_1^{i,j,k} \right) \right] \\
&\quad + \frac{\chi}{8} \sum_{\alpha,\beta,\gamma=\pm 1} \left[\alpha\gamma\eta_x\eta_z \left(\tilde{S}_{13} - \tilde{S}_{55} \right) \left(w_1^{i+\alpha,j,k} - w_1^{i,j,k+\gamma} \right) \right] \\
&\quad - \frac{\chi}{8} \sum_{\alpha,\beta,\gamma=\pm 1} \left[\beta\gamma\eta_y\eta_z \left(\tilde{S}_{36} + \tilde{S}_{45} \right) \left(w_1^{i,j,k} - w_1^{i,j+\beta,k+\gamma} \right) \right] \\
&\quad - \frac{\chi}{8} \sum_{\alpha,\beta,\gamma=\pm 1} \left[\alpha\gamma\eta_x\eta_z \left(\tilde{S}_{36} + \tilde{S}_{45} \right) \left(w_2^{i,j,k} - w_2^{i+\alpha,j,k+\gamma} \right) \right] \\
&\quad - \frac{\chi}{8} \sum_{\alpha,\beta,\gamma=\pm 1} \left[\beta\gamma\eta_y\eta_z \left(\tilde{S}_{36} - \tilde{S}_{45} \right) \left(w_1^{i,j,k+\gamma} - w_1^{i,j+\beta,k} \right) \right] \\
&\quad - \frac{\chi}{8} \sum_{\alpha,\beta,\gamma=\pm 1} \left[\alpha\gamma\eta_x\eta_z \left(\tilde{S}_{36} - \tilde{S}_{45} \right) \left(w_2^{i,j,k+\gamma} - w_2^{i+\alpha,j,k} \right) \right] \\
&\quad + \frac{2\chi}{8} \sum_{\alpha,\beta,\gamma=\pm 1} \left[\alpha\beta\eta_x\eta_y \tilde{S}_{45} \left(w_3^{i+\alpha,j+\beta,k} - w_3^{i,j,k} \right) \right] \\
&\quad - \frac{2\chi}{8} \sum_{\alpha,\beta,\gamma=\pm 1} \left[\left(\eta_x^2 \tilde{e}_{15} + \eta_y^2 \tilde{e}_{24} + \eta_z^2 \tilde{e}_{33} \right) \psi^{i,j,k} \right] \\
&\quad + \frac{2\chi}{8} \sum_{\alpha,\beta,\gamma=\pm 1} \left[\left(\eta_x^2 \tilde{e}_{15} \psi^{i+\alpha,j,k} + \eta_y^2 \tilde{e}_{24} \psi^{i,j+\beta,k} + \eta_z^2 \tilde{e}_{33} \psi^{i,j,k+\gamma} \right) \right]
\end{aligned} \tag{2.31}$$

The calculated mechanical displacement components are then used to calculate the induced potentials using Eq. 2.32:

$$F(\psi) = g(w_1, w_2, w_3) \quad (2.32)$$

where $F(\psi)$ and $g(w_1, w_2, w_3)$ are functions defined as:

$$\begin{aligned}
F(\psi) &= -2 \sum_{\alpha, \beta, \gamma = \pm 1} [(\eta_x^2 \tilde{\kappa}_{11} + \eta_y^2 \tilde{\kappa}_{22} + \eta_z^2 \tilde{\kappa}_{33}) \psi^{i, j, k}] \\
&\quad + 2 \sum_{\alpha, \beta, \gamma = \pm 1} [(\eta_x^2 \tilde{\kappa}_{11} \psi^{i+\alpha, j, k} + \eta_y^2 \tilde{\kappa}_{22} \psi^{i, j+\beta, k} + \eta_z^2 \tilde{\kappa}_{33} \psi^{i, j, k+\gamma})] \\
g(w_1, w_2, w_3) &= - \sum_{\alpha, \beta, \gamma = \pm 1} [\alpha \gamma \eta_x \eta_z (\tilde{e}_{15} + \tilde{e}_{31}) w_1^{i, j, k}] \\
&\quad + \sum_{\alpha, \beta, \gamma = \pm 1} [\alpha \gamma \eta_x \eta_z (\tilde{e}_{15} - \tilde{e}_{31}) (w_1^{i, j, k+\gamma} - w_1^{i+\alpha, j, k})] \\
&\quad - \sum_{\alpha, \beta, \gamma = \pm 1} [\beta \gamma \eta_y \eta_z (\tilde{e}_{24} + \tilde{e}_{32}) w_2^{i, j, k}] \\
&\quad + \sum_{\alpha, \beta, \gamma = \pm 1} [\beta \gamma \eta_y \eta_z (\tilde{e}_{24} - \tilde{e}_{32}) (w_2^{i, j, k+\gamma} - w_2^{i, j+\beta, k})] \\
&\quad - 2 \sum_{\alpha, \beta, \gamma = \pm 1} [(\eta_x^2 \tilde{e}_{15} + \eta_y^2 \tilde{e}_{24} + \eta_z^2 \tilde{e}_{33}) w_3^{i, j, k}] \\
&\quad + 2 \sum_{\alpha, \beta, \gamma = \pm 1} [(\eta_x^2 \tilde{e}_{15} w_3^{i+\alpha, j, k} + \eta_y^2 \tilde{e}_{24} w_3^{i, j+\beta, k} + \eta_z^2 \tilde{e}_{33} w_3^{i, j, k+\gamma})]
\end{aligned} \quad (2.33)$$

As before, the current time step t is assumed where it is not mentioned. $\tilde{e}_{15} = e_{15}(i + \alpha, j + \beta, k + \gamma)$ represents piezoelectric stress material property for one of the eight cells surrounding point C depending on the choice of (α, β, γ) from $(+1, -1)$ and similar expressions hold for other mechanical stiffness, piezoelectric stress matrix and permittivity terms. The parts of the equations encapsulated in the color boxes represent the additional terms in UM-LISA due to piezoelectric effects. It should be noted that Eqs. 2.29-2.31 are

solved explicitly whereas Eq. 2.32 should be solved implicitly for induced potentials.

2.3.3 Guided Wave Generation in UM-LISA

Although in-plane PD shown in Fig. 2.8(a) is a better representation of the input excitation than the out-of-plane PD (Fig. 2.8(b)), it does not take into account the mechanical and piezoelectric coupling between the actuator and the composite structure. This can now be addressed in UM-LISA formulation since it accounts for the aforementioned complex coupling effects. A discretized model of a PZT transducer is shown in Figure 2.10. The actuation is implemented by prescribing a time-varying electric potential on the top surface of the actuator (labeled as “Top Nodes” and shown as red nodes) and zero potential (ground) at the “Bottom Nodes” (shown as green nodes). The induced potentials at other nodes would be calculated, if present, in the problem.

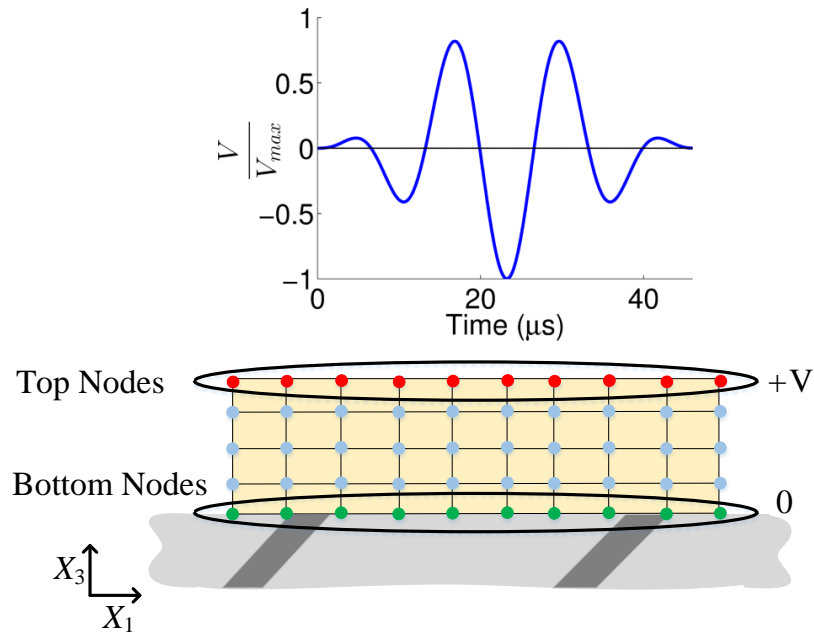


Figure 2.10: Modeling in UM-LISA for piezoelectric actuators.

2.4 Modeling for Guided Wave Sensing in UM-LISA

In the UM-LISA formulation, sensor response can be obtained either by calculating the in-plane strains based on the displacement field, or by implementing the piezo-coupled formulation to model the piezo electric sensor directly. The different schemes are illustrated in Fig. 2.11.

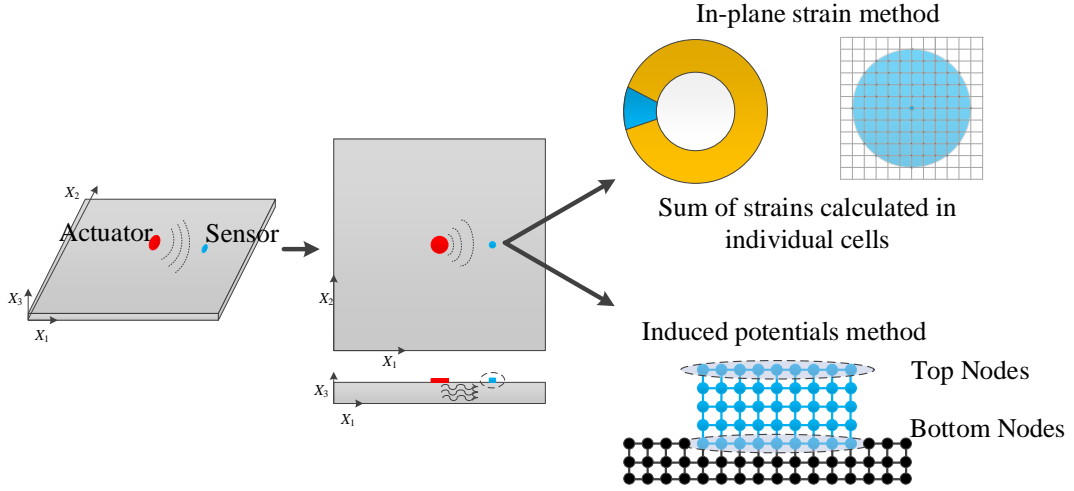


Figure 2.11: Different mechanisms for modeling sensors in the LISA formulation.

2.4.1 Basic Strain-based Sensor Modeling

For the basic UM-LISA method (without piezo coupling), the response for a piezo-sensor bonded on the surface of a plate can be derived by considering the relation between the electric field E_i , electric displacement D_k , and internal stress in the piezoelectric element [127]:

$$E_i = -g_{ikl}\tau_{kl} + \beta_{ik}^\tau D_k \quad (2.34)$$

where g_{ikl} represents the piezoelectric material matrix components, and β_{ik}^τ are the coefficients of the impermeability constant matrix at constant stress for the material. Following

the procedure presented by Raghavan and Cesnik [46], and making an assumption that the sensor is infinitely compliant and does not disturb the GW field, the output voltage response of the sensor can be written as:

$$V_s = \frac{V_0}{S_t} \int_{S_t} \varepsilon_{ii} dS \quad (2.35)$$

where V_s is the voltage generated by the sensor, S_t is the surface area of the transducer, and V_0 is a constant depending on piezoelectric and elastic sensor material properties [46]. For the case of a circular piezo-disc sensor, Eq. 2.35 can be written as:

$$V_s = \frac{V_0}{S_t} \int_{S_t} \int (\varepsilon_{rr} + \varepsilon_{\theta\theta}) r dr d\theta \quad (2.36)$$

where ε_{rr} and $\varepsilon_{\theta\theta}$ are the in-plane strain components expressed in polar coordinates (r and θ). The strain components are obtained by employing FD transformations on the displacement field calculated from UM-LISA.

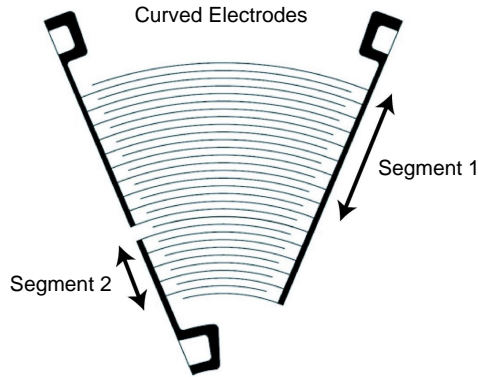


Figure 2.12: Sample curved electrodes used in the CLoVER construction.

Consider the extension of the derivation to a CLoVER sector (Fig. 2.12). The voltage generated by the normal radial normal strain component (ε_{rr}) along the fibers in a CLoVER sector of inner radius R_i , outer radius R_o , and azimuthal sector angle $\Delta\theta$ is given by:

$$V_s = \frac{2V_0}{(R_o^2 - R_i^2)\Delta\theta} \int_0^{\Delta\theta} \int_{R_i}^{R_o} \epsilon_{rr} r dr d\theta \quad (2.37)$$

Here, it is assumed that the electric field is uniform through the cross-section of the fibers, and the presence of the sensor is not affecting the wave field in the substrate or its voltage reading. Since UM-LISA calculates the displacement field in the Cartesian system, the along-the-fiber normal strain is calculated from the in-plane strain components (ϵ_{11} , ϵ_{22} , and ϵ_{12}) using the FD scheme and then rotating them based on the azimuthal position of the CLoVER sector. Radial (along-the-fibers) strains at the nodes which represent the CLoVER sector are calculated and summed to obtain the induced voltage.

2.4.2 Direct Piezo Coupled Field Modeling

One of the main advantages of UM-LISA is its ability to simulate the response of piezoelectric sensors. In UM-LISA modeling, along with the piezoelectric properties of the material, the electromechanical coupling effects between the transducer and the substrate are also considered. Induced potentials in the sensor are calculated using the Eq. 2.32, where the induced potentials in a piezoelectric region are a function of the mechanical displacement field. Since electrostatic behavior is considered in the formulation, the induced potentials are calculated using an implicit scheme (in contrast to the explicit, time-marching scheme to calculate the displacement field).

Equation 2.32 represents the relationship between the induced potentials and mechanical displacement field for a given node in the grid. By combining the equations for all the nodes capable of developing potentials (piezo-sensor nodes), one arrives at the following relation:

$$\Phi_{u \times u}^o \psi_{u \times 1}^o = \Theta_{u \times 1} \quad (2.38)$$

where $\Phi_{u \times u}^o$ is a matrix which is a function of material properties, $\psi_{u \times 1}^o$ is a vector of the unknown potentials, $\Theta_{u \times 1}$ is a vector which is a function of material properties and mechanical displacements, and u is the number of nodes with induced potentials. It should be noted that when solving for the induced potentials, the top and bottom surfaces of the sensor have constrained potentials because of the presence of electrodes. A vector transformation is used to include the additional constraints of unique potentials for the boundary nodes, as given by:

$$\psi_{n \times 1}^o = \Lambda_{u \times v} \psi_{v \times 1} \quad (2.39)$$

where v is the number of unique potentials to be calculated, and $\Lambda_{u \times v}$ is the transformation matrix. By using this transformation, and pre-multiplying Eq. 2.38 with the transpose of the transformation vector, a reduced set of equations is obtained, which accounts for the additional constraints in the induced potential field, i.e.,

$$\Lambda_{v \times u}^T \Phi_{u \times u}^o \Lambda_{u \times v} \psi_{v \times 1} = \Lambda_{v \times u}^T \Theta_{u \times 1} \quad (2.40)$$

It should also be noted that the size of the matrices involved in the implicit scheme to calculate the induced potentials tend to be large and solving the implicit equation by matrix inversion is extremely inefficient. A standard mathematical approach (LU decomposition) is utilized to efficiently calculate the induced potentials by employing the back substitution method during the advancement of iterative equations.

CHAPTER 3

Numerical Framework

This chapter presents an overview of the numerical implementation of the new formulation created for UM-LISA. A history of the LISA framework development is presented. The architecture of the code is introduced with the help of a block diagram highlighting different modules with UM-LISA. This chapter aims to present the code in a step-wise fashion to describe the structure of the setup and expedite future developments to the framework.

3.1 Development

As discussed in Chapter 1, the LISA formulation was first introduced by Delsanto and co-workers. The formulation was first presented for 1D LISA [91] in 1992, and subsequently the 2D LISA [67] and 3D LISA [92] were introduced in 1994 and 1997, respectively. The derived equations were capable of modeling homogenous and non-homogeneous orthotropic media in principal reference frame. One of the initial motivations for the development of LISA was its capability of being used as a highly parallelized numerical tool for wave propagation. This was achieved by “teaching” the individual nodes in the numerical model the rules for displacement based on the displacement profile of the few nearest neighboring nodes at previous two time steps. This enabled the calculation of the displacement field over the whole domain with knowledge of the displacements at the two previous time steps. The original LISA formulation was later extended to include

spring model-based LISA [128, 129], which addresses the issues of flawed interfaces and attenuative, nonlinear and hysteretic media.

Subsequently, the framework was adopted and implemented by several researchers, such as Agostini et al. [93, 94], to model orthotropic structures in principal-reference frame, and by Lee and Staszewski [49, 95] to model GW propagation and damage interaction in isotropic structures using the 2D LISA formulation.

In 2008, the 3D LISA framework was extended by Sundararaman and Adams [106] to model orthotropic media with non-uniform spatial discretizations and with a visco-elastic damping term. Although this LISA formulation has the potential for a wide range of application, it was primarily utilized to model GW propagation and damage interaction in isotropic plates with uniform spatial discretization. The GW propagation and damage interaction studies with composites were limited to an orthotropic layer rather than a laminate.

In 2013, Nadella and Cesnik [122] extended the LISA formulation to model 3D laminated orthotropic structures with nonuniform cell aspect ratios and in a non-principal axis frame, which benefits from modeling generic laminated composite materials. New coupling stiffness terms populate the stiffness matrix because of the material axis rotation and are accounted for in the derivation of the equations.

Recently, Nadella and Cesnik [126] extended the formulation even further to model the actuator by implementing the piezoelectric material effects. The iterative equations were extended to include piezoelectric materials, taking into account the electromechanical coupling of the governing equilibrium equations. New constitutive and compatibility conditions are considered to account for the coupling of the electrical and mechanical parameters. The iterative equations calculate mechanical displacements in an explicit time-marching scheme, whereas the electric potentials are calculated using an implicit scheme.

3.2 Architecture

Figure 3.1 presents an overview of the implementation of the UM-LISA framework. The multi-physics numerical framework has been developed with the help of modules and sub-routines performing various tasks in the implementation of the LISA method.

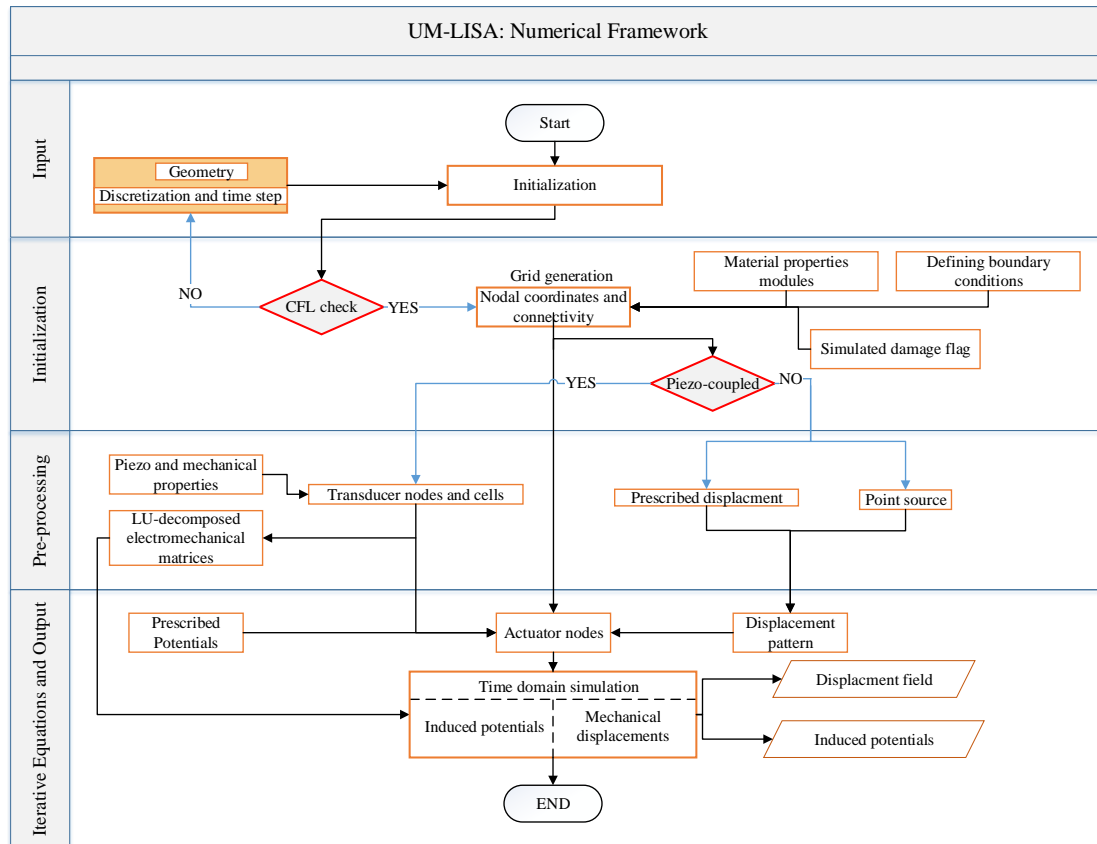


Figure 3.1: Block diagram showing Local Interaction Simulation Approach (LISA) framework.

3.2.1 Model Initialization

Three model setup files (*MaterialDimensions.txt*, *DiscretizationParameters.txt*, *VariableParam.txt*) are used to define the substrate's dimensions, discretizations, and the frequency of the generated GW. The first file sequentially lists the different layers in the

composite laminate including dimensions, Δx_3 for each lamina and associated material properties. The second file determines in-plane discretizations along with time step and total duration of the simulation. Table. 3.1 shows specific details pertaining to the input files.

Table 3.1: Input file parameters.

<i>MaterialDimensions.txt</i>	List of layers with dimensions
	Material-ID
	In-plane rotation
	Through-thickness discretization
<i>DiscretizationParameters.txt</i>	Number of air-cells in the X_1X_2 -plane
	Total duration of simulation and time step
	In-plane discretizations (Δx_1 and Δx_2)
<i>VariableParam.txt</i>	Frequency of excitation

Next, module *MaterialProperties.f90* loads the material properties of the individual layers of the laminated composite from the database (*MaterialDatabase.txt*). Based on the discretizations and the material properties, the subroutine *CFLcheck* performs the stability check using Courant-Friedrichs-Lewy number (CFL) criterion. After the discretization parameters satisfy the stability criterion, the module *NodesMeshGeneration.f90* generates the nodes for the composite substrate along with the connectivity determining the 18 closest neighbors. Next, the 8 cells surrounding a generic node are also assigned material properties based on the material-IDs defined in *MaterialDimensions.txt*. In the numerical simulation, the boundary surfaces are padded with air-cells to represent a free boundary conditions. It should be noted that air layer thickness along the through-thickness direction (X_3 -axis) is defined in the input file, *MaterialDimensions.txt*, and the number of in-plane (X_1X_2 -plane) air-cells are specified in the file *DiscretizationParameters.txt*.

3.2.2 Pre-processing

This section of the UM-LISA determines several key modules for the framework which determine the actuators, sensors and output files.

3.2.2.1 Actuator and Sensor Modeling

There are several ways to generate GW in the UM-LISA framework. The GW generation method can be selected based on the flags specified in file *ActuationFlags.txt*. The list of the available actuation methods along with available shapes are presented in Table. 3.2. In the current version of the UM-LISA, two actuators can be modeled, one on the top and the other on the bottom surface of the laminated plate with both in-phase and out-of-phase excitation to generate waves with a purely symmetric or anti-symmetric fundamental mode in the laminate.

Table 3.2: Actuation method flags in *ActuationFlags.txt*.

Actuation_shape_flag	1 → Circular
	2 → Rectangular
	3 → CLoVER sector
Actuation_type_flag	1 → w_3 point source
	2 → w_2 point source
	3 → PD method-I
	4 → PD method-II
	5 → PC method
Actuation_mode_flag	1 → Single actuator on the top surface of laminate
	2 → Dual actuators, in-phase excitation
	3 → Dual actuators, out-of-phase excitation

The file *ActuatorDimensions.txt* specifies the dimensions (Table. 3.3) of the different actuator shapes specified in *ActuationFlags.txt*. It should be noted that, although multiple dimensions (radius, thickness, length and breadth) can be specified for the actuator, the framework selectively chooses the dimensions used based on the actuator flags in file *ActuationFlags.txt*.

Table 3.3: Actuation dimensions in *ActuatorDimensions.txt*.

Top surface actuator	Outer radius $\rightarrow R_o$ (circular actuator)
	Inner radius $\rightarrow R_i$ (circular actuator)
	Length \rightarrow Dimension along X_1 axis (rectangular actuator)
	Breadth \rightarrow Dimension along X_2 axis (rectangular actuator)
	Thickness \rightarrow Dimension along X_3 axis (PC actuation)
Bottom surface actuator	Outer radius $\rightarrow R_o$ (circular actuator)
	Inner radius $\rightarrow R_i$ (circular actuator)
	Length \rightarrow Dimension along X_1 axis (rectangular actuator)
	Breadth \rightarrow Dimension along X_2 axis (rectangular actuator)
	Thickness \rightarrow Dimension along X_3 axis (PC actuation)

After the actuation method and the dimensions are determined, module *ActuationMethods.f90* returns the set of actuator nodes and the field variables associated with the nodes (displacement components in the case of PD methods and electric potentials in the case of PC method) based on the input excitation. It should be noted that in the case of PC method the module also changes the material properties of the cells constituting the actuator. The list of mechanical and piezoelectric material properties for the transducers in the framework are listed in files *PZT_Mechanical_properties.txt* and *PZT_Dielectric_properties.txt*, respectively. To facilitate the calculation of induced potentials (Eq. 2.32), if present, module *LU.f90* is used to decompose the matrix F in Eq. 2.33 with the aim of using back-substitution during the iterative process. It is also important to note that the module *ActuationMethods.f90* is called during the iterative process for the generation of GW. During the pre-processing step, several text and binary files are generated to record the displacement components and potentials computed in the next step. The list of output files are listed in Table 3.4.

3.2.2.2 Damage Modeling

The UM-LISA framework has the option of adding linear damage to the model just before the iterative equations. The damage can be introduced by overwriting the material

Table 3.4: Output files generated.

<i>parameters_used.txt</i>	List of discretization parameters used in the UM-LISA
<i>Piezo_Act_disp_P.bin</i>	Induced potentials for the piezoelectric actuator
<i>Piezo_Act_disp_U.bin</i>	X_1 displacement component for the piezoelectric actuator
<i>Piezo_Act_disp_V.bin</i>	X_2 displacement component for the piezoelectric actuator
<i>Piezo_Act_disp_W.bin</i>	X_3 displacement component for the piezoelectric actuator
<i>Piezo_Sens_I_disp_P.bin</i>	Induced potentials for the piezoelectric sensor
<i>Piezo_Sens_I_disp_U.bin</i>	X_1 displacement component for the piezoelectric sensor
<i>Piezo_Sens_I_disp_V.bin</i>	X_2 displacement component for the piezoelectric sensor
<i>Piezo_Sens_I_disp_W.bin</i>	X_3 displacement component for the piezoelectric sensor
<i>Xdisp_XYplane.bin</i>	X_1 displacement component at every nodal point on the X_1X_2 -plane, which passes through the actuator nodes
<i>Ydisp_XYplane.bin</i>	X_2 displacement component at every nodal point on the X_1X_2 -plane, which passes through the actuator nodes
<i>Zdisp_XYplane.bin</i>	X_3 displacement component at every nodal point on the X_1X_2 -plane, which passes through the actuator nodes
<i>Xdisp_YZplane.bin</i>	X_1 displacement component at every nodal point on the X_2X_3 -plane, which passes through the actuator nodes
<i>Ydisp_YZplane.bin</i>	X_2 displacement component at every nodal point on the X_2X_3 -plane, which passes through the actuator nodes
<i>Zdisp_YZplane.bin</i>	X_3 displacement component at every nodal point on the X_2X_3 -plane, which passes through the actuator nodes
<i>Xdisp_ZXplane.bin</i>	X_1 displacement component at every nodal point on the X_1X_3 -plane, which passes through the actuator nodes
<i>Ydisp_ZXplane.bin</i>	X_2 displacement component at every nodal point on the X_1X_3 -plane, which passes through the actuator nodes
<i>Zdisp_ZXplane.bin</i>	X_3 displacement component at every nodal point on the X_1X_3 -plane, which passes through the actuator nodes

properties of the cells to reflect voids through holes and notches in the structure. This is beneficial in parametric studies where the effects of simulated damage dimensions can be addressed without creating new models. The framework also allows for the modification of the geometry, which requires that appropriate alterations be made to the connectivity matrix along with assigning the new material properties to the inclusions. The simulated damage (concentrated mass) parameters are loaded from the file *Damage.txt*. Table 3.5 specifies the details in the file.

Table 3.5: Simulated damage parameters in *Damage.txt*.

Damage_flag	0 → No damage
	1 → Simulated damage: concentrated mass
Concentrated mass	Distance from the actuator
	Side length of the cross-section
	Height of the mass
	Azimuthal location of the mass

3.2.3 Iterative Equations

This section of the framework implements the Eqs. 2.29-2.32 to simulate the GW propagation in the structure. The initialized field variables at timesteps $t = -1$ and $t = 0$ are provided to the iterative equations to calculate the field variables at timestep $t = 1$. The time marching method for calculating the displacement field and the implicit method to calculate induced potentials is illustrated in Fig. 3.2.

In Fig. 3.2 the variable “ t ” represents the iterative step of the simulation, w_i ($i = 1, 2, 3$) represents the mechanical displacement field and ψ is the electric potential. Subscripts “Act_top” and “Act_bot” represent the nodes on the top and bottom surfaces of the piezo-electric actuator, respectively, and “prescribed” represents all the nodes where the potentials are enforced by external sources. The main inputs and outputs for the iterative equations section are presented in Table. 3.6.

Table 3.6: Inputs and Outputs of the iterative equations.

Input	Initialized variables (displacements or potentials)
	Material properties of cells surrounding each node
	Discretization parameters
	Input excitation through actuator nodes
	LU decomposed matrices for F (Eq. 2.33)
Output	Mechanical displacements
	Induced potentials

During the implementation of the iterative equations, OPENMP-based parallelization

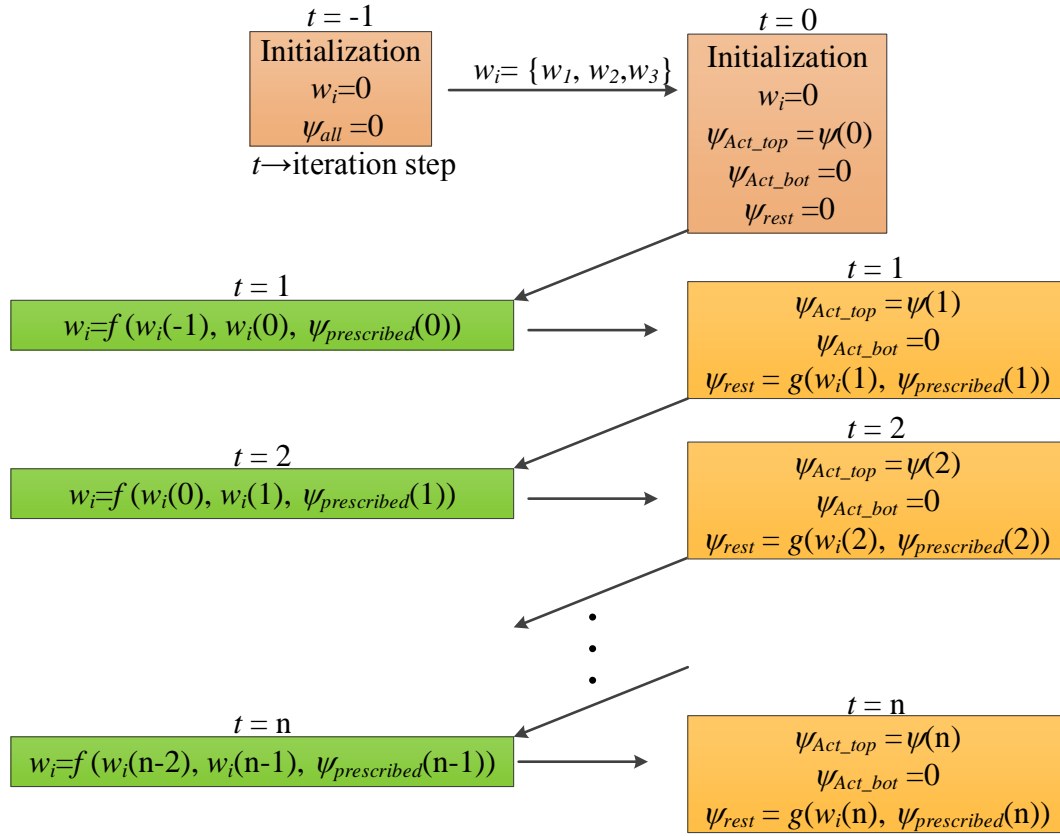


Figure 3.2: Flowchart showing the time-marching scheme utilized in the LISA simulations.

was used to improve the performance of the numerical framework. The parallelization was used to divide the physical domain between 12 processors to achieve increase performance of the UM-LISA code.

3.2.4 Post-processing

This part of the solution is implemented in MATLAB as stand-alone scripts, which analyze the displacement field and induced potential data from the time domain simulations. The data obtained from the time-marching solver can be used to animate the wave propagation, perform frequency analysis, calculate the behavior of actuator nodes and to estimate the induced potentials in a piezo sensor. This is a crucial step in validating the UM-LISA

framework when comparing experiments or analytical methods and performing numerical studies.

CHAPTER 4

Grid Convergence Studies

This chapter presents basic convergence studies for the UM-LISA framework. First, ac-sGW are simulated in isotropic plates with varying spatial and temporal discretizations to determine the parameters affecting wave propagation. Then, the rate of convergence is calculated using a normalized root mean square deviation (NRMSD) metric. Next, simulations with cubic and distorted (cuboidal) grids are conducted to characterize the evolution of error based on relative root mean square deviation (RRMSD). Simulations are also carried out for surface mounted actuators to determine the minimum discretization required for the actuator. Finally, suggestions regarding the optimal parameters while utilizing UM-LISA for wave propagation are presented.

4.1 Effects of Spatial and Temporal Discretizations

Convergence is a critical criterion when developing a numerical method. In the present context, convergence studies are conducted for UM-LISA to ensure its applicability for wave propagation modeling. The simulations are carried out in an isotropic plate model. Extended accuracy and convergence studies were presented by Sundararaman and Adams [124], but the studies were predominantly limited to two-dimensional cases (and PD method-II excitation). This section presents a study focussed on three-dimensional LISA to determine the discretization parameters affecting GW propagation.

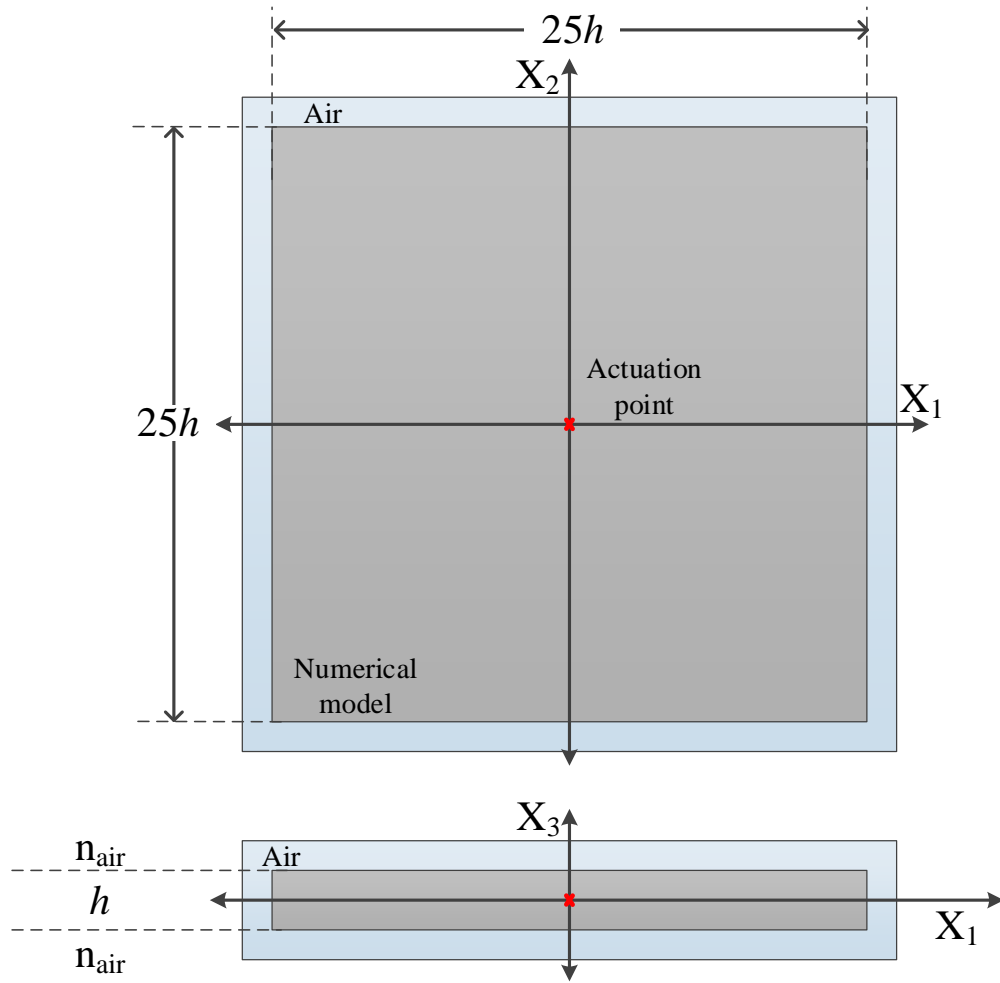


Figure 4.1: Schematic of the simulation model used for point-source convergence study.

Simulations to determine the effect of discretization parameters for UM-LISA were carried out with point-source excitation. The point-source excitation prescribes a predetermined out-of-plane excitation at a specific point in the plate structure. This excitation method was considered to avoid actuator discretization effects on the GW generation.

Figure 4.1 shows the numerical plate model with dimensions of $25h \times 25h \times h$, where h is the thickness of the plate. A fixed number of air cells ($n_{\text{air}} = 4$) were used as padding to represent free edges in the numerical model. The total duration of the simulations was

fixed to $50 \mu s$. The input excitation was prescribed at the center of the plate as shown in Fig. 4.1 with a red cross. The excitation was a 3.5-cycle Hann-modulated toneburst of unit amplitude. A center frequency of 150 kHz was chosen for the rate of convergence studies.

The test cases shown in Table. 4.1 were considered for the isotropic plate case. The isotropic plate has a Young’s modulus of 70 GPa, Poisson’s ratio of 0.3, and density of 2700 kg/m^3 .

Table 4.1: Discretization parameters for convergence studies in an isotropic plate.

Case	Δ_{xyz}	Cells through thickness	Δt (ns)	CFL
Case (a1)	$\frac{h}{4}$	4	2.5	0.013
Case (b1)	$\frac{h}{8}$	8	2.5	0.026
Case (c1)	$\frac{h}{16}$	16	2.5	0.051
Case (d1)	$\frac{h}{32}$	32	2.5	0.102
Case (a2)	$\frac{h}{4}$	4	5	0.026
Case (b2)	$\frac{h}{8}$	8	5	0.051
Case (c2)	$\frac{h}{16}$	16	5	0.102
Case (d2)	$\frac{h}{32}$	32	5	0.205
Case (a3)	$\frac{h}{4}$	4	10	0.051
Case (b3)	$\frac{h}{8}$	8	10	0.102
Case (c3)	$\frac{h}{16}$	16	10	0.205
Case (d3)	$\frac{h}{32}$	32	10	0.409
Case (a4)	$\frac{h}{4}$	4	20	0.102
Case (b4)	$\frac{h}{8}$	8	20	0.205
Case (c4)	$\frac{h}{16}$	16	20	0.409
Case (d4)	$\frac{h}{32}$	32	20	0.819

In Table. 4.1, the cases are classified based on the spatial and temporal discretizations, with letters “a”, “b”, “c”, and “d” representing spatial discretizations of $\frac{h}{4}$, $\frac{h}{8}$, $\frac{h}{16}$ and $\frac{h}{32}$, respectively. Numbers “1”, “2”, “3” and “4” represent temporal discretizations (Δt) of 2.5 ns, 5 ns, 10 ns and 20 ns, respectively. Uniform cell discretization is represented by Δ_{xyz} , i.e., $\Delta x_1 = \Delta x_2 = \Delta x_3 = \Delta_{xyz}$. The test cases provided in Table. 4.1 are not an exhaustive list, but they provide insight into the convergence of the LISA method for wave propagation studies.

Figure 4.2 shows the comparison results for varying spatial discretizations with a constant temporal discretization. The normalized out-of-plane displacement component was

compared at distances of $2.5h$, $5h$ and $7.5h$ from the point of excitation. The displacements were normalized with the amplitude at a distance of $1.25h$ to compensate for the variation in energy associated with prescribing displacements instead of traction. One can see that the spatial discretization affects the wave propagation, with the profiles of the propagating wave monotonically converging with finer spatial discretization. The plots also display a difference in the wave propagation speeds for different spatial discretizations, highlighted by the increasing separation of the wave profiles.

Next, comparison results for varying temporal discretizations for a constant spatial discretization are presented in Fig. 4.3. This comparison aids in visualizing the effect of varying temporal discretizations on wave propagation characteristics. From Fig. 4.3, it can be concluded that temporal discretization seems to have no effect on the propagation characteristics. This phenomenon can be attributed to the fact that the sampling frequency for the test matrix cases is higher than the required sampling rate according to the Nyquist–Shannon sampling criterion [130]. This over sampling is a result of the CFL number constraint on the discretization parameters. For a given spatial discretization, varying the temporal discretization changes the CFL number, so, from the Fig. 4.3 it can also be concluded that the value of the CFL number is not critical in determining the accuracy of the numerical simulation, this was also noted by Iordache et al. [131].

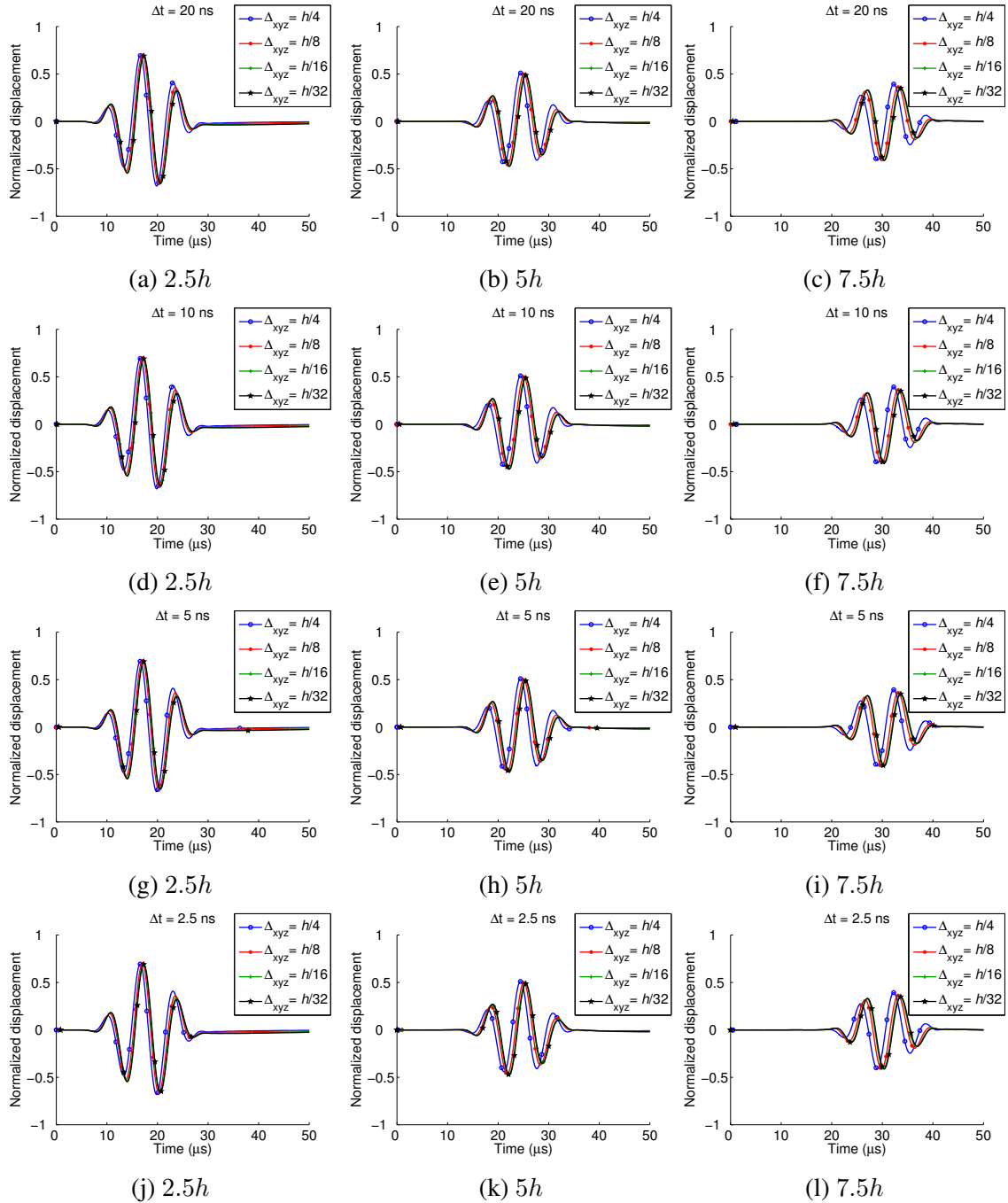


Figure 4.2: Out-of-plane displacement component for different spatial discretizations are compared at different distances from the center of excitation in an isotropic substrate. Each column corresponds to a specific distance from the center of the actuator, and each row corresponds to a particular timestep used for the numerical simulation.

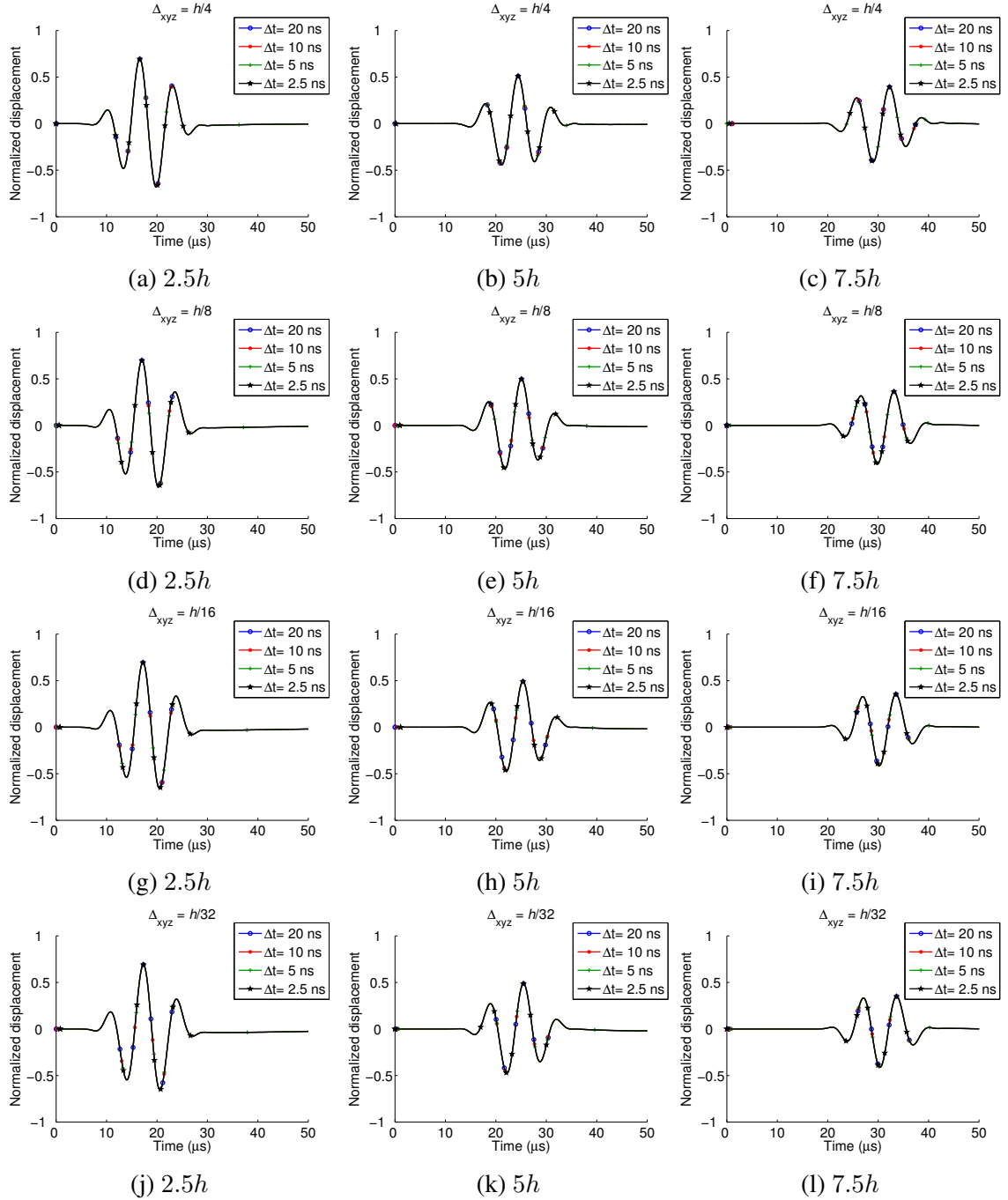


Figure 4.3: Out-of-plane displacement component for different temporal discretizations are compared at different distances from the center of excitation in an isotropic substrate. Each column corresponds to a specific distance from the center of the actuator, and each row corresponds to a particular spatial discretization used for the numerical simulation.

4.2 Rate of Convergence

The test cases shown in Table 4.2 were considered to determine the rate of convergence for the 3D LISA method. It should be noted that the time step was kept constant at 10 ns, which was determined to provide temporal discretization for this case. The same isotropic plate with point source excitation, as shown in Fig. 4.1, was considered again for this study.

Table 4.2: Discretization parameters for determining rate of convergence in an isotropic plate.

Case	Δ_{xyz}	Cells through thickness	Δt (ns)	CFL
Case (I)	$\frac{h}{2}$	2	10	0.026
Case (II)	$\frac{h}{4}$	4	10	0.051
Case (III)	$\frac{h}{8}$	8	10	0.102
Case (IV)	$\frac{h}{16}$	16	10	0.204
Case (V)	$\frac{h}{32}$	32	10	0.409
Case (VI)	$\frac{h}{64}$	64	10	0.818

The out-of-plane displacement pattern in the X_1X_2 plane passing through the input excitation point was used to calculate the rate of convergence. Figure.4.4 shows the snapshots of the normalized displacement field at a time step of 20 μs for different cases of spatial discretization. The spatial dimensions of the plate are normalized by the thickness (h) of the plate. It is evident from the figures that although there is a significant difference between the coarsest grid (Case (I)) and finest grid (Case (VI)), the displacement pattern converges with discretization refinement.

NRMSD was used as a metric to calculate the error for different cases with Case (VI) being considered as the reference. Both spatial and temporal variation of the GW field were considered in calculating the NRMSD as shown in Eq. 4.1.

$$\text{NRMSD(p)} = \frac{1}{n_t} \sum_t \sqrt{\frac{\sum_{x_1x_2} (w_p(x_1, x_2, t) - w_n(x_1, x_2, t))^2}{n_{x_1} n_{x_2} w_n^m(t)}}} \times 100 \quad (4.1)$$

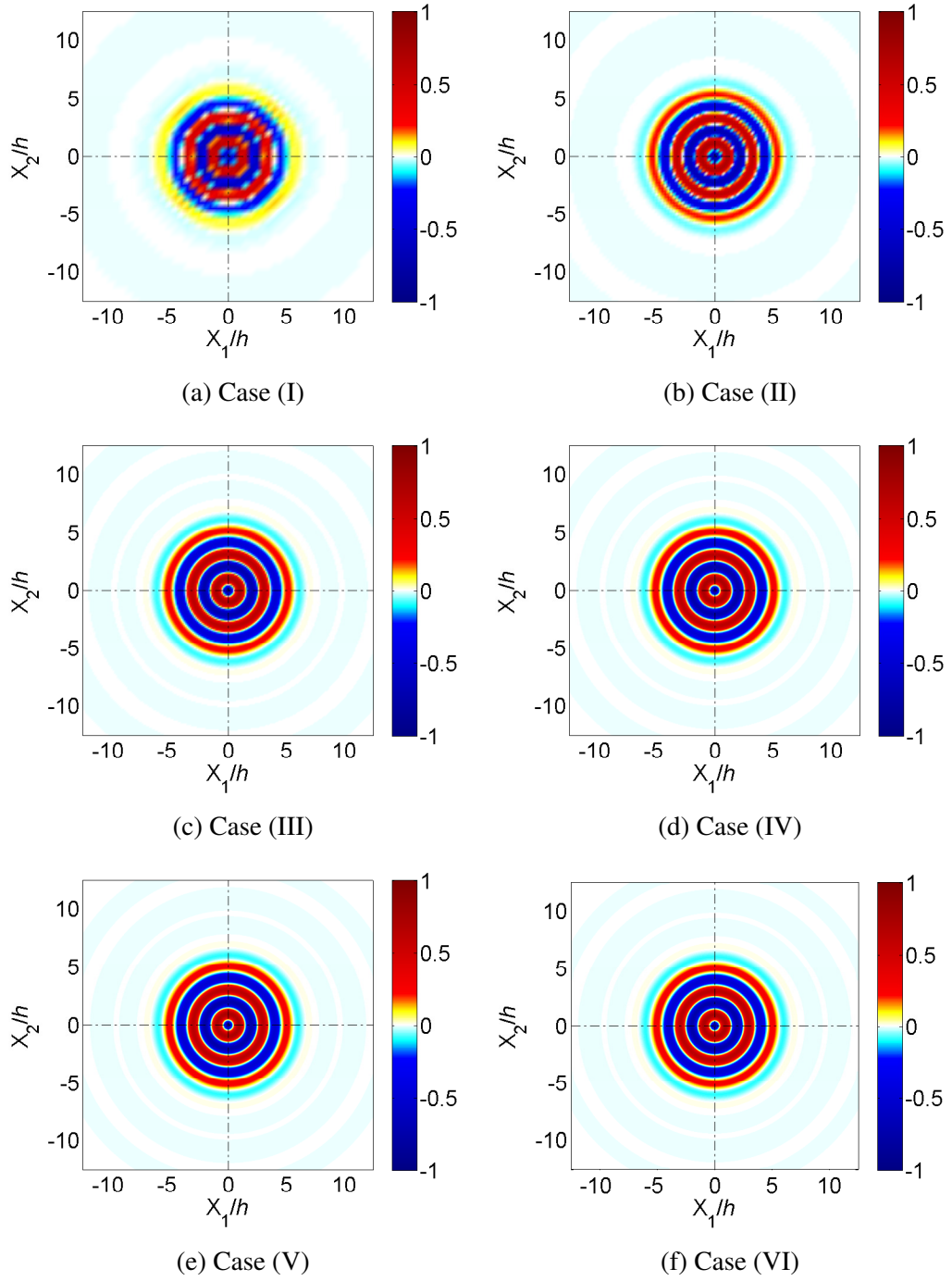


Figure 4.4: Snapshots of the out-of-plane displacement component at $20 \mu s$ for different discretizations. The displacements have been normalized by the amplitude at the point $1.25h$ from the center of the excitation point along the X_1 direction.

where w_p is the displacement field for a given case as listed in Table 4.1, w_n is the reference displacement field (Case (VI)), w_n^m is the maximum value of the reference displacement field at a particular time “ t ”, x_1 and x_2 are coordinated of a generic point in the X_1X_2 plane, $\sum_{x_1x_2}$ represents the summation in spatial domain, \sum_t represents the summation in temporal domain, n_{x_1} and n_{x_2} are the number of spatial points along the X_1 and X_2 axes, respectively, and n_t is the number of temporal samples used in calculating NRMSD.

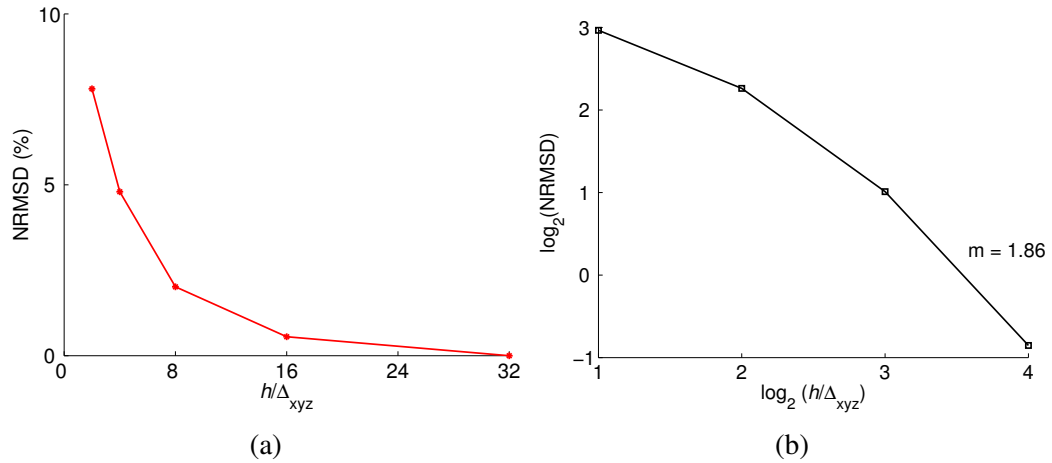


Figure 4.5: (a) Error associated with spatial discretization. The reference case for calculating error is $\Delta xyz = \frac{h}{64}$. (b) Log-log plot of the error, the slope of the connecting line “ m ” determines the rate of convergence.

Figure 4.5(a) shows the NRMSD as a function of spatial discretization and Fig. 4.5(b) shows the log-log plot of the error. From the former, one can see the gradual decrease in the error with increasing discretization. The log-log plots indicates the convergence rate for the numerical method to be 1.86.

4.3 Convergence Error

Lamb wave characteristics such as propagating speed, dispersion and existence of higher order modes depend on the frequency-thickness parameter. Verification of the LISA methodology for different frequency-thickness cases is essential in developing a robust numerical

framework. In this section, studies to determine the effect of spatial discretization on simulating GW for different frequency-thickness cases are studied.

4.3.1 Point Source Actuation

Point source excitation was considered for the same isotropic plate as used in the previous section, and a time step of 10 ns was used for the simulations. In the study, various frequency-thickness cases were considered, and RRMSD was used as a metric to calculate the error for different cases, i.e.,

$$\text{RRMSD}(p) = \frac{1}{n_t} \sum_t \sqrt{\frac{\sum_{x_1 x_2} (w_p(x_1, x_2, t) - w_{p+1}(x_1, x_2, t))^2}{n_{x_1} n_{x_2} w_{p+1}^m(t)}}} \times 100 \quad (4.2)$$

where w_{p+1} is the displacement field for the next level of discretization for given case w_p listed in Table 4.1, and w_{p+1}^m is the maximum value of the displacement field at a particular time step. The wave packet in each of the frequency-thickness cases was allowed to travel for 25 μs after the generation of the signal. The error metrics NRMSD and RRMSD differ on the choice of reference: NRMSD considers a universal reference or a “true solution” as the reference (the finest discretization in this study), where as the RRMSD captures the evolution of error between successive discretizations.

Figure 4.6(a) shows the RRMSD as a function of varying cell discretizations for different frequency-thickness cases. The cases were chosen in the region of the dispersion curves dominated by the first symmetric (S_0) and anti-symmetric (A_0) modes. Cubic cells were considered for the initial case, i.e. $\Delta x_1 = \Delta x_2 = \Delta x_3 = \Delta_{xyz}$. It can be seen that for each of the frequency-thickness cases, the error monotonically reduced. From the above figure, one can see that coarser discretizations ($\Delta_{xyz} = h/2$ and $\Delta_{xyz} = h/4$) result in larger RRMSD associated with higher frequency-thickness cases than frequency-thickness cases. From the figure it can be also observed that the RRMSD converges for a discretization of

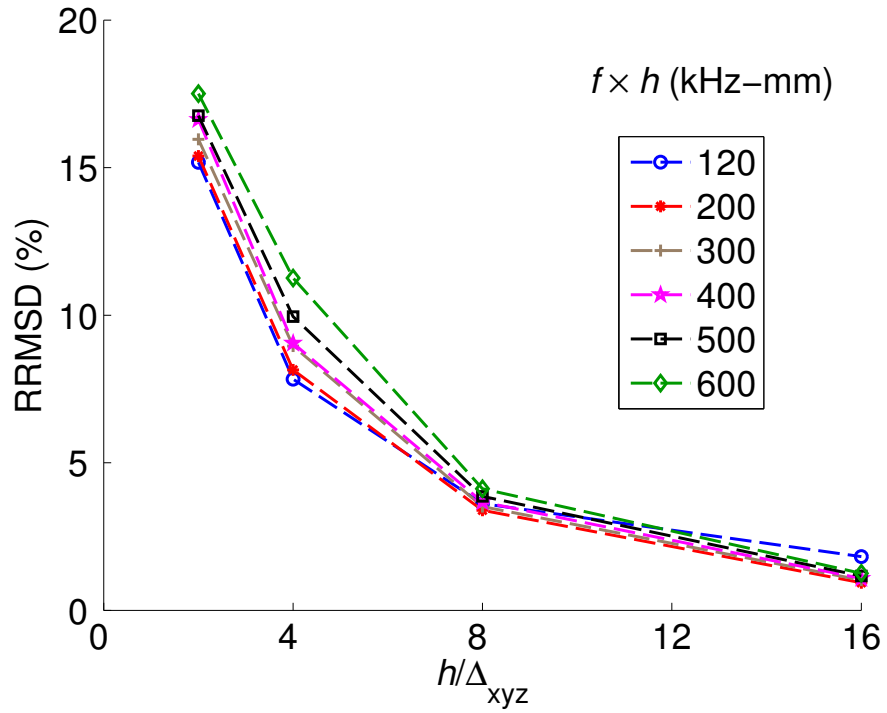
($\Delta_{xyz} = h/8$), after which there is a trend reversal in the RRMSD value observed for lower frequencies as compared to higher frequencies. From the figure it can be concluded that the rate of RRMSD change is high for higher frequencies than lower frequencies, and also that for a discretization of $\Delta_{xyz} = \frac{h}{8}$, all the frequency-thickness cases indicate an error less than 5% based on the RRMSD metric.

Using cuboid cells are more desirable for simulating GW in thin-walled structures because of the high aspect ratio of the substrate. Figure 4.6(b) shows the RRMSD for cuboid cells where the through-thickness discretization (Δx_3) was fixed at $\frac{h}{20}$, and the in-plane discretizations (Δx_1 and Δx_2) were varied for different frequency-thickness cases. There is a lower error in the case of cuboid case for coarser in-plane discretization as the through-thickness discretization is already refined to $\frac{h}{20}$, highlighting the importance of through-thickness discretization. Figure 4.7 illustrates the difference between the cubic and cuboid cells for different frequency-thickness cases. The Δx_3 is the only parameter varying between the cubic and cuboid discretizations, and from the plots it can be seen that having coarser Δx_3 has a significant effect on the RRMSD. Consequently LISA simulations can be carried out with coarser in-plane discretizations (Δx_1 and Δx_2) with a less penalty for appropriate choice of Δx_3 .

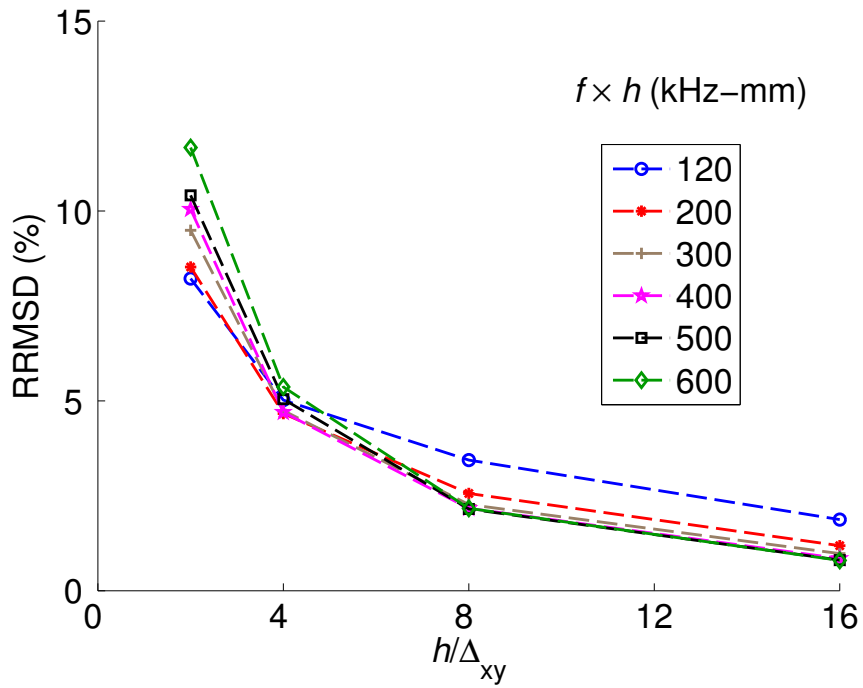
4.3.2 Piezo Actuation

Simulations were also performed for the piezo-coupled version of the UM-LISA framework with varying substrate and actuator discretizations. The numerical plate model used in the study had dimensions of $25h \times 25h \times h$, where h is the thickness of the plate. The dimensions of the piezo actuator were $4h \times 4h \times \frac{h}{8}$. The input excitation was a 10 V potential difference between the surfaces of the piezo actuator in the form of a 3.5-cycle Hann-modulated toneburst at a center frequency of 75 kHz. The total duration of the simulations was 72 μs . The actuator was placed in the center of the plate as shown in Fig. 4.8.

Cuboid cells are considered in the discretization of the actuator and substrate. Table. 4.3



(a) $\Delta x_1 = \Delta x_2 = \Delta x_3 = \Delta_{xyz}$



(b) $\Delta x_1 = \Delta x_2 = \Delta_{xy}$ and $\Delta x_3 = \frac{h}{20}$

Figure 4.6: Comparison of RRMSD error estimates for (a) cube and (b) cuboidal cells for different frequency-thickness cases.

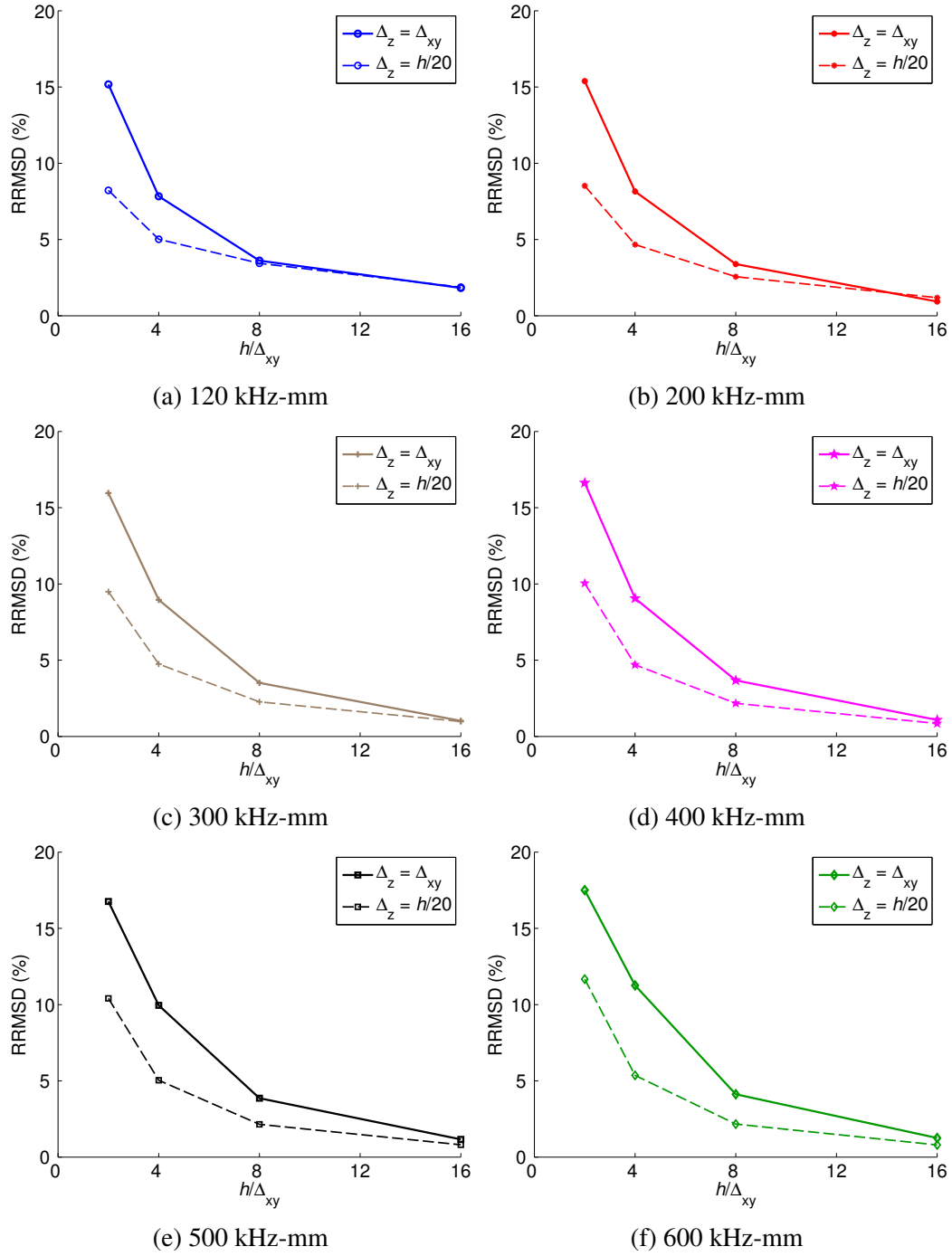


Figure 4.7: Comparison of error estimates between cubic and cuboidal discretization.

lists the numerical cases for the spatial discretizations of the actuator and substrate. Letters “a”, “b”, “c”, and “d” represent substrate’s through-thickness discretizations and numbers “1”, “2”, “3” and “4” represent actuator’s through-thickness discretizations of $\frac{h}{8}$, $\frac{h}{16}$, $\frac{h}{32}$ and

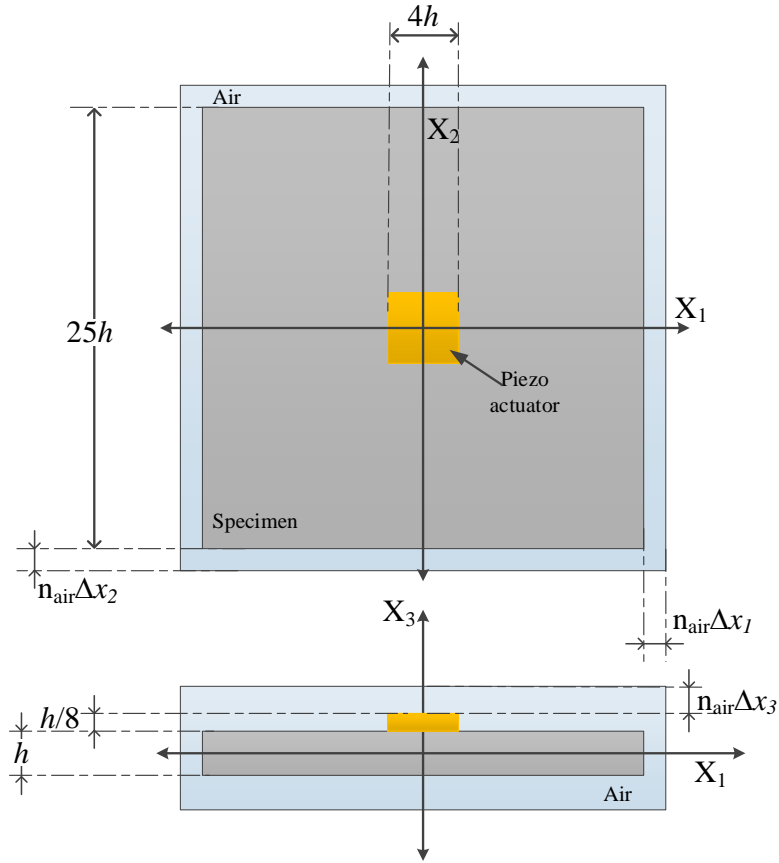


Figure 4.8: Schematic of the simulation model used for piezo actuator convergence study.

$\frac{h}{64}$, respectively. In the study, the in-plane discretization for Δx_1 and Δx_2 was fixed at $\frac{h}{8}$.

Two specimens were considered in the study: an isotropic plate and a uni-directional laminate. The isotropic plate is made of Aluminum, where carbon fiber IM7/977-3 properties were used for the uni-directional laminate as listed in Table 5.1. The NRMSD metric was considered for error evaluation and the finest discretization case (Case 4d) was considered as the reference.

Figures 4.9 and 4.10 show the NRMSD error for the isotropic and composite plates, respectively. The NRMSD was calculated based on the displacement profile measured along a square contour on the top surface of the substrate at a distance of h from the edge of the

Table 4.3: Discretization parameters for piezo actuator convergence studies.

Case	Δ_{x_3} (Actuator)	Δ_{x_3} (Substrate)	CFL (Actuator)	CFL (Substrate)
Case (1a)	$\frac{h}{8}$	$\frac{h}{8}$	0.068	0.102
Case (1b)	$\frac{h}{8}$	$\frac{h}{16}$	0.068	0.205
Case (1c)	$\frac{h}{8}$	$\frac{h}{32}$	0.068	0.409
Case (1d)	$\frac{h}{8}$	$\frac{h}{64}$	0.068	0.819
Case (2a)	$\frac{h}{16}$	$\frac{h}{8}$	0.137	0.102
Case (2b)	$\frac{h}{16}$	$\frac{h}{16}$	0.137	0.205
Case (2c)	$\frac{h}{16}$	$\frac{h}{32}$	0.137	0.409
Case (2d)	$\frac{h}{16}$	$\frac{h}{64}$	0.137	0.819
Case (3a)	$\frac{h}{32}$	$\frac{h}{8}$	0.273	0.102
Case (3b)	$\frac{h}{32}$	$\frac{h}{16}$	0.273	0.205
Case (3c)	$\frac{h}{32}$	$\frac{h}{32}$	0.273	0.409
Case (3d)	$\frac{h}{32}$	$\frac{h}{64}$	0.273	0.819
Case (4a)	$\frac{h}{64}$	$\frac{h}{8}$	0.546	0.102
Case (4b)	$\frac{h}{64}$	$\frac{h}{16}$	0.546	0.205
Case (4c)	$\frac{h}{64}$	$\frac{h}{32}$	0.546	0.409
Case (4d)	$\frac{h}{64}$	$\frac{h}{64}$	0.546	0.819

actuator. In the figures, $\Delta_{z(\text{Substrate})}$ represents the substrate discretization, and n_{Actuator} represents the number of cells through the actuator thickness. The NRMSD was calculated for all the mechanical displacement components (w_1 , w_2 , w_3). Overall, monotonic reduction in error was observed for most of the cases (except Fig. 4.9 (c)) with increasing discretization of actuator and substrate. As expected, in the case of the isotropic plate, error profiles are identical for in-plane displacements as seen in Fig. 4.9 (a) and Fig. 4.9 (b). From the figures one can also observe that sufficient discretizations of both the substrate and actuator are essential to obtain accurate results. Based on the NRMSD values for the w_3 displacement (Figs. 4.9 (c) and 4.10 (c)), one can see that there is less NRMSD variation for increasing substrate discretization as compared to increasing the number of cells through the thickness of the actuator, indicating that the actuator discretization has more effect than the substrate discretization. Based on the figures, one can conclude that beyond a discretization of $\frac{h}{16}$ for the substrate there is not much improvement for a given discretization of the actuator. Moreover, $n_{\text{Actuator}} = 4$ for the actuator discretization should be sufficient for most applications.

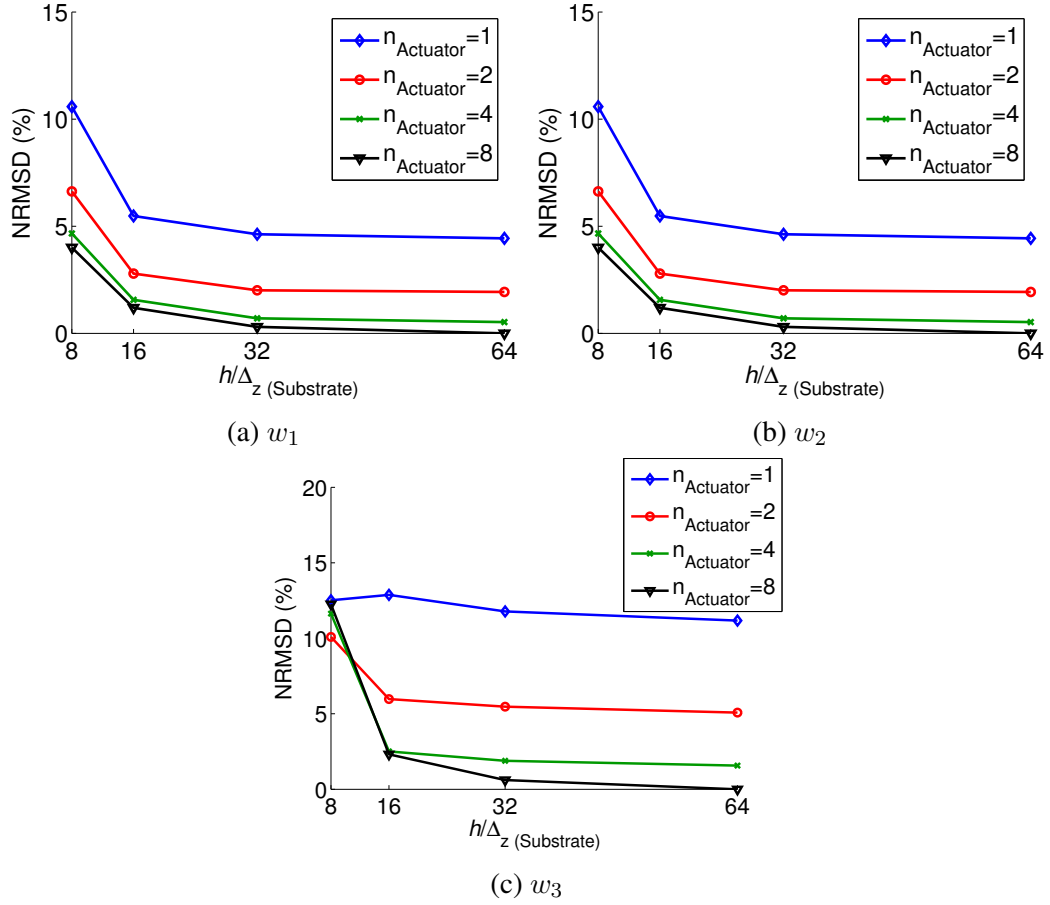


Figure 4.9: NRMSD metric for the isotropic substrate for different discretizations.

4.3.3 Air Layer Error

Solution of UM-LISA usually involves padding the substrate with air cells to represent free boundary conditions. Simulations to investigate the impact of those air cells to the GW solution were carried by changing the number of air cells surrounding a plate structure. The actuator coupled model shown in Fig. 4.8 was considered for this study. The metric presented in Eq. 4.2 was used to quantify the error. A uniform cell discretization of $\frac{h}{16} \times \frac{h}{16} \times \frac{h}{16}$ was considered for the simulation. Two specimens were considered in the study, an isotropic plate and a uni-directional laminate. The isotropic plate is made of Aluminum, and IM7/977-3 properties were used for the uni-directional laminate as listed in Table 5.1.

Figure 4.11 shows the RRMSD for different number of air cells. Although there is a

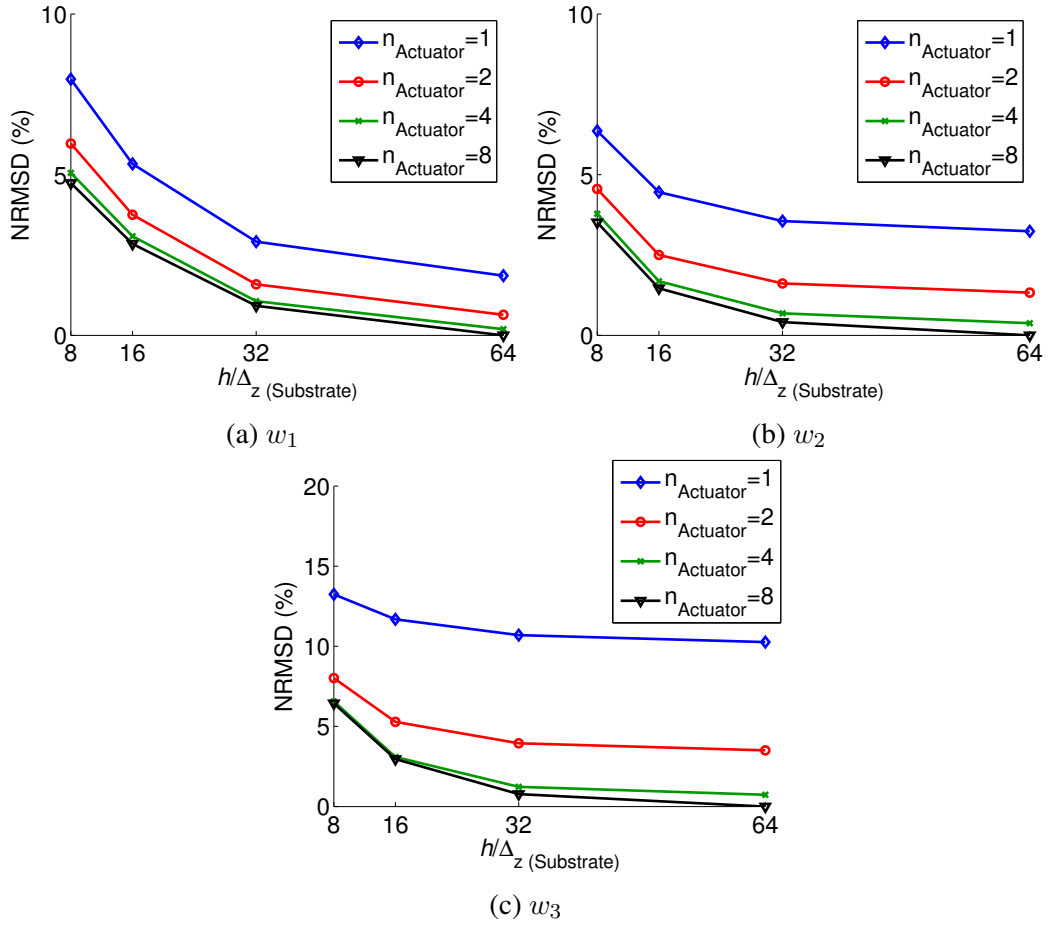


Figure 4.10: NRMSD metric for the uni-directional laminate substrate for different discretizations.

decrease in the error with increasing number of air cells, the value is significantly small compared to the errors associated with cell discretizations. Therefore, $n_{\text{air}} = 4$ is sufficient to obtain low error, and further addition of air cells to represent free boundary conditions would needlessly increase the computational cost with marginal impact on the solution.

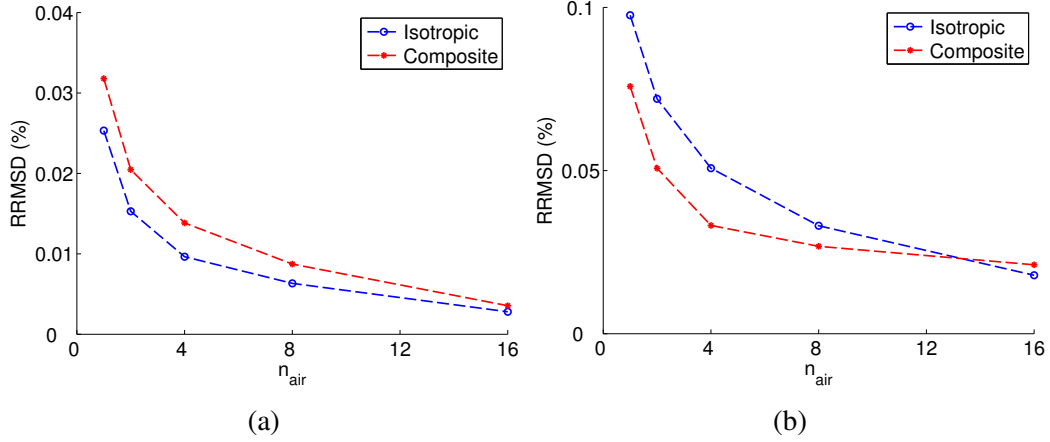


Figure 4.11: Error associated with number of air cells for different plates for (a) a single time step at peak excitation ($23\mu s$) (b) averaged over $72\mu s$.

4.4 Guidelines for Discretization Parameters

Several factors affect the GW simulation using the LISA methodology. Two critical features are numerical stability and grid convergence. Stability condition ensures the boundedness of the solution, whereas the grid convergence results in an accurate simulation.

Table 4.4 provides guidelines for the discretization parameters while implementing the UM-LISA framework for simulating GW. The first step is to ensure the stability of the numerical framework by satisfying the CFL criterion. The next important parameter is the through-thickness discretization (Δx_3); it is advisable to have a discretization of $\frac{h}{8}$ for

Table 4.4: Guidelines for parameter selection in UM-LISA.

Stability	$\text{CFL} \leq 1$
Grid convergence	$\Delta x_1 \leq \frac{h}{4}$
	$\Delta x_2 \leq \frac{h}{4}$
	$\Delta x_3 \leq \frac{h}{8}$
	$\Delta t \leq \frac{1}{2f_{\text{max}}}$
	$N_\lambda \geq 8$ [132]
	$N_\lambda \approx 16$
Actuator convergence	$n_{\text{Actuator}} \geq 4$

Δ_{x_3} . Coarser discretizations can be used for the in-plane discretizations (Δx_1 and Δx_2), and it is suggested to have cell sizes less than $\frac{h}{4}$. If piezo transducers are used in the simulation, then it is advisable to have at least 4 cells through the thickness of the actuator. The number of nodes per wavelength (N_λ), defined as:

$$N_\lambda = \frac{\sqrt{S_{min}/\rho}}{\Delta x_{max} f_{max}} \quad (4.3)$$

where S_{min} is the component of stiffness along the least stiff direction, Δx_{max} is the maximum discretization used in the model, and f_{max} is the maximum frequency component of the excitation signal. Although, Harker [132] noted that having $N_\lambda \geq 8$ was sufficient for accurate ($\leq 1\%$ error) results in finite difference based solutions, based on the simulations carried out in this dissertation, it is advisable to have $N_\lambda \approx 16$. The time step (Δt) tends to be defined by the CFL condition, and the largest one that satisfies it will be enough to provide temporal convergence. Finally, it is also advisable to have at least 4 cells of air (n_{air}) around the structure when modeling free edges. Because of the comparatively low mechanical properties used for modeling air cells, their discretization has little effect on the wave propagation characteristics, and ensuring $CFL \leq 1$ is the only constraint in choosing the discretization parameters for the air cells.

CHAPTER 5

Numerical and Experimental Studies

This chapter presents the results obtained from several numerical studies. After the initial characterization studies of UM-LISA in the previous chapter, its capabilities are exercised to study the wave propagation characteristics in different thin-walled structures. First, the effects of material anisotropy on the characteristics of wave propagation are compared against laser vibrometry experiments. Next, a simulated damage is modeled using the framework and the results are compared with piezo sensor experiments. Then, the effects of substrate's anisotropic material properties and mechanical impedance mismatch between the actuator and substrate on the GW generation are studied. Finally, the UM-LISA formulation is exercised to study the sensor response characteristics and the simulations are compared with experimental results.

5.1 Anisotropic Effects in Composite Laminates

5.1.1 Experimental Test Specimens

Several material systems were used in the numerical studies, and their mechanical material properties are presented in Table 5.1. The composite laminates used in this study were manufactured from pre-impregnated composite tape made from IM7 fibers and Cycom 977-3 resin (Cytac Engineered Materials). The thickness of the carbon fiber prepreg layer is 0.125 mm. The mechanical properties provided by the manufacturer were used as

a starting point, and mechanical tensile tests and wave velocity tests on the unidirectional coupons aided in converging on the material properties used in the numerical simulation.

The multilayered composite specimens used in this study were 12-layer uni-directional $[0]_{12T}$, 12-layer cross-ply $[0/90]_{3S}$, and 16-layer quasi-isotropic $[0/45/-45/90/90/-45/45/0]_S$ laminates. The uni-directional laminate provided the highest amount of anisotropy, whereas the cross-ply and quasi-isotropic laminates provided a typical representation of the configurations used in practical applications. The composite laminates used in this study were manufactured in-house following the fabrication procedure specified in Ref. [133]. The 12-layer laminates had a post-cure thickness of 1.5 mm whereas the 16-layer laminates had a thickness of 2.0 mm. In this study, PZT 5A was used for transduction. Its mechanical material properties are presented in Table 5.1 and the piezoelectric properties are shown in Table 5.2.

Table 5.1: Mechanical properties of different materials used in the simulations.

Mech. Prop.	Aluminum	IM7/977-3	PZT 5A	T300B-3K Fabric - Epon 862	Last-A-Foam FR - 6710
E_{11} (GPa)	70.28	147.00	60.98	50.10	0.09
E_{22} (GPa)	70.28	9.80	60.98	50.10	0.09
E_{33} (GPa)	70.28	9.80	53.19	9.80	0.09
ν_{12}	0.33	0.41	0.35	0.21	0.3
ν_{13}	0.33	0.41	0.44	0.40	0.3
ν_{23}	0.33	0.48	0.44	0.08	0.3
G_{12} (GPa)	26.42	3.70	22.57	19.6	0.02
G_{13} (GPa)	26.42	3.70	21.05	3.50	0.02
G_{23} (GPa)	26.42	3.31	21.05	3.50	0.02
ρ (kg/m ³)	2684	1558	7750	1760	160

5.1.2 Experimental Setup

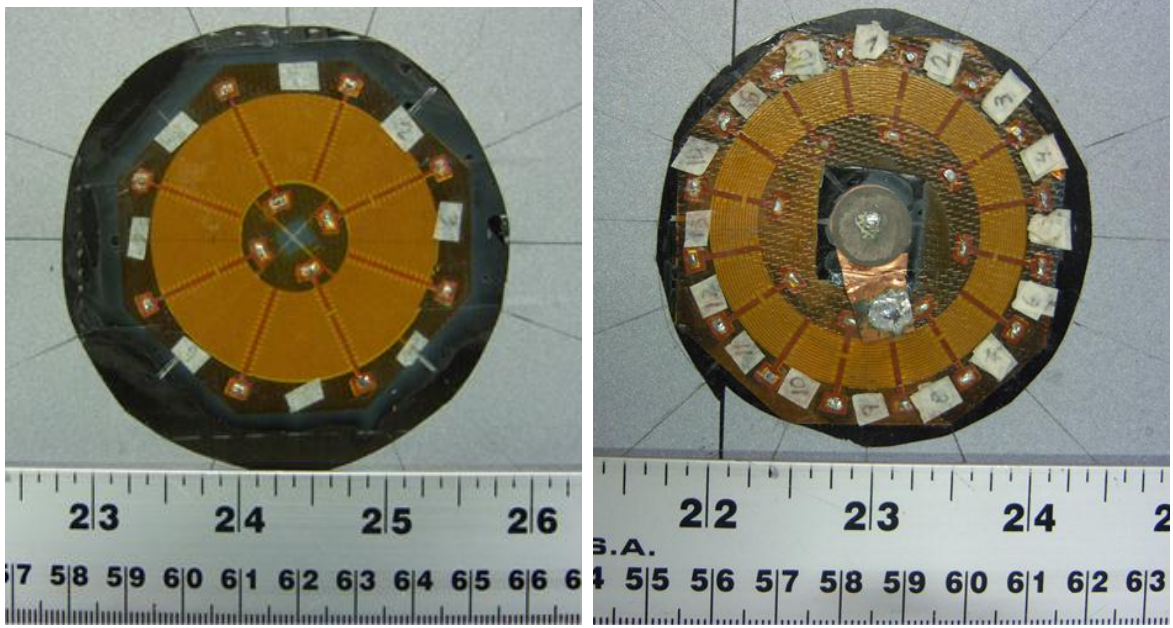
The composite laminates used in the experiments were autoclave fabricated and had a square geometry with 0.5 m in each side. The uni-directional and cross-ply laminates were

Table 5.2: Transducer piezoelectric properties.

Piezo. Prop.	PZT 5A
e_{15} (C/m ²)	12.29
e_{25} (C/m ²)	12.29
e_{31} (C/m ²)	-5.35
e_{32} (C/m ²)	-5.35
e_{33} (C/m ²)	15.78
κ_{11} (nF/m)	8.13
κ_{22} (nF/m)	8.13
κ_{33} (nF/m)	7.32

1.5 mm thick while the quasi-isotropic laminate was 2 mm thick. For the wave propagation studies, a piezoceramic disc (PZT-5A) and two different CLoVERs were used. The PZT disc had a diameter of 12.8 mm ($R_O = 6.4$ mm) and a thickness of 0.23 mm. CLoVER1, shown in Figure 5.1(a), was comprised of eight 45-deg sectors with an inner and outer diameter of 20 mm and 50 mm, respectively. The radial length of the actuator was divided into two segments of lengths 5 mm and 10 mm. CLoVER2, shown in Figure 5.1(b), was comprised of sixteen 22.5-deg sectors with an inner and outer diameter of 35 mm and 50 mm, respectively. The radial length of the actuator was divided into two segments of lengths 2.5 mm and 5 mm. For the current experiments, only the larger segments were used. The CLoVER transducers were bonded with a secondary cure on the top surface of the laminates. A 3.5-cycle Hann-modulated toneburst at a center frequency of 75 kHz was used in the experiments for input excitation, as shown in Fig. 5.2(a) and the frequency content of the input signal was obtained by performing fast fourier transformation (FFT), as shown in Fig. 5.2(b). More details related to the experiments can be found in Ref. [30].

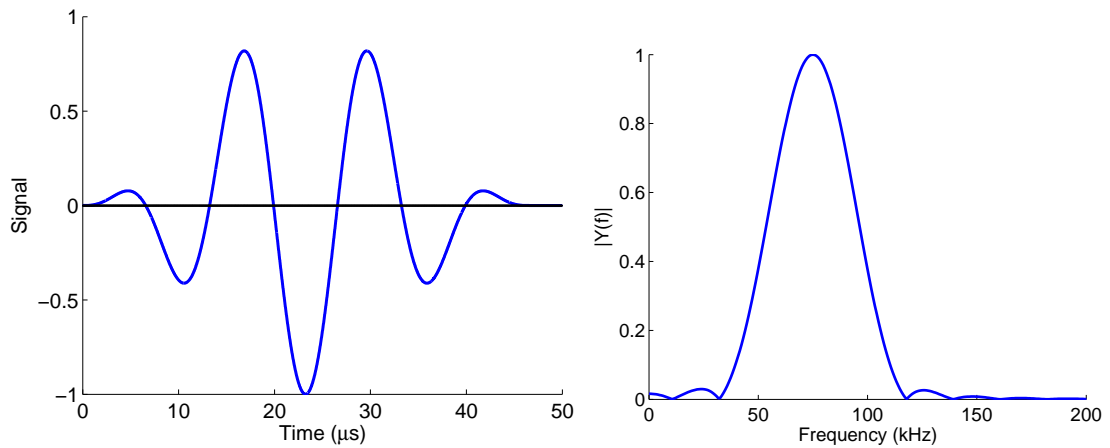
For the GW propagation studies, out-of-plane displacement profile was chosen as the comparison parameter. The GW field was measured using a Polytec PSV-400 scanning laser vibrometer in the configuration shown in Figure 5.3. Retroreflective tape was used on the top surface of the composite laminates to increase laser visibility.



(a) CLoVER1

(b) CLoVER2

Figure 5.1: Two CLoVERs used in the experimental studies.



(a) Signal at 75kHz center frequency.

(b) FFT of the signal.

Figure 5.2: The input excitation chosen for the validation studies.

5.1.3 Simulation Parameters

The structures used in the simulation were multilayered composite laminates with in-plane dimensions of 350×350 mm. The laminates had a through-thickness dimension of 1.5 mm for uni-directional and cross-ply laminates, and 2 mm for the quasi-isotropic lam-

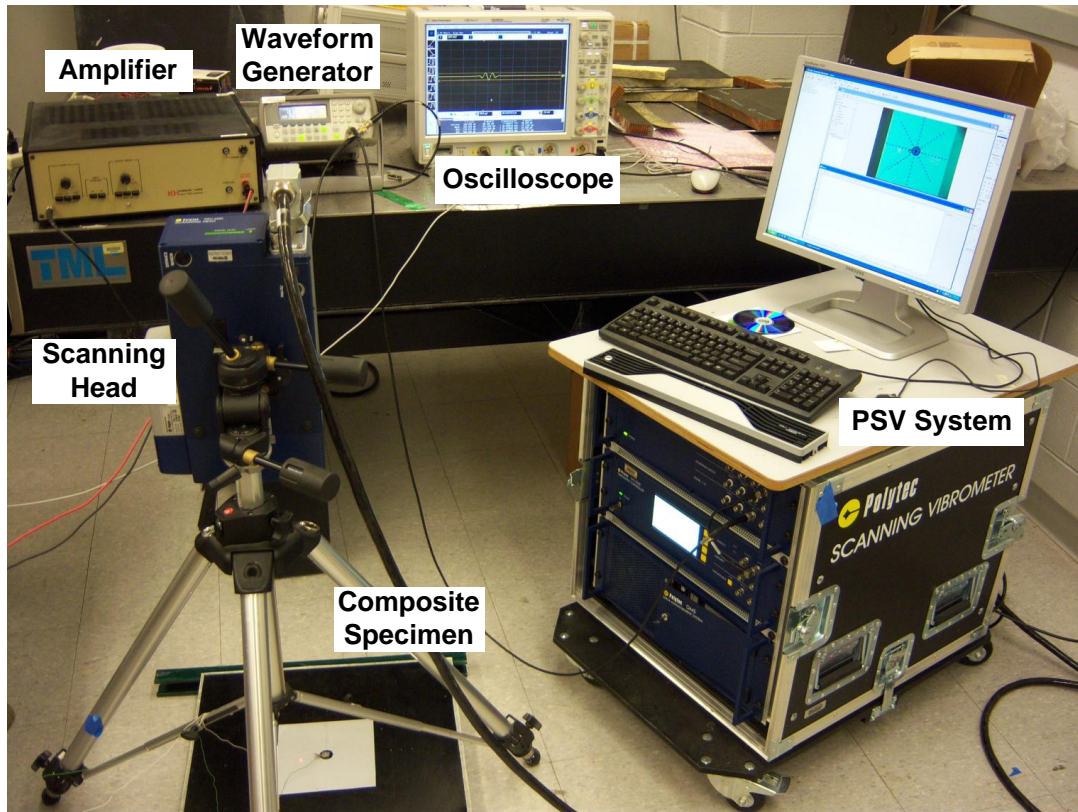


Figure 5.3: Experimental setup showing different components used in the laser vibrometry experiments to measure the guided waves propagation field.

inate. After convergence studies, the structure was discretized using cells of dimension $0.5 \times 0.5 \times 0.125$ mm with $351 \times 351 \times 13$ grid points. Also, a time step of 1×10^{-8} s was used to ensure numerical stability according to the CFL criterion (CFL= 0.842, for the IM7/977-3 material system in Table 5.1 and the chosen discretization parameters). To simulate free boundary conditions, additional cells ($n_{\text{air}} = 4$) with the material properties of air (density of 1.3 kg/m^3 and stiffness 10,000 times less than aluminum) were added to complete the computational domain. The out-of-plane displacement component was monitored in the simulation for the top surface of the composite laminate and compared with experimental results.

5.1.4 Phase Slowness Diagrams

Phase slowness diagrams provide valuable insight into the GW energy propagation direction, which is represented by the vector normal to the curve at any given azimuthal position [47]. The phase slowness diagrams for uni-directional, cross-ply, and quasi-isotropic laminates used in this study are presented in Fig. 5.4. These results were generated using the Global Matrix approach [4], since the discrete nature of the rectangular grid in the LISA solution would require a very fine discretization to obtain equivalent results.

The slowness curve in Fig. 5.4(a) is for the uni-directional laminate with fibers oriented along the 0-deg azimuthal direction. Based on the shape of the curve, most of the energy is directed along the fibers. The slowness curve for the cross-ply laminate displayed in Fig. 5.4(b) shows that most of the energy is concentrated along the 0-deg and 90-deg azimuthal directions, and although the direction of the normal to the slowness curve at 45-deg is along that same direction, it has a higher amount of energy spreading because of the smaller radius of curvature. The slowness curve in the case of the quasi-isotropic laminate (Fig. 5.4(c)) is almost circular owing to even azimuthal distribution of the constituent plies.

5.1.5 Piezoceramic Disk Actuator

The first set of experiments were carried out with the circular PZT actuator to visualize the guided wave propagation in different composite specimens. Certain GW propagating characteristics, such as energy steering and energy attenuation, can be determined in different directions. The out-of-plane propagation patterns for the LISA simulations and experiments for uni-directional, cross-ply, and quasi-isotropic laminates, are compared in Figs. 5.5, 5.6 and 5.7, respectively. Snapshots of the normalized out-of-plane component of the displacement at different time steps were recorded on the top surface of the laminate to compare the propagation pattern of the GW.

In the uni-directional laminate, the fiber direction was parallel to the x-axis. From Fig. 5.5, it is evident that the majority of the wave energy propagated along the fiber direc-

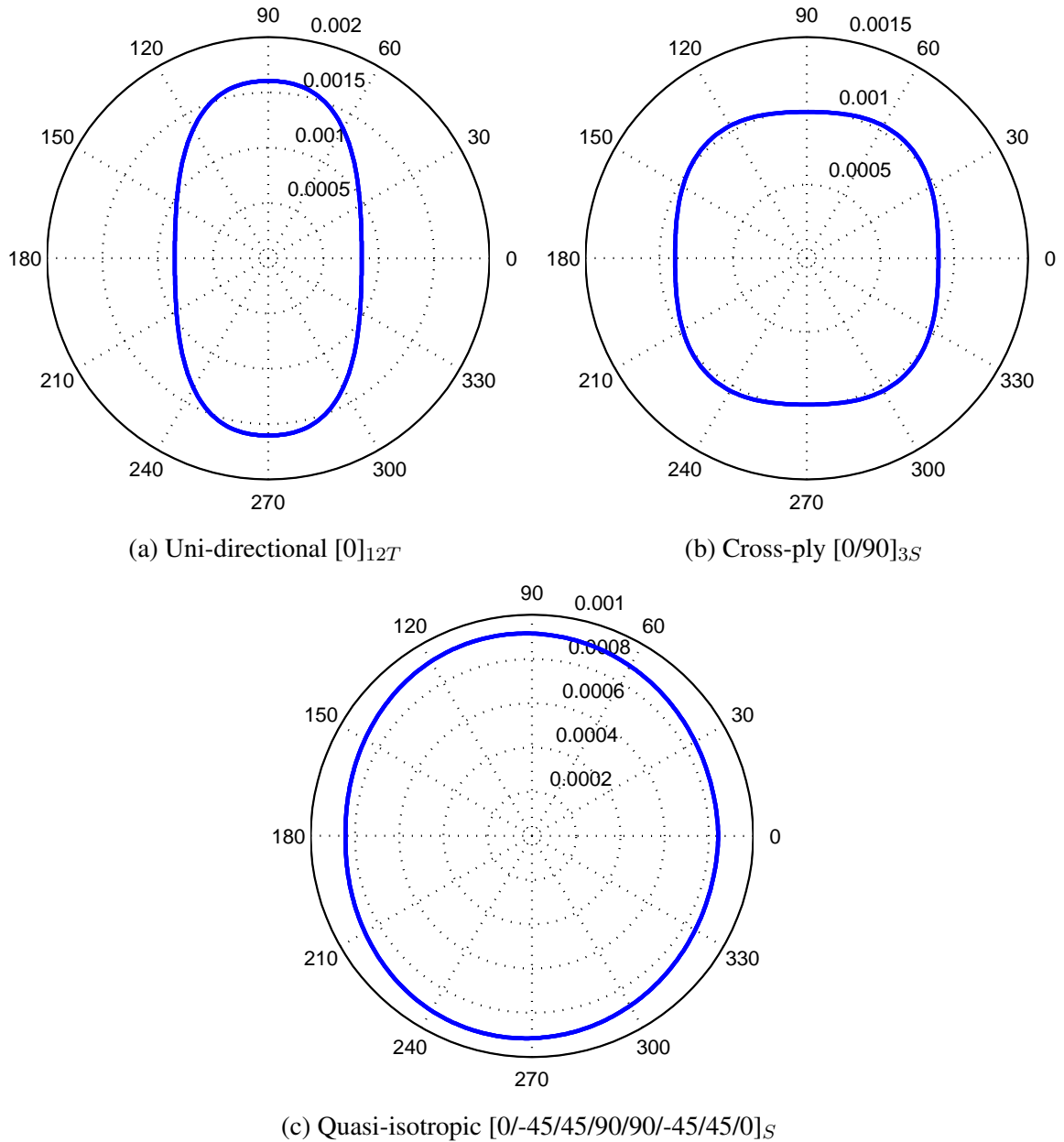


Figure 5.4: IM7/977-3 material phase slowness for the antisymmetric mode at 75 kHz.

tion, and the velocity normal to the fiber direction was slower as compared to the velocity along the fiber direction because of the difference in material properties. These phenomena are also expected based on the slowness plot shown in Fig. 5.4(a). The wave propagation simulated with LISA was in good agreement with the experimental data, as the main propagation characteristics were captured with the simulation. It is worth noticing, however, that

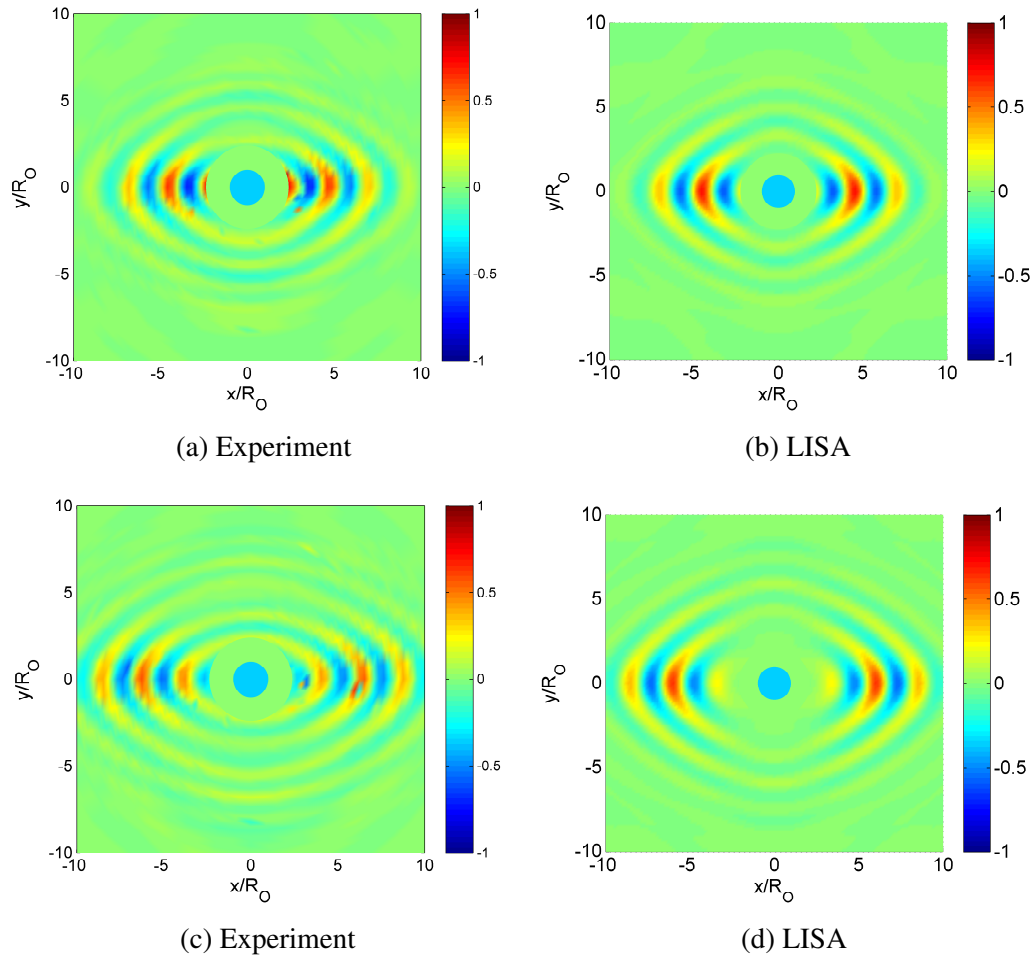


Figure 5.5: Out-of-plane normalized displacements in a uni-directional laminate $[0]_{12T}$ at (a)-(b) $58 \mu s$ and (c)-(d) $68 \mu s$. Distances from the center of the plate normalized by actuator radius ($R_O = 6.4 \text{ mm}$).

the simulation showed a higher wave velocity in the transverse direction than observed in the experiment. This is attributed to the higher uncertainty in the material properties of the resin. While the Young's modulus along the fiber direction was experimentally determined, the shear modulus used in the analysis was provided by the material manufacturer.

Even better correlation was observed for the cross-ply laminate as shown in Fig. 5.6. As expected from the slowness curves, we can see that the majority of the energy was along the 0-deg and 90-deg directions, corresponding to the fiber directions. It was observed both experimentally as well as numerically that the wave traveled slightly faster along the 0-deg

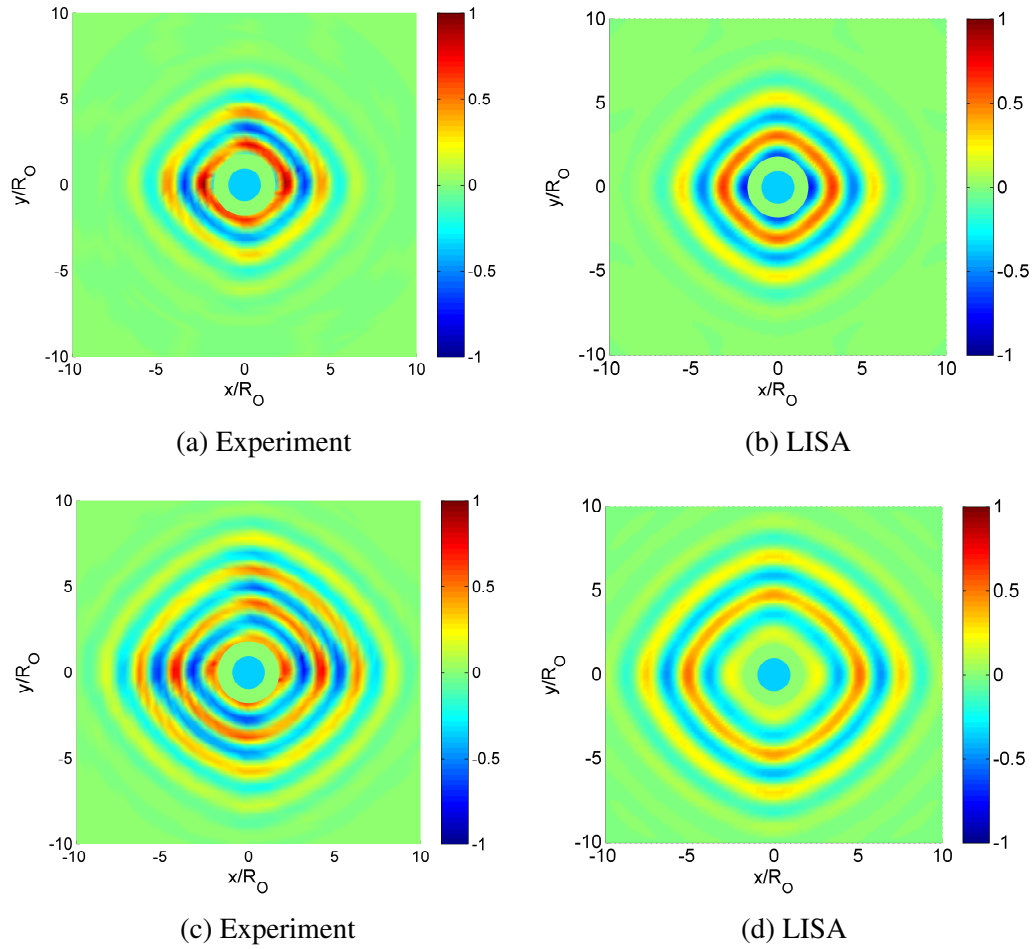


Figure 5.6: Out-of-plane normalized displacements in a cross-ply laminate $[0/90]_{3S}$ at (a)-(b) $55 \mu s$ and (c)-(d) $68 \mu s$. Distances from the center of the plate normalized by actuator radius ($R_O = 6.4 \text{ mm}$).

direction (parallel to x-axis) as compared to the 90-deg direction (normal to the x-axis). This is attributed to the effects of the stacking sequence in the laminate, where the top layer is oriented at 0 degrees.

For the quasi-isotropic specimen, as expected from the phase slowness diagram, there was no clear preferred direction for the GW. Although the plots look circular, the wave traveled slightly slower at an angle of 90 deg, as a result of the stacking sequence. The new LISA formulation was able to model the quasi-isotropic laminate as a result of the new terms included in the modified stiffness matrix.

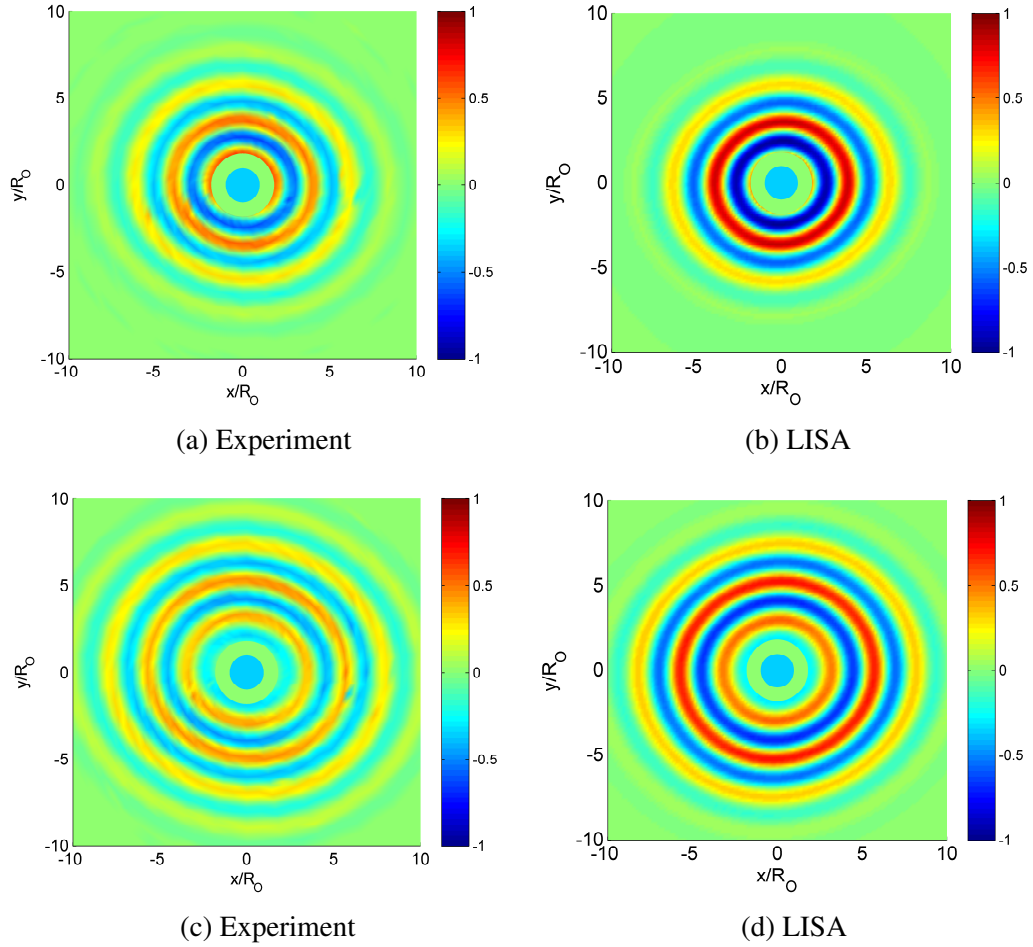


Figure 5.7: Out-of-plane normalized displacements in a quasi-isotropic laminate $[0/-45/45/90/90/-45/45/0]_s$ at (a)-(b) $68\mu s$ and (c)-(d) $78\mu s$. Distances from the center of the plate normalized by actuator radius ($R_O = 6.4\text{ mm}$).

5.1.6 CLoVER Actuator

For the second set of experiments, the CLoVER actuator was used to generate the GW. Snapshots of the out-of-plane component of the displacement at different times were recorded on the top surface of the laminate to compare the propagation pattern of the GW. Only one sector of the CLoVER was activated at a given time and is indicated by the color red on the yellow ring (representing the CLoVER transducer) in the plots. CLoVER1 was used for GW generation in uni-directional laminates, and the comparison between experiments and LISA simulations is shown in Fig. 5.8. The dimensions of the plate were

normalized by the outer radius of the CLoVER actuator.

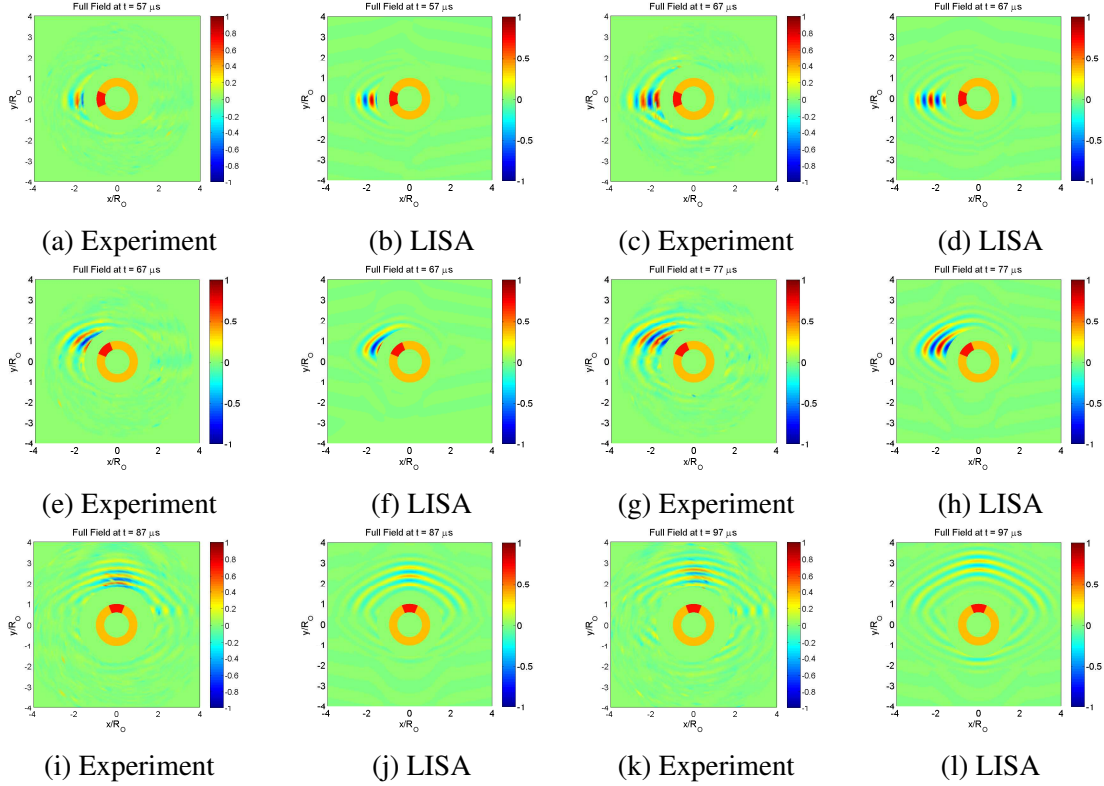


Figure 5.8: Out-of-plane displacement pattern for uni-directional $[0]_{12T}$ laminate when the input waves are incident along (a)-(d) 0 deg, (e)-(h) 45 deg and (i)-(l) 90 deg directions. Snapshots of the propagating waveform are shown at (a)-(b) $57\mu s$, (c)-(d) $67\mu s$, (e)-(f) $67\mu s$, (g)-(h) $77\mu s$, (i)-(j) $87\mu s$ and (k)-(l) $97\mu s$.

Figures 5.8(a)-(d) illustrate the case when the excited sector is aligned with the fiber direction. As predicted by the phase slowness diagram shown in Fig. 5.4(a), there was no steering effect, and the wave was captured by the LISA simulation with good agreement. Similar experimental and simulation results for the sector aligned at the 45-deg direction are shown in Figs. 5.8(e)-(h). In this case, the expected steering phenomenon was visible in both experiments and simulations. Further experiments and simulations were conducted for the sector aligned perpendicular to the fiber direction shown in Figs. 5.8(i)-(l). Although the phase slowness diagram is flat perpendicular to the fiber direction, the smaller radius of curvature results in higher steering effect on the propagating wave towards the fiber direction, which can be seen both in the experiments and simulations.

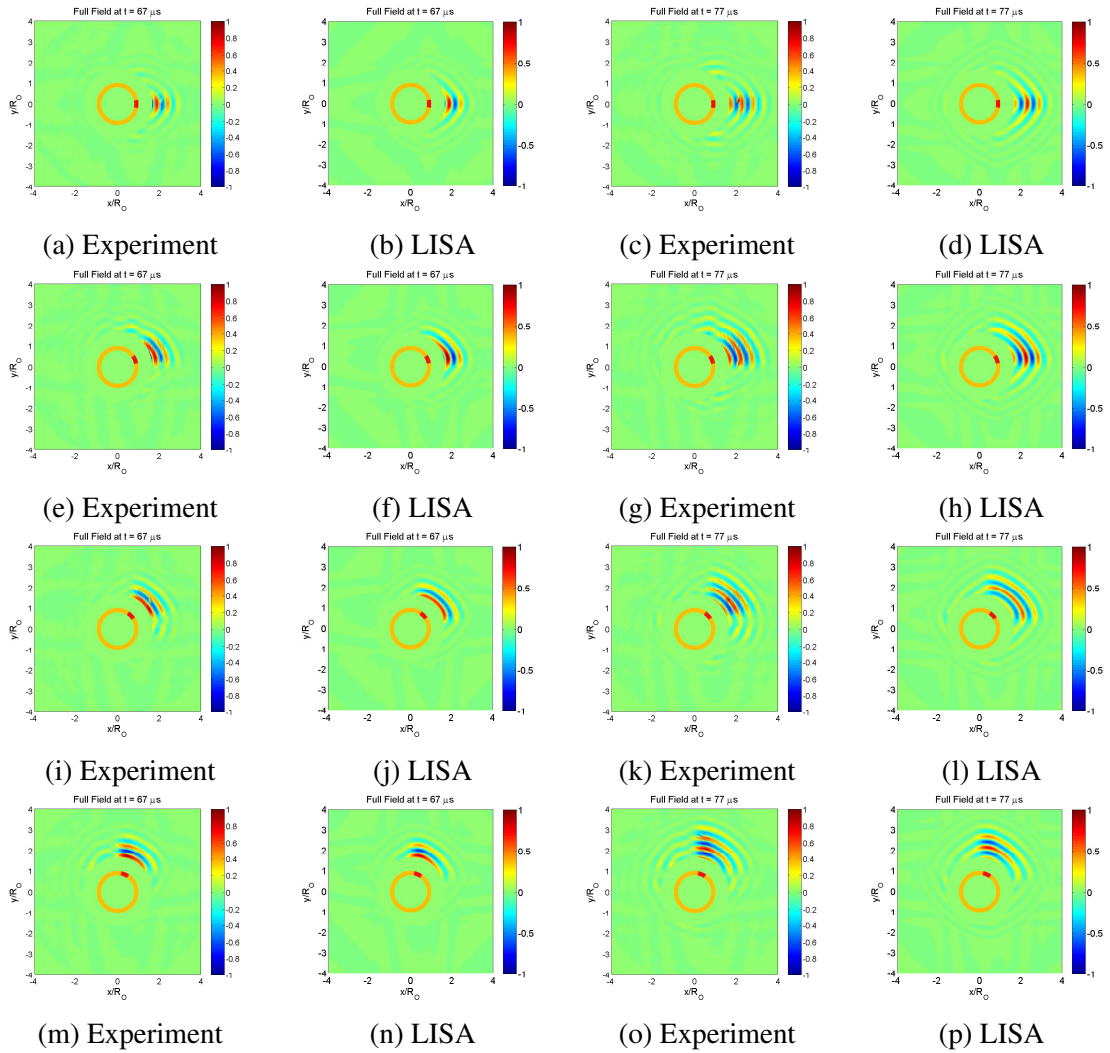


Figure 5.9: Out-of-plane displacement pattern for cross-ply $[0/90]_{3S}$ laminate when the input waves are incident along (a)-(d) 0 deg, (e)-(h) 22.5 deg, (i)-(l) 45 deg and (m)-(p) 67.5 deg directions. Snapshots of the propagating waveform are shown at $67\mu\text{s}$ for the two columns on the left and $77\mu\text{s}$ for the two columns on the right.

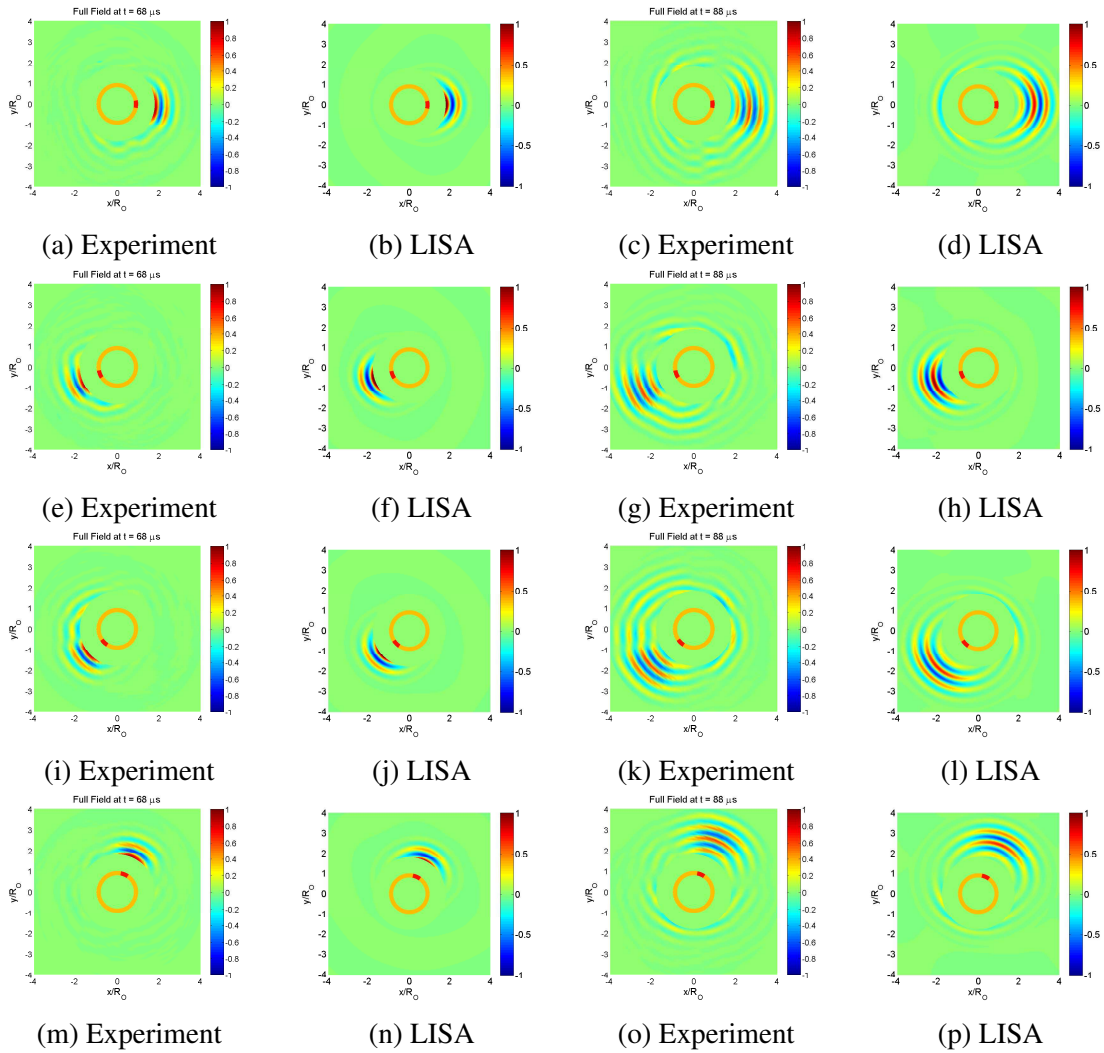


Figure 5.10: Out-of-plane displacement pattern for quasi-isotropic laminate when the input waves are incident along (a)-(d) 0 deg, (e)-(h) 180+22.5 deg, (i)-(l) 180+45 deg and (m)-(p) 67.5 deg directions. Snapshots of the propagating waveform are shown at 68 μs for the two columns on the left and 88 μs for the two columns on the right.

The cross-ply laminate was instrumented with CLoVER2. The top lamina in the cross-ply laminate was oriented along the horizontal direction (parallel to x-axis). In Figs. 5.9(a)-(d), the sector along the 0-deg azimuthal position was activated, and the resulting GW pattern showed no steering effect, which is consistent with what was expected from the phase slowness diagram in Fig. 5.4(b). Figures 5.9(e)-(h) show a similar pattern when the sector oriented along 22.5 deg to the fiber direction was activated, but in this case the GW was observed to steer towards the horizontal direction, as seen from the slowness diagram. Figures 5.9(i)-(l) show a similar pattern when the sector oriented along the 45-deg direction was activated, but in this case the GW was observed to have minimal steering, as the normal to the phase slowness diagram is almost aligned with the radial direction. Figures 5.9(m)-(p), where the sector oriented along the 67.5-deg direction is activated show a pattern similar to Figs. 5.9(e)-(h). In this case, the GW was observed to steer towards the vertical direction, as expected from the slowness diagram.

In Figs. 5.10(a)-(d), the sector along the 0-deg direction was active and GW propagation is compared between LISA and experiments. As expected from the slowness curves, no energy steering was observed. Figures 5.10(e)-(h) show a similar pattern rotated by 22.5 deg from the horizontal position, corresponding to the active sector. Steering was still not visible, which agrees with what is expected from the slowness curve (Fig. 5.4(c)). Figures 5.10(i)-(l) and Figs. 5.10(m)-(p) show similar propagation characteristics, and the GW propagation was seen to have no steering.

From the results shown above for uni-directional, cross-ply, and quasi-isotropic laminates, it can be deduced that the new LISA formulation is able to accurately capture the effect of additional terms in the stiffness matrix resulting from a multi-layer stacking sequence.

5.1.7 Preliminary GW Studies in Sandwich Foam Core Panels

Preliminary experimental and numerical studies using LISA were performed to assess the feasibility of GW approaches for delamination monitoring of the interface between the sandwich core and the composite facesheets. The particular architecture of interest, shown in Fig. 5.11(a), consists of surface-bonded transducers on the inner part of a sandwich structure to emit GW used for interrogation of the interface between the sandwich core and the outer composite facesheet.

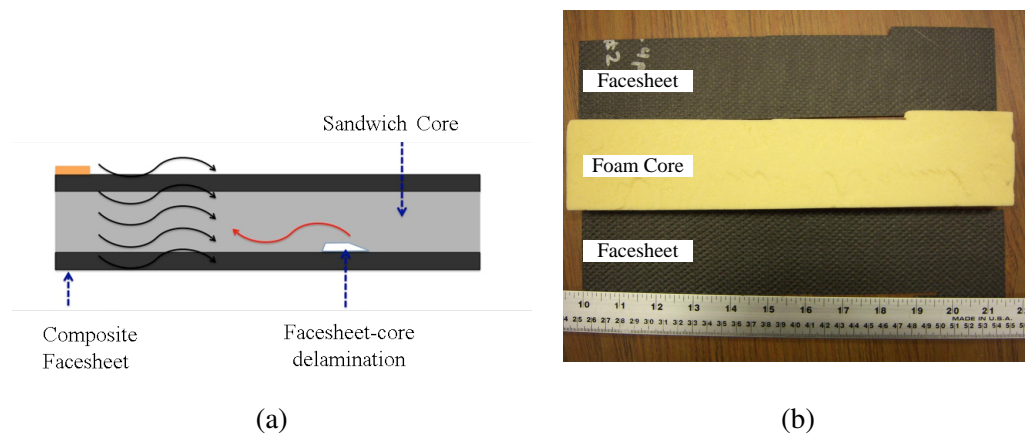
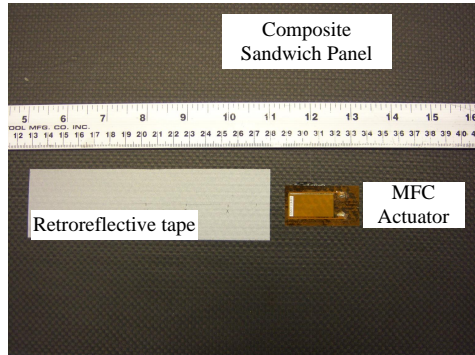


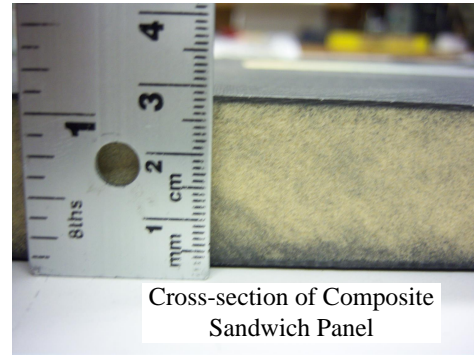
Figure 5.11: (a) Schematic of GW-based damage detection architecture for sandwich panels. (b) Components of the sandwich foam core.

The composite sandwich specimen, composed of a closed-cell polyurethane foam LAST-A-FOAM ®FR-6710, sandwiched between facesheets consisting of four plies of T300B-3K plain weave carbon fiber fabric with the Epon 862 epoxy is shown in Fig. 5.11(b). The facesheets and core have thickness of 1 mm and 24 mm, respectively. The mechanical properties were obtained from Refs. [134, 135]. The specimen had a 0.5×0.3 m rectangular geometry.

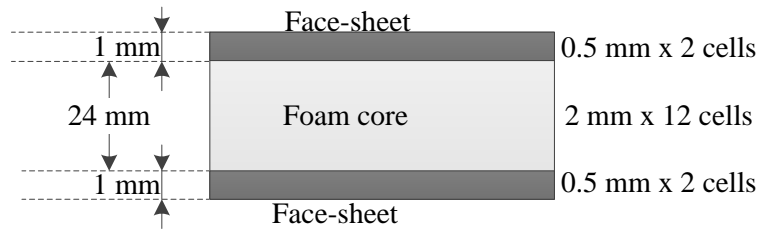
Guided waves were generated in the composite sandwich specimen with the help of an MFC actuator, as shown in Fig. 5.12(a), bonded to the top surface of the panel. The actuator was oriented along the length of the panel and was placed at an optimum location to avoid boundary reflections. The transducer used in the experiments was 28-mm long and 15-mm



(a)



(b)



(c)

Figure 5.12: (a) Composite sandwich specimen with MFC actuator and retro-reflective tape. (b) Cross section of the composite foam core sandwich. (c) Cross-sectional schematic of the sandwich panel in UM-LISA simulations.

wide, and it was excited with a 3.5-cycle Hann-modulated toneburst, shown in Fig. 5.2(a). GW were generated with center frequencies varying between 10 kHz and 200 kHz with an interval of 10 kHz. The GW field was measured using a Polytec PSV-400 scanning laser vibrometer by recording the out-of-plane velocities in a configuration as shown in Fig. 5.3. A patch of retroreflective tape, shown in Fig. 5.12(a), was attached to the top and bottom surfaces to ensure consistent laser signal strength. The out-of-plane velocity was measured along a segment aligned with the actuator on the top surface and bottom surface of the composite sandwich panel. The amplitude of out-of-plane displacement, calculated by integrating the velocity measured from the laser experiments, was compared between

the top surface and bottom surface.

Numerical simulations were performed on the composite sandwich panel with in-plane (X_1X_2 -plane) discretizations of 1×1 mm. The cross-section of the sandwich panel (Fig. 5.12(b)) was discretized with facesheets having Δx_3 equal to 0.5 mm and foam core with Δx_3 equal to 2 mm (Fig. 5.12(c)). The discretization was chosen to satisfy the CFL criterion and avoid excessive simulation times. As described in the experiments, the excitation was prescribed on the top surface of the model in the shape of a rectangular MFC. In-plane displacements along the length of the actuator parallel to X_1 were considered for actuation. The out-of-plane displacement was recorded on the top surface of the sandwich panel and the Hilbert transform of the signal determined the peak of the arriving signal. The scaled ratio of the amplitudes of the signals on the bottom and top surfaces was plotted at different distances from the center of the actuator, as shown in Fig. 5.13. From those, it is apparent that lower frequencies are suitable for GW testing as more energy propagates to the bottom facesheet as compared to the higher frequencies. The 3D numerical simulations based on LISA were able to capture the trend in the GW propagation characteristics accurately. More experiments and numerical simulations are required at lower frequencies to investigate if the response at 10 kHz is a global peak.

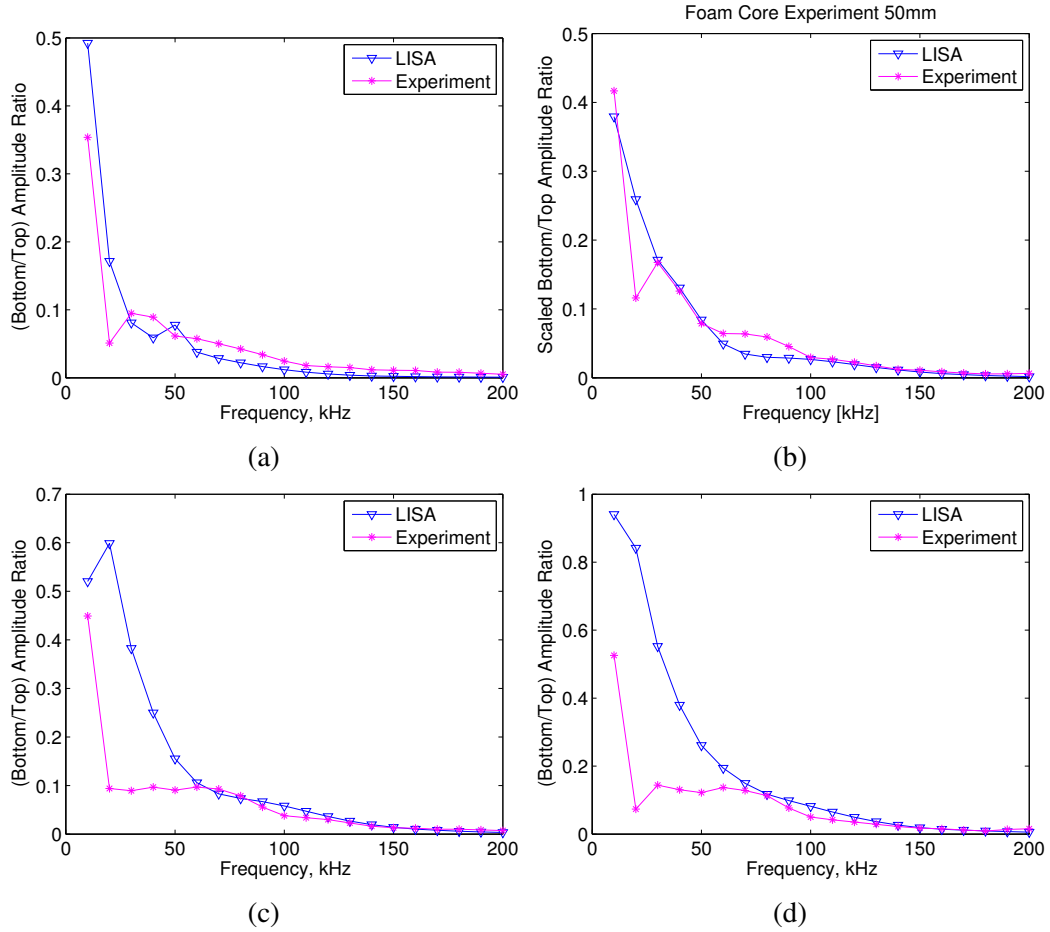


Figure 5.13: Ratio of the amplitudes of signals on the bottom surface and top surface for different frequencies at a distance of (a) 40 mm, (b) 50 mm, (c) 60 mm and (d) 70 mm from the center of the MFC actuator.

5.2 Simulated Damage: Concentrated Mass

The damage interaction study was carried out on the quasi-isotropic laminate $[0/-45/45/90/90/-45/45/0]_S$. The GW were generated using a PZT disc actuator (PZT 5A, $R_o=6.4$ mm) bonded to the top surface of the laminate. A simulated damage was introduced to the structure using a concentrated mass in the form of a prismatic steel bar ($E=200$ GPa, $\nu=0.3$, $\rho=8000$ kg/m³). The bar had a square cross-section with a side of 22 mm and mass of 0.65 kg, and it was placed at a constant distance of 125 mm from the center of the actuator. This particular damage was selected because of its mobility to different radial

and azimuthal positions on the structure, and also to avoid any permanent damage to the plate. The GW were monitored using the CLoVER (CLoVER2) transducer placed around the PZT actuator, as shown in Fig. 5.14(a). In the damage experiments, the concentrated mass was placed with the sharp edge facing the PZT actuator, as shown in Fig. 5.14(b), while in the simulations the flat edge of the bar faces the actuator for modeling simplicity. This change in damage orientation does not significantly affect the detection of damage, as discussed by Salas and Cesnik [30].

To visualize the effect of a concentrated mass on the out-of-plane displacement component of the propagating GW in the quasi-isotropic plate, LISA simulations were conducted on the pristine plate and the one with the simulated damage. In Fig. 5.15, snapshots of the normalized out-of-plane displacement component were recorded for the top-surface of the quasi-isotropic laminate. The fibers in the top ply of the laminate were oriented in the horizontal direction. Comparison of the out-of-plane displacement between the pristine laminate and the one with simulated damage is presented for different times. The simulated damage is represented as a black square in the plots and the dimensions of the simulated damage are normalized with the PZT radius. The in-plane dimensions of the composite laminate were normalized by the radius of the PZT actuator ($R_o = 6.35$ mm). It can be seen in Figs. 5.15(a)-(h) that the propagation pattern was similar for both pristine and simulated damage laminates. The difference between the pristine and simulated damage laminate can be clearly seen in the subsequent time instants represented in Figs. 5.15(i)-(t). As expected, only a fraction of the incident energy was reflected back along the incident direction, and almost no displacement was seen in the wake of the simulated damage. The wave front reflected from the simulated damage confirms that LISA is able to capture the presence of simulated damage in the composite laminate.

For the damage interaction study experiments, a standard pulse-echo method was employed. To analyze the reflections from the simulated damage site, the (baseline) signal of the pristine structure was subtracted from the signal obtained for the structure with the

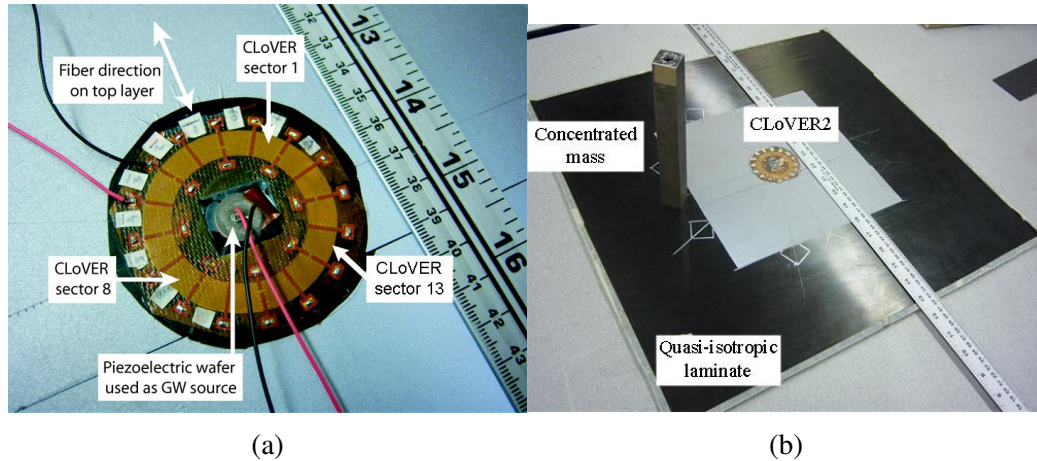


Figure 5.14: (a) Details for the PZT disc and CLoVER configuration used in the damage interaction studies on quasi-isotropic laminate. (b) Experimental setup for the damage interaction studies.

damage. In particular, the peak-to-peak amplitude of the difference was used as the damage indicator. The simulated damage was aligned with the central radial lines for different sectors, one at a time, and the response was recorded by all of the other CLoVER sectors. More details pertaining to the experimentation can be found in Ref. [30]. The LISA model was created to match the experimental setup, with the exception that the azimuthally-varying position of the simulated damage was replaced by rotating the material properties of the plate in the opposite direction along with the CLoVER sectors. Simulations were then conducted for the different simulated damage positions.

Figures 5.16–5.18 show the comparison between the experimental data and LISA simulations for different cases of simulated damage alignment with the transducer. The “Sensor Index” in the plots corresponds to the number assigned for each sector of the CLoVER as shown in Fig. 5.14(a). The main observation from the comparison results is that the CLoVER transducer is effective in identifying the azimuthal location of the simulated damage and rejecting transverse signals coming to it (filtering effect) [29]. Consistent higher amplitudes were observed in the sectors aligned to the damage site. It is interesting to observe that the sectors diametrically opposite to the aligned sector also detected the reflected

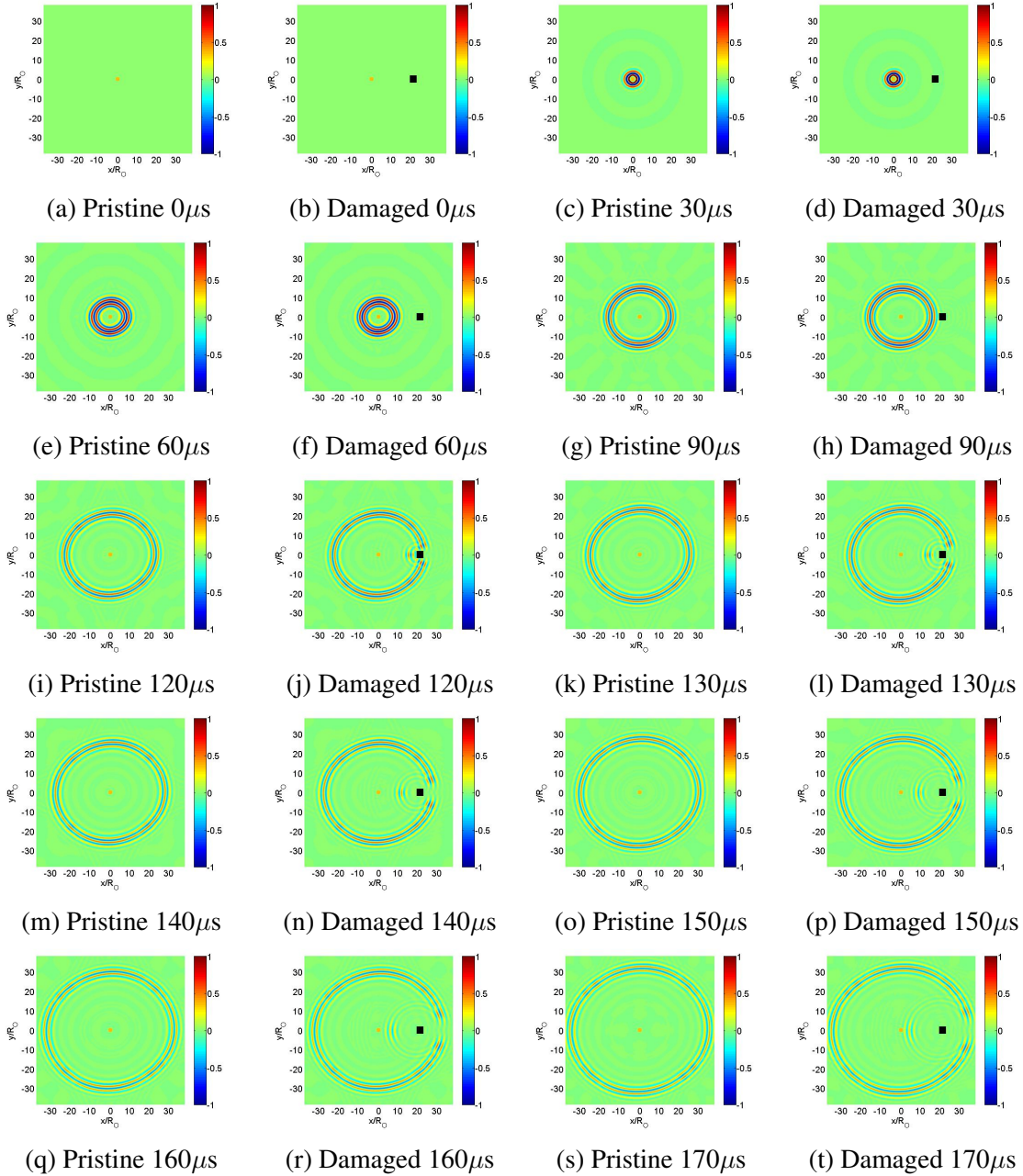


Figure 5.15: Out-of-plane displacement pattern comparison between pristine and simulated damage quasi-isotropic laminates. The black square represents the position of the damage.

signal, something not observed in the experiments. This is attributed to the fact that the LISA simulations did not take into account the damping effects of the CLoVER transducer and its adhesive layer nor the damping coming from the center actuator PZT disc when the reflected wave traveled from one sector to the diametrically opposite one. This issue can

be rectified by keeping track of the reflected wave, as the sector facing the damage would receive the wave ahead of the sector diametrically opposite to it.

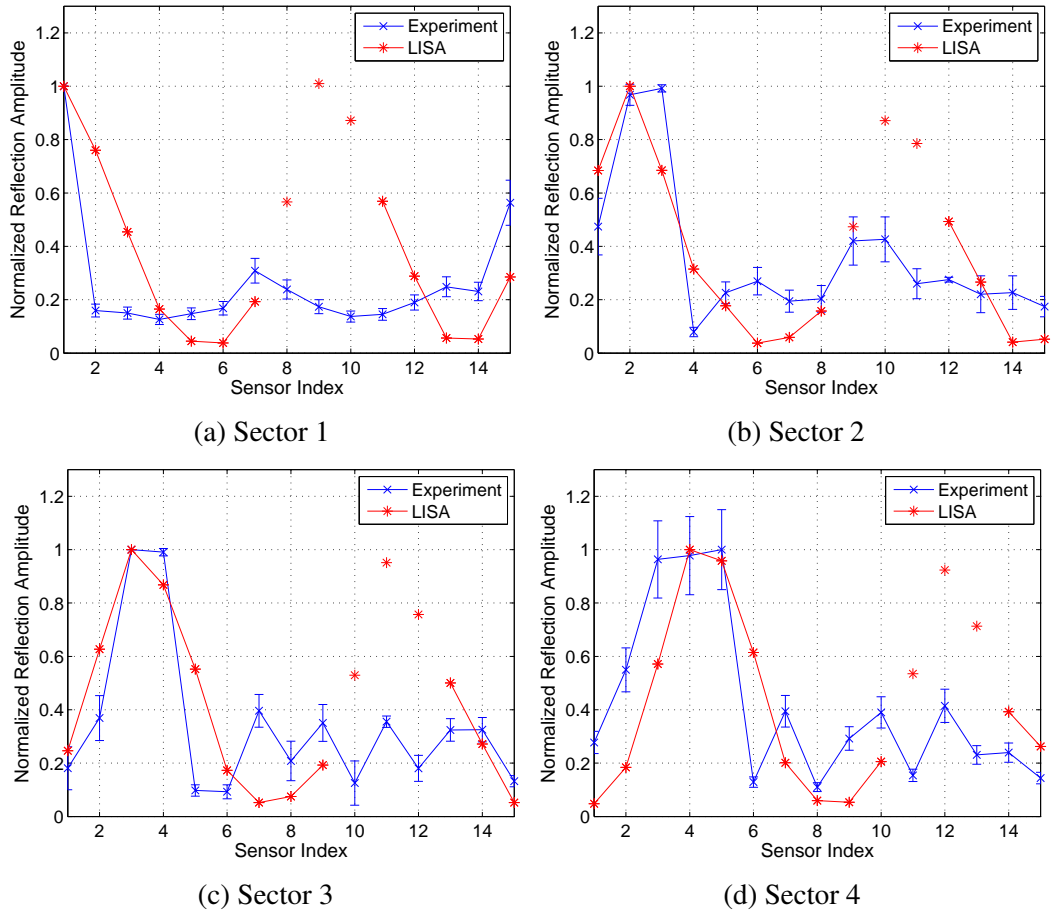


Figure 5.16: Comparison between LISA simulations and experiments for the normalized peak-to-peak reflection amplitude recorded with the CLoVER transducer in quasi-isotropic $[0/45/-45/90/90/-45/45/0]_S$ laminate when the damage was aligned with (a) sector 1, (b) sector 2, (c) sector 3, and (d) sector 4

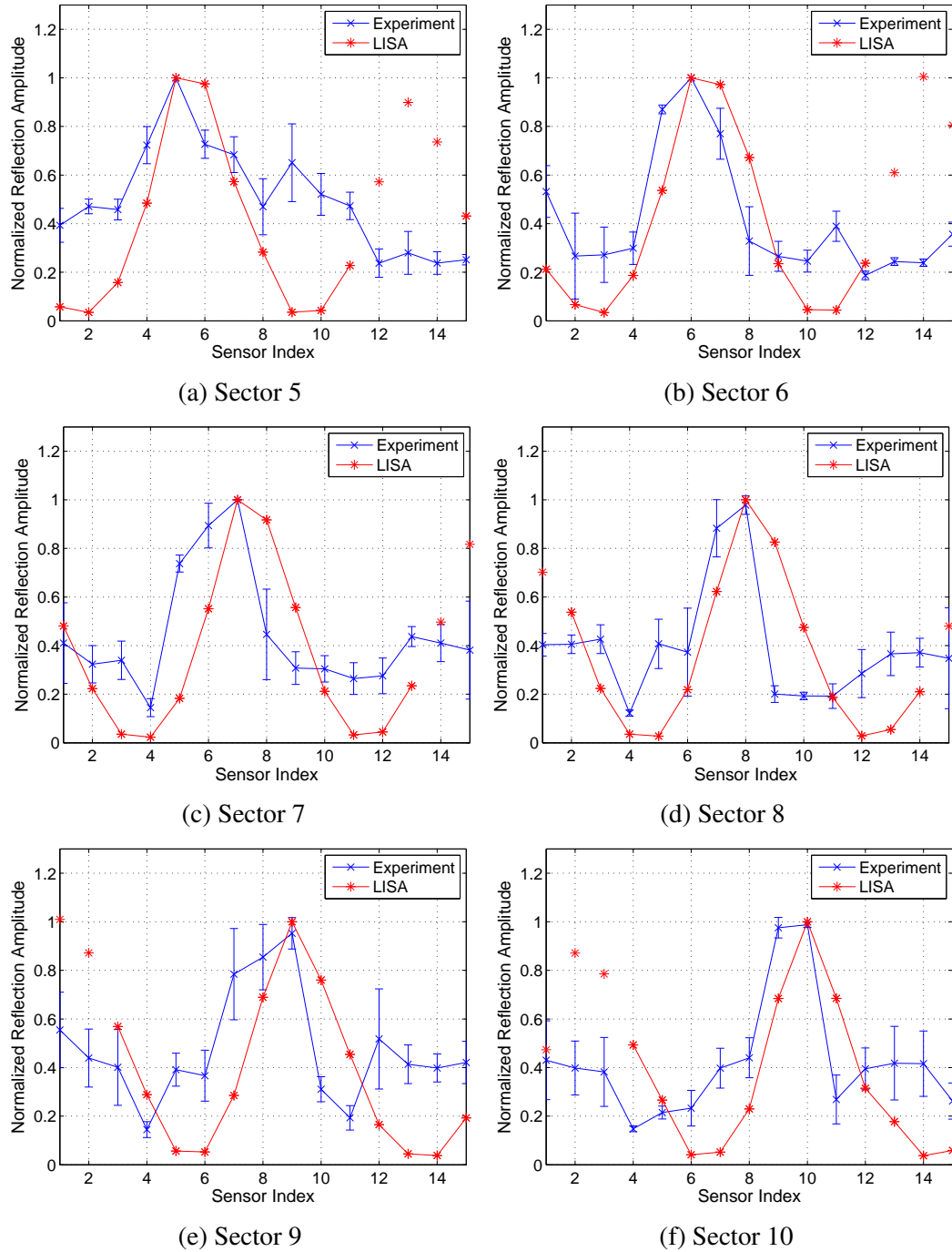
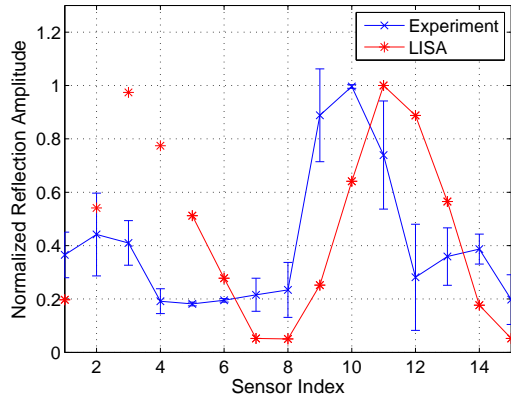
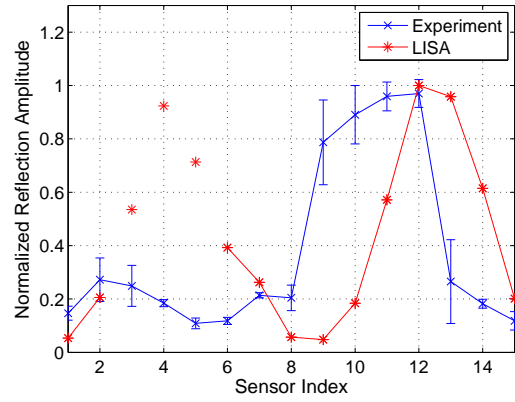


Figure 5.17: Comparison between LISA simulations and experiments for the normalized peak-to-peak reflection amplitude recorded with the CLoVER transducer in quasi-isotropic $[0/45/-45/90/90/-45/45/0]_S$ laminate, when the damage was aligned with (a) sector 5, (b) sector 6, (c) sector 7, and (d) sector 8, e) sector 9, (f) sector 10,

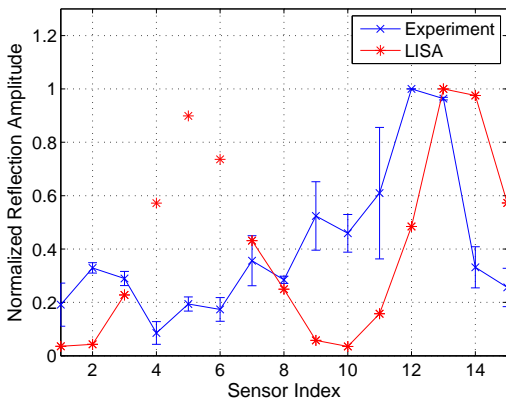
It is also interesting to note that in Figs. 5.16(a), 5.17(b), 5.17(e) and 5.18(d) the



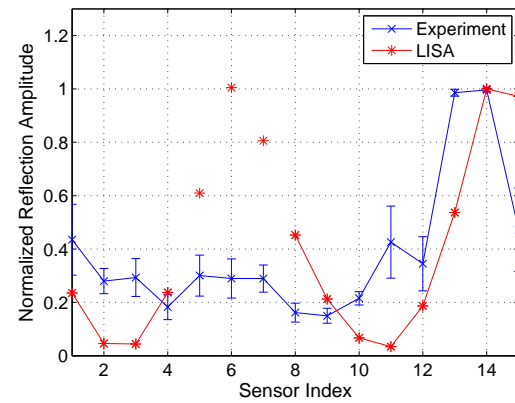
(a) Sector 11



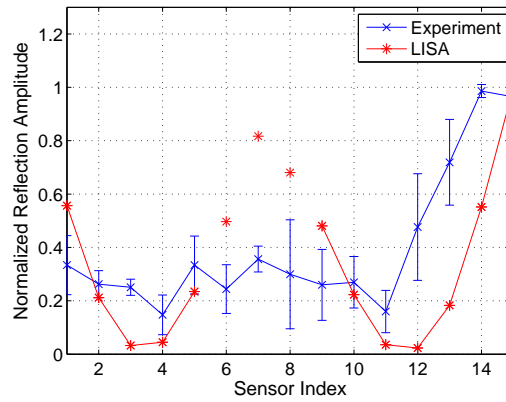
(b) Sector 12



(c) Sector 13



(d) Sector 14



(e) Sector 15

Figure 5.18: Comparison between LISA simulations and experiments for the normalized peak-to-peak reflection amplitude recorded with the CLoVER transducer in quasi-isotropic $[0/45/-45/90/90/-45/45/0]_S$ laminate, when the damage was aligned with (a) sector 11, and (b) sector 12, (c) sector 13, (d) sector 14, and (e) sector 15

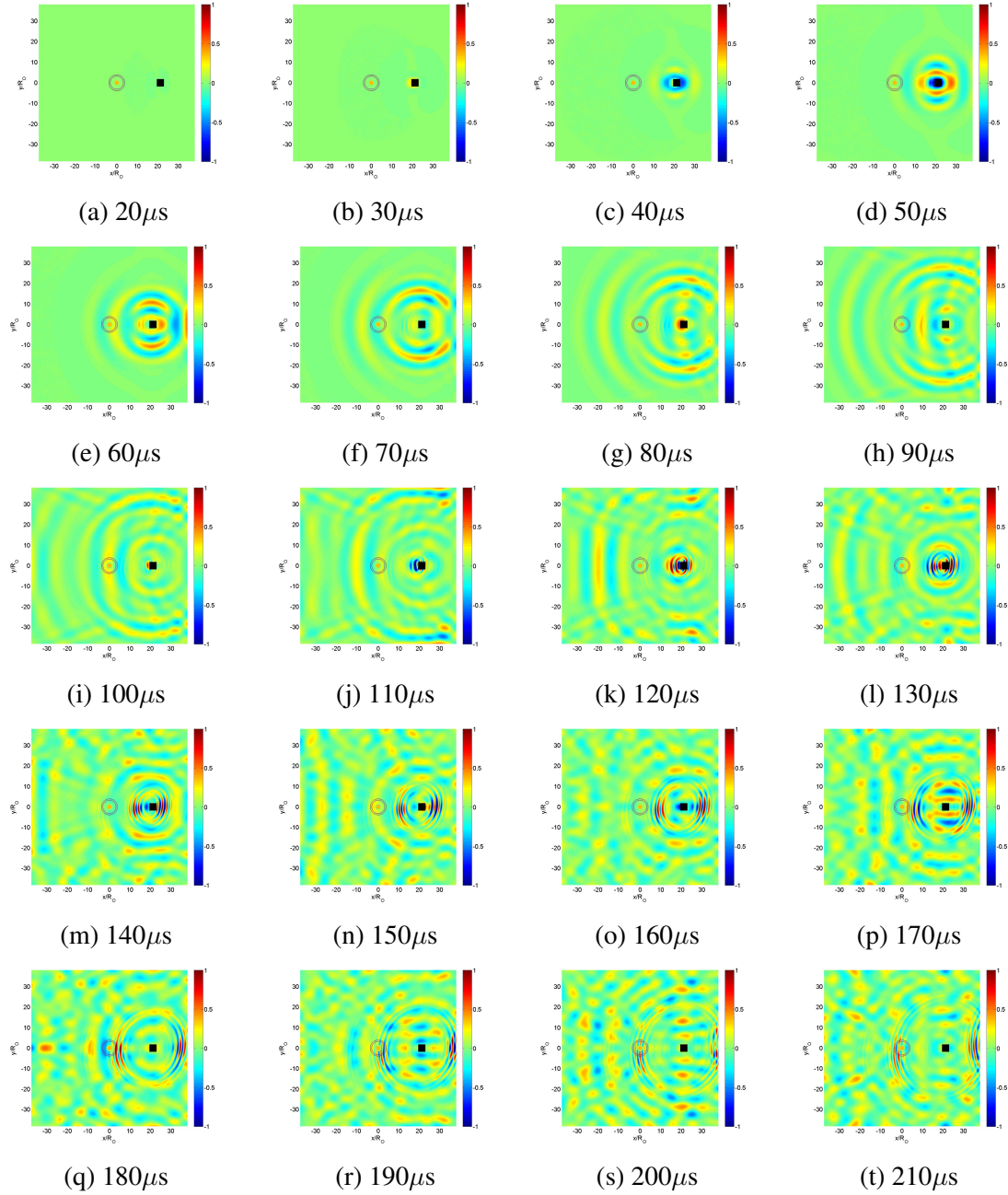


Figure 5.19: In-plane displacement component along the X -direction in the quasi-isotropic plate. It is obtained by subtracting the displacement field of the pristine case from the damaged one. GW are generated by the PZT disc shown as yellow disc and the CLOVER is shown as a translucent annulus around it; the damage is indicated by the black square in the right side of the plate.

diametrically-opposite sector had an amplitude higher than the sector facing the damage. This unexpected behavior can be explained by studying the in-plane displacement compo-

ment of the reflected wave, as shown in Fig. 5.19, where the damage is aligned with Sector 1. In Fig. 5.19, the in-plane displacement component along the horizontal axis (X_1 -axis) is considered. The material coordinate system of the plate along with the CLoVER sensor was rotated to align Sector 1 with the damage placed along the X_1 -axis. The normalized difference of the signals between the simulated damage case and the pristine one is plotted in Fig. 5.19. It can be seen that there is a significant amplitude associated with the fundamental symmetric mode (S_o) reflected from the damage site. The reflected fundamental anti-symmetric mode (A_o) originates from the damage site around $90 \mu s$ (Fig. 5.19(h)) and travels towards the CLoVER transducer. The symmetric wave travels significantly faster than the anti-symmetric wave and there is interference between the reflected S_o mode from the edge of the plate and the A_o arriving at the CLoVER transducer for sensing. This interference of signals contributed to higher amplitudes seen in the diametrically-opposite sector to the sector facing the damage, which received the reflected signal directly from the damage site.

5.3 Wave Generation Modeling

5.3.1 Displacement Behavior of Actuator Nodes

This section presents three actuation methods to generate GW in LISA. While two of the methods are indirect representation of the actuator effects through prescribed displacement, the third one is a direct representation of the electromechanical coupled effects of the piezo actuator by the piezo-coupled implementation. For PD methods, equivalent response of the actuator as a displacement field is enforced as radially increasing in-plane displacements (method-I) or out-of-plane displacements (method-II) with a gaussian profile. It should be noted that, while the input excitation is prescribed using a particular component(s) of displacement, the other component(s) of displacement are allowed to develop unhindered. The PC formulation is implemented by enforcing a potential difference

across the “Top Nodes” and “Bottom Nodes” of the actuator, as shown in Fig. 2.10. The components of the displacement field at the actuator nodes which constitute the actuator and substrate interface are monitored to compare the different actuation methods. The simulations are performed for an isotropic plate and several composite laminated plates.

5.3.1.1 Isotropic Substrate

First, an isotropic plate was considered for comparing different actuation models. An isotropic substrate is beneficial as it decouples the effect of azimuthal variation of the substrate’s material properties, which might affect the actuator behavior.

Figure 5.20 shows the in-plane displacement pattern for the actuator on an isotropic substrate. The first column in Fig. 5.20 shows the time steps where the different actuation methods were compared. The time steps for comparison were chosen to have large amplitudes at the actuator nodes. The second, third and fourth column in Fig. 5.20 present the displacement pattern for different actuation methods. The axes are normalized by the radius of the actuator (R_o) and the arrows represent the direction and amplitude of the in-plane components of the displacement field. The contours show the lines with same amplitude. From the figure, it is clear that for the isotropic case, all the actuation methods show an axisymmetric displacement pattern, which is expected as there is no azimuthal preference based on material properties. It is interesting to note the spacing between the contour lines is different for various types of actuator modeling. For the PD method-I, the contour lines are uniformly spaced, reflecting the radially increasing displacement. In PD method-II, the contour lines are not equally spaced, but there is no variation in the contour patterns, which confirms that the non-uniformness of the contour lines is a result of the gaussian enforcement in method-II and the material coupling between the in-plane displacements and out-of-plane displacement component. Finally, in the PC formulation, we see that the contours are not uniformly spaced and the contour pattern is changing, which indicates that the PC formulation is allowing the actuator nodes to develop the GW without

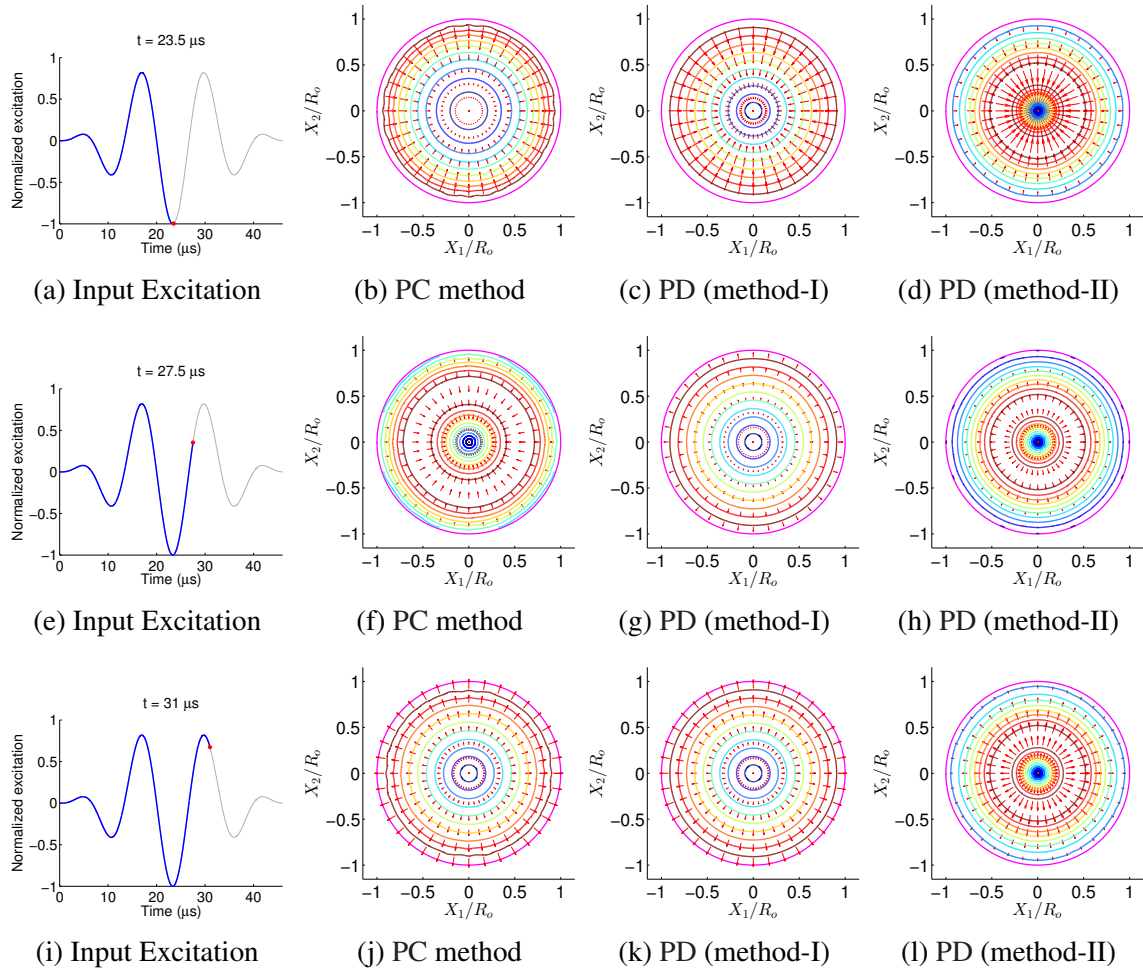


Figure 5.20: Snapshots of the in-plane displacement pattern for the actuator nodes for an isotropic substrate. Each row corresponds to a particular time step during the actuation. The first column represents the particular time step where the actuator nodes are compared. The second column shows the actuator nodes in the piezo-coupled actuation case. The third column is for the prescribed displacement method-I input, and the fourth column is for the prescribed displacement method-II input.

direct interference in the displacement pattern. For the last time result presented, the PD method-I shows a very good correlation with the PC solution which is only a coincidence.

Figure 5.21 shows the out-of-plane displacement pattern for the actuator on the isotropic substrate. The first column shows the time steps where the different actuation methods were compared. Similar to before, the time steps for comparison were chosen to have large amplitudes at the actuator nodes. The second, third and fourth column in Fig. 5.21 present the

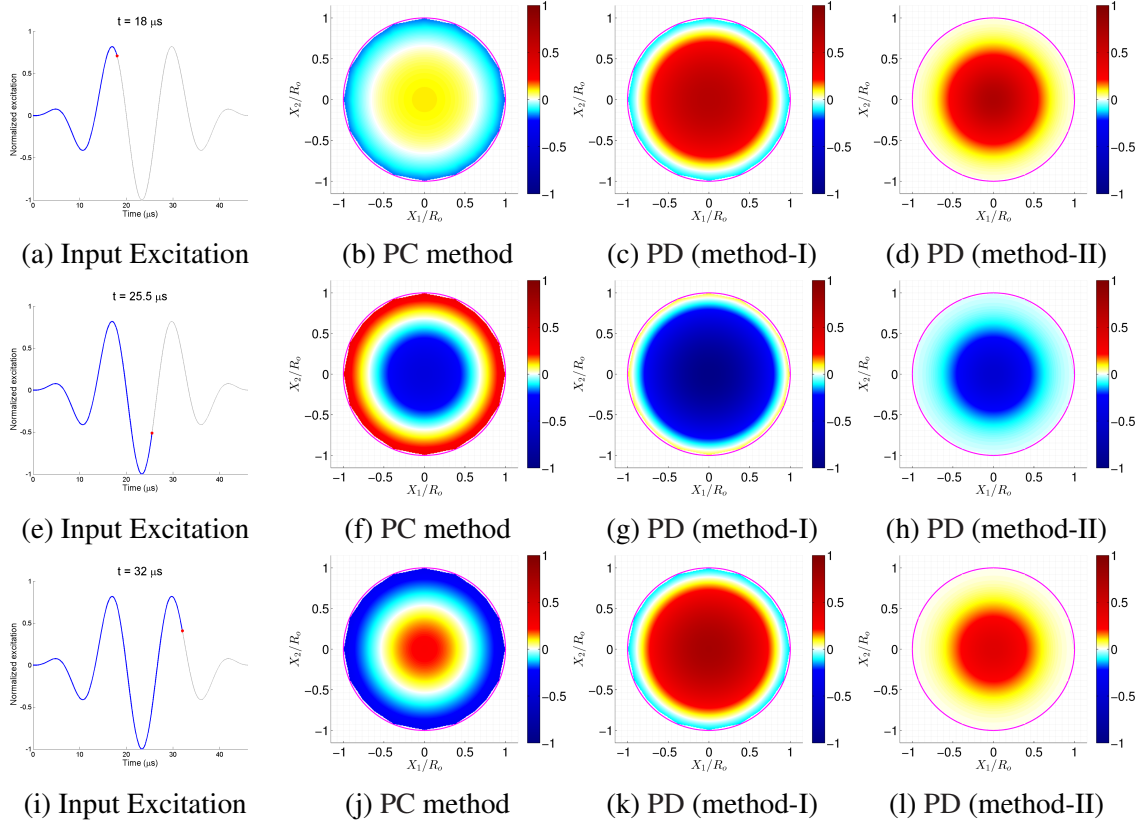


Figure 5.21: Snapshots of the out-of-plane displacement pattern for the actuator nodes for different actuator models for an isotropic substrate. Each row corresponds to a particular time step during the actuation. The first column represents the particular time step where the actuator nodes are compared. The second column shows the actuator nodes in the piezo-coupled actuation case. The third column is for the prescribed displacement method-I input, and the fourth column is for the prescribed displacement method-II input.

out-of-plane displacement pattern for different actuation methods. The axes are normalized by the radius of the actuator (R_o) and the out-of-plane displacement is normalized by the maximum observed displacement amplitude. The axisymmetric displacement pattern is also observed for the out-of-plane displacement component. The important feature is that both PD methods are only able to achieve either a positive or negative displacement, but not a combination of displacement patterns as seen in the case of the PC formulation.

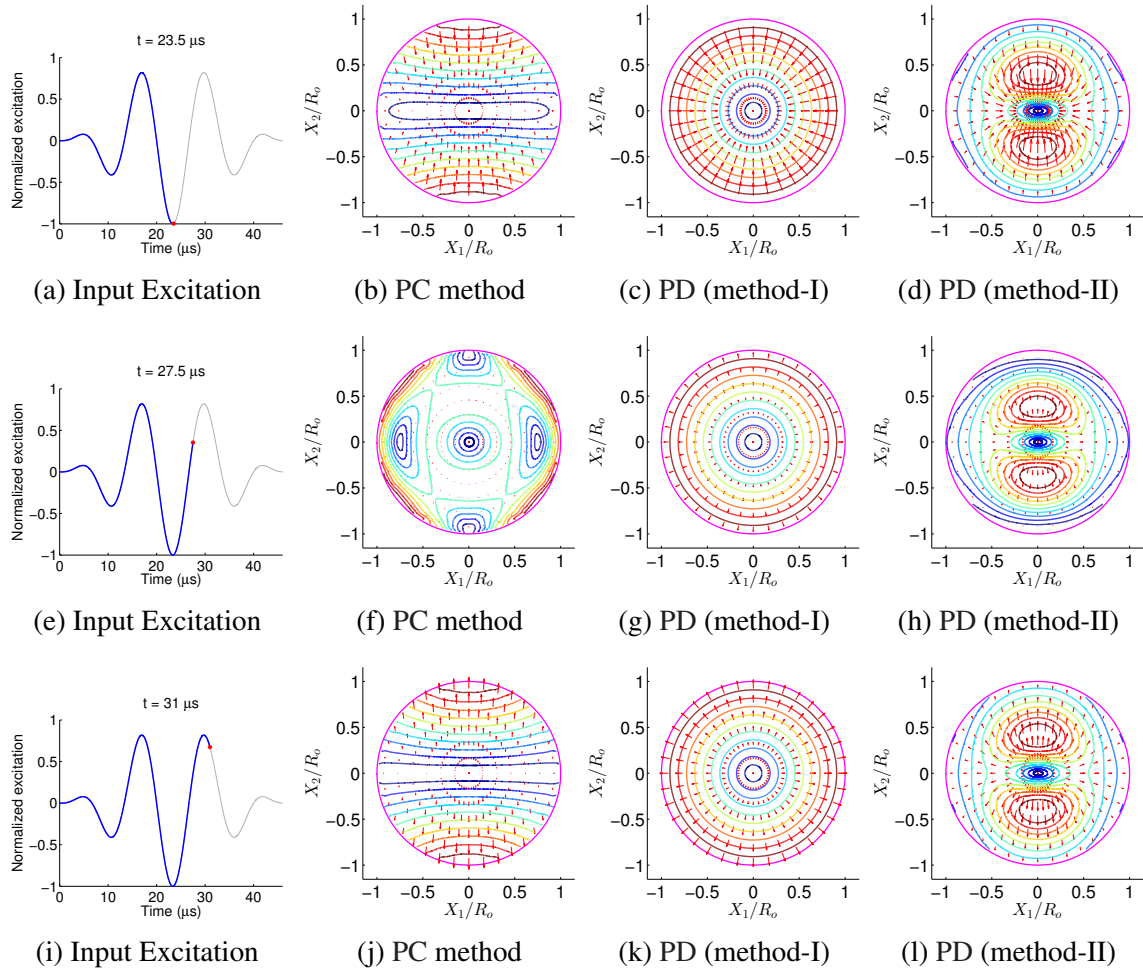


Figure 5.22: Snapshots of the in-plane displacement pattern for the actuator nodes for different actuator models for a uni-directional laminate. Each row corresponds to a particular time step during the actuation. The first column represents the particular time step where the actuator nodes are compared. The second column shows the actuator nodes in the piezo-coupled actuation case. The third column is for the prescribed displacement method-I input, and the fourth column is for the prescribed displacement method-II input.

5.3.1.2 Uni-directional $[0]_{12T}$ substrate

Next, a uni-directional $[0]_{12T}$ laminate was considered for comparing different actuation models. Figure 5.22 shows the in-plane displacement pattern for the actuator bonded on the uni-directional laminate. As before, the first column in Fig. 5.22 shows the different time steps where the actuation methods are compared. The second, third and fourth columns in Fig. 5.22 present the displacement pattern for different actuation methods. The

axes are normalized by the radius of the actuator (R_o), the arrows represent the direction and amplitude of the in-plane components of the displacement field, and the contours show the lines with same amplitude. The displacement pattern of the actuator nodes show the effect of material anisotropy on GW generation. As expected, PD method-I shows the same behavior of actuator nodes for both the isotropic and uni-directional cases. Although the displacement pattern for PD method-II shows the effect of material properties, the uniformity of behavior indicates that the material coupling between the enforced out-of-plane displacement and in-plane displacements is the only factor determining the displacement pattern, and that does not accurately approximate the more complex piezo actuator effects as captured by PC method.

Figure 5.23 shows the out-of-plane displacement pattern for the actuator nodes for a uni-directional laminate substrate. The first column in Fig. 5.23 shows the time steps where the different actuation methods were compared. The second, third and fourth columns in Fig. 5.23 present the out-of-plane displacement pattern for the different actuation methods. The axes are normalized by the radius of the actuator (R_o) and the out-of-plane displacement is normalized by the maximum observed displacement amplitude. Similar to the in-plane displacement pattern for this uni-directional laminate (Fig. 5.22), one can see that the PD method-II has a predetermined gaussian profile for the out-of-plane displacement as given, and the PD method-I only displays the effects of material coupling due to the in-plane actuation. Both, however, miss the complex pattern displayed in the PC solution. This is due to the fact that the PC method incorporates both the mechanical coupling between the actuator and the substrate, and also the electrical response of the actuator under external applied voltage, which is not present in the PD-based methods.

5.3.2 Validation of GW Generation

Experimental validation studies for the GW generation schemes were carried out on a cross-ply $[0/90]_{3S}$ laminate of thickness 1.5 mm. For this study, out-of-plane displacements

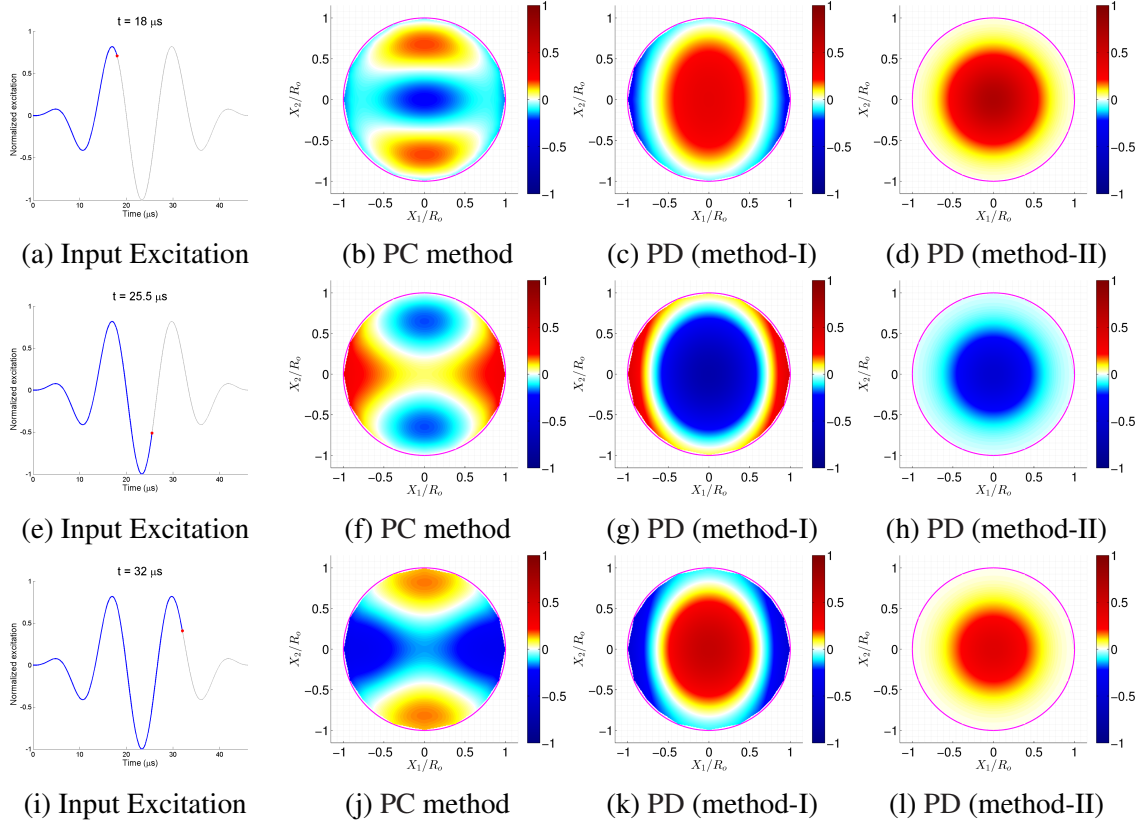


Figure 5.23: Snapshots of the out-of-plane displacement pattern for the actuator nodes for different actuator models for a uni-directional laminate. Each row corresponds to a particular time step during the actuation. The first column represents the particular time step where the actuator nodes are compared. The second column shows the actuator nodes in the piezo-coupled actuation case. The third column is for the prescribed displacement method-I input, and the fourth column is for the prescribed displacement method-II input.

were chosen as the comparison parameter to evaluate the quality of different methods of actuator representation in UM-LISA. The GW field was measured using a Polytec PSV-400 scanning laser vibrometer in the configuration shown in Fig. 5.3. The mechanical properties of the composite material are shown in Table 5.1. A piezoceramic disc (PZT-5A) transducer of radius 6.5 mm (R_o) and a thickness of 0.23 mm was used to generate GW. A 3.5-cycle Hann-modulated toneburst at a center frequency of 75 kHz was used in the experiments. The displacements were measured along and perpendicular to the fiber direction of the top lamina. The distances chosen for comparison were 40 mm, 60 mm and 80 mm from the center of the actuator.

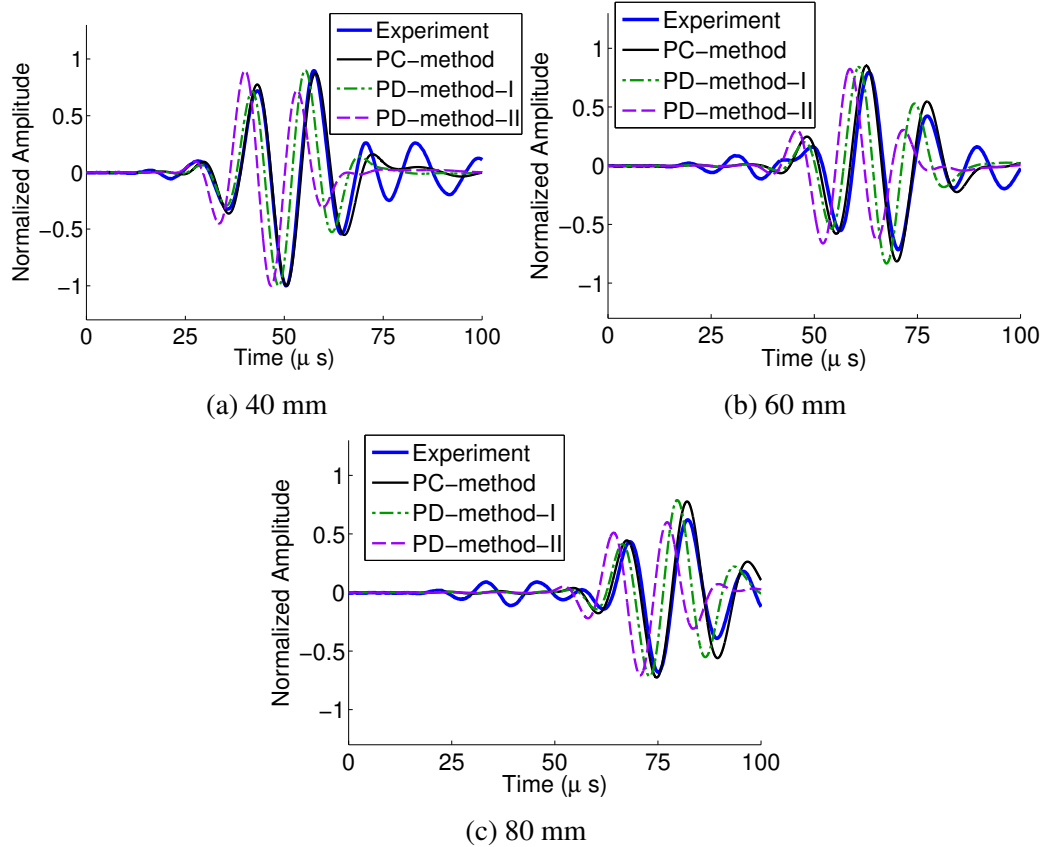


Figure 5.24: Comparison between experimental data and LISA simulations along the 0 deg azimuthal direction for different actuation methods at varying distances from the center of the actuator.

Figure 5.24 shows the comparison for out-of-plane component of the displacement field between the experimental data and LISA simulations along the fiber direction of the top lamina (azimuthal direction of 0 deg). The signals presented are normalized by the maximum amplitude of the respective case at a distance of 40 mm and azimuthal direction of 0 deg from the center of the actuator. To account for the phase shift caused by the electronic acquisition system, a fixed shift of $10 \mu s$ was applied to the experimental data. From Fig. 5.24 it is clear that UM-LISA with the PC method has a significantly better correlation with the experimental data than the PD methods. Although PD (method-I) is able to capture the general shape of the propagating wave, there is a significant drop in correlation as the phase difference increases with time. On the other hand, PD (method-II) shows a very

low correlation with the experimental data.

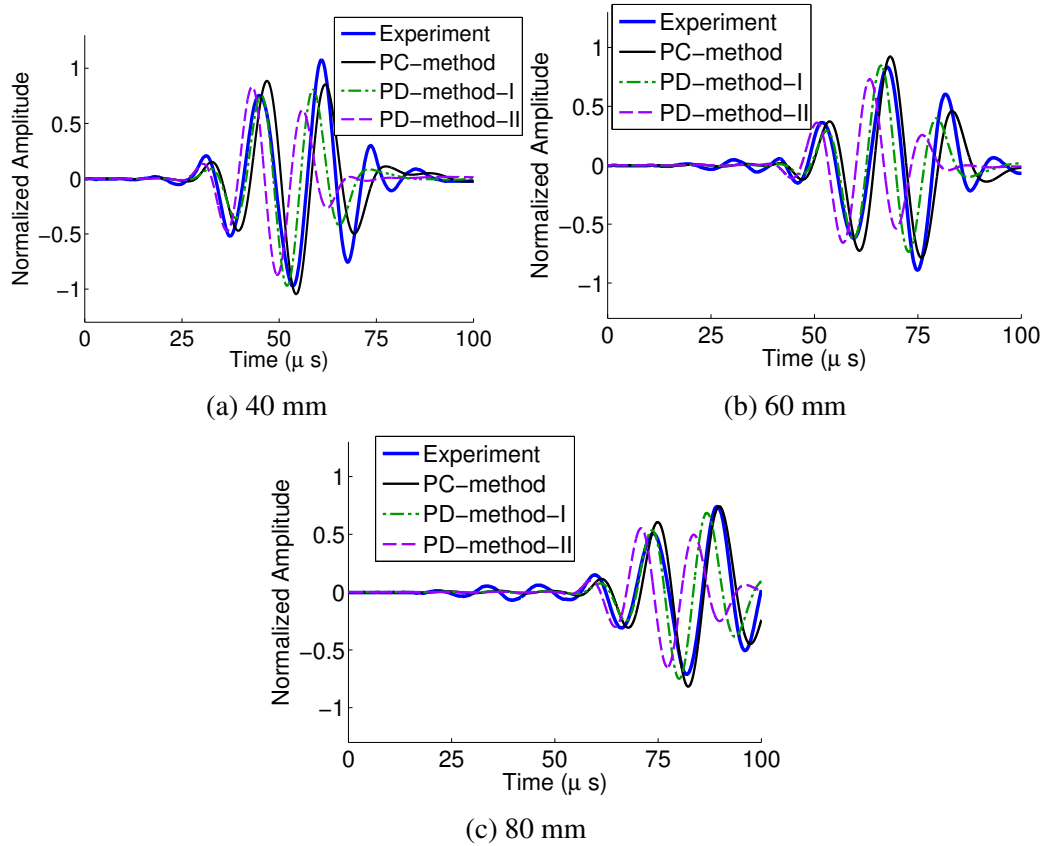


Figure 5.25: Comparison between experimental data and LISA simulations along the 90 deg azimuthal direction for various actuation methods.

Figure 5.25 shows the out-of-plane component of the displacement field for the experiment and LISA simulations. The displacements are compared along the azimuthal direction of 90 deg. As before, a fixed shift of $10 \mu s$ was applied to the experimental data. To capture the relative amplitude between the wave field along the 0 deg and 90 deg azimuthal directions, the signals are normalized by the same values chosen in Fig. 5.24. Similar trends are observed in the case of wave propagation comparisons along 90-deg azimuthal direction with good correlation between the experimental data and PC method. PD methods, on the other hand, show marked differences in the temporal behavior of the propagating wave. One key feature is that the amplitude in the experiments is lower than the values predicted by the PC method, which can be attributed to the material damping present in the

experiment and not currently modeled in UM-LISA.

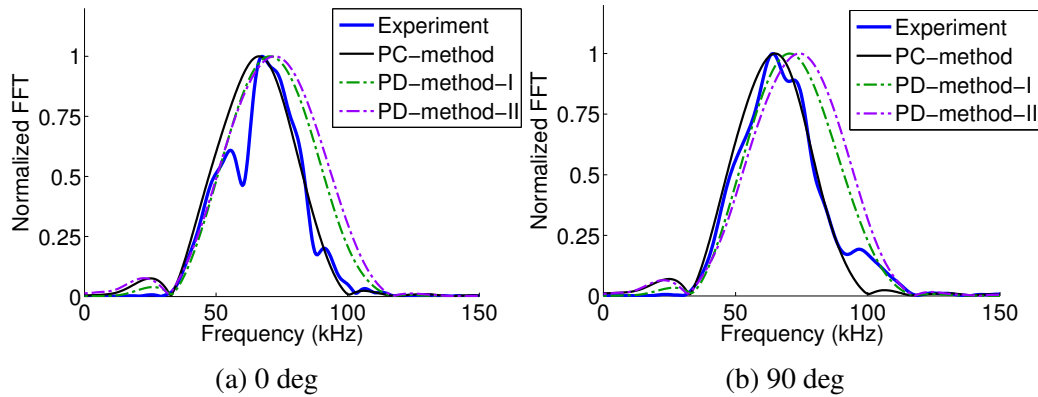


Figure 5.26: Comparison between FFT of the experimental data and LISA simulations at 40 mm from the center of the actuator along various azimuthal directions.

Figure 5.26 shows the Fast Fourier Transform of the out-of-plane component of the displacement for experimental data and LISA simulations. The FFT provides information about the frequency content of the propagating signal. From the figure, it is clear that PC method is able to predict the frequency content in the propagating wave field better than any of the PD methods.

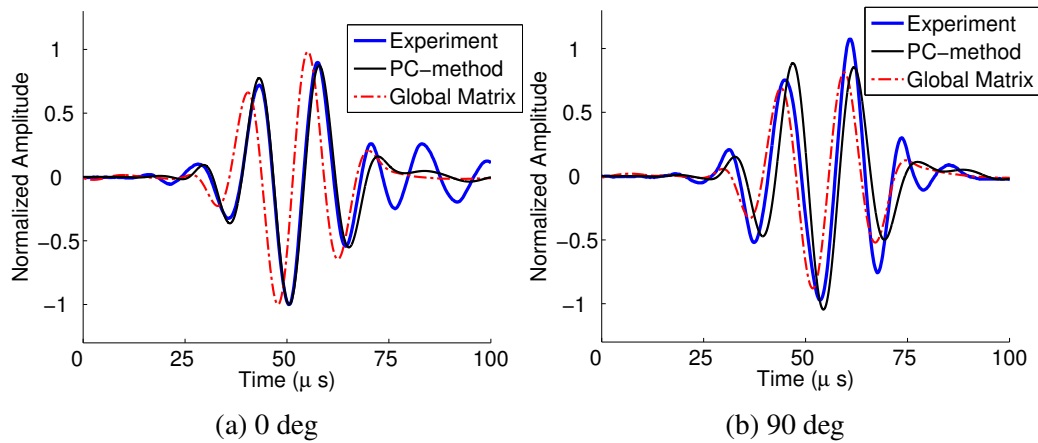


Figure 5.27: Comparison between the experimental data, UM-LISA (PC method) simulations and global matrix method for the out-of-plane displacement at 40 mm from the center of the actuator along 0 deg and 90 deg azimuthal direction.

To characterize the electromechanical coupling between the actuator and substrate, sim-

ulations were performed with the global matrix (GM) method [47, 136]. GM is a semi-analytical method for obtaining wave propagation in infinite layered media that uses surface shear tractions to represent actuation. Figure 5.27 shows the comparison of out-of-plane component of displacement between the experimental data, UM-LISA with the PC method and global matrix approach. One can see that there is a phase shift between the signals predicted by the GM approach and UM-LISA with the PC method. This shift in signal can be partly attributed to the inertial effects of the actuator. To isolate this phenomenon, simulations were carried out with UM-LISA (PC method) by significantly reducing the density of the piezoelectric material and, therefore, eliminating its inertial effects. The reduction density ratio of 100 ($\rho_{reduced} = 77.50 \text{ kg/m}^3$) was considered for the simulations to visualize the effect of mechanical coupling between the actuator and the substrate.

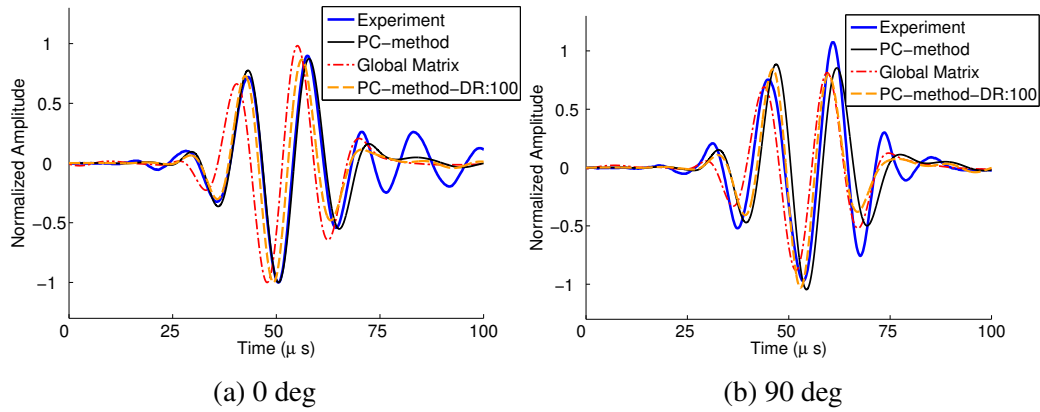


Figure 5.28: Effect of density reduction on UM-LISA simulation of GW.

Figure 5.28 shows the results for UM-LISA (PC method) with reduced actuator density. The results show that reducing the actuator density compensates for some of the phase shift observed in the case of GM, but not entirely. The additional shift might be a result of piezoelectric coupling between the actuator and the substrate.

5.4 Frequency Response for Piezoelectric Sensor

UM-LISA with PC method of actuation was used to revisit the sources of error encountered in validating the theoretical formulation developed by Raghavan and Cesnik [46]. The theoretical formulation was developed for finite-dimensional surface-bonded piezoelectric wafer actuators. Although the theoretical formulation showed good correlation between the experimental and theoretical results, there was a slight error observed in the prediction of peak frequency for thicker rectangular actuators.

The experimental set-up (shown in Fig. 5.29) used in the theoretical validation was a $600 \times 600 \times 3.1$ mm thick isotropic aluminum plate (Table. 5.1). It was instrumented with a pair of 0.3-mm thick PZT-5A rectangular piezo actuators of dimensions 25×5 mm at the center of the top and bottom surfaces. For the first experiment, the two actuators were actuated in-phase to generate the fundamental symmetric mode (S_o). For the second experiment, they were excited out-of-phase to generate the fundamental anti-symmetric mode (A_o). The input excitation for the actuators was a 3.5-cycle Hann-modulated toneburst over a range of center frequencies. The generated GW were monitored with a 10×10 mm PZT-5A sensor mounted at a location (35 mm, 35 mm) relative to the plate center as shown in Fig. 5.29. More details regarding the experiment can be found in Ref. [46].

The initial error in the theoretical formulation was attributed to a shear lag effect present in the experiment. In the theoretical formulation, the pin-force model proposed by Crawley and de Luis [123] was used for actuator modeling. The pin-force was developed for surface-bonded piezoelectric actuators on opposite beam surfaces and actuated quasi-statically. The approximation was valid for the cases where the shear lag parameter (Γ) approached infinity, that is,

$$\Gamma = \sqrt{\frac{a^2 G_b (1 + \nu_a)}{Y_a^{11} h_a h_b} \left(1 + \frac{\eta Y_a^{11} h_a}{Y_s h_s} \right)} \rightarrow \infty \quad (5.1)$$

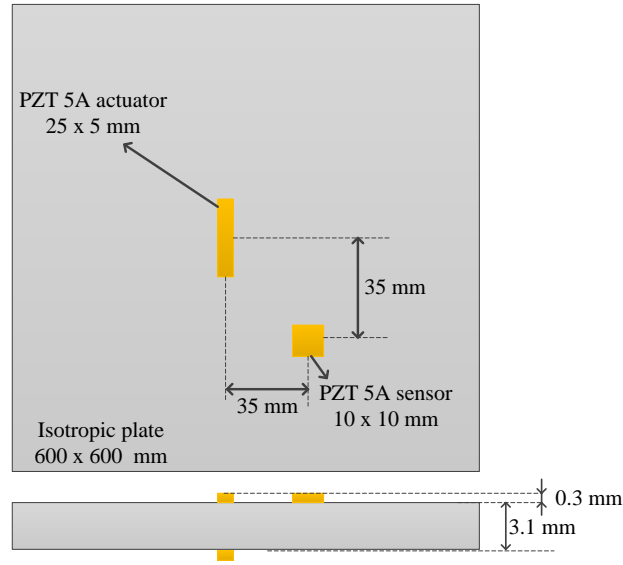


Figure 5.29: Schematic of the experiment of Raghavan and Cesnik [46].

where h_a , h_b and h_s are the thicknesses of actuator, bond layer and substrate, respectively. And, a , Y_a and ν_a are the dimension, Young's modulus and Poisson ratio of the actuator, respectively. Y_s is the substrate's Young's modulus and G_b is the shear modulus of the bond layer. η is a constant depending on the excitation phase of the dual actuators ($\eta = 2$ for symmetric excitation and $\eta = 6$ for antisymmetric excitation).

For smaller Γ resulting from the finite stiffness of the actuator relative to the plate and imperfect bonding between the actuator and substrate, the force transfer between the actuator and substrate occurs over a finite length close to the edge of the actuator. This was implemented in the theoretical formulation of Ref. [46] by reducing the physical dimensions of the actuator by 20%. The plots for the comparison between the experimental and theoretical sensor response are shown in Fig. 5.30. It was observed that the theoretical results with reduced dimensions agreed better with the experimental results.

The UM-LISA simulations were carried out for the experimental setup shown in Fig. 5.29.

The comparison between the experimental data, theoretical calculations and UM-LISA simulations are shown in Fig. 5.31. The plots show a good correlation between UM-LISA

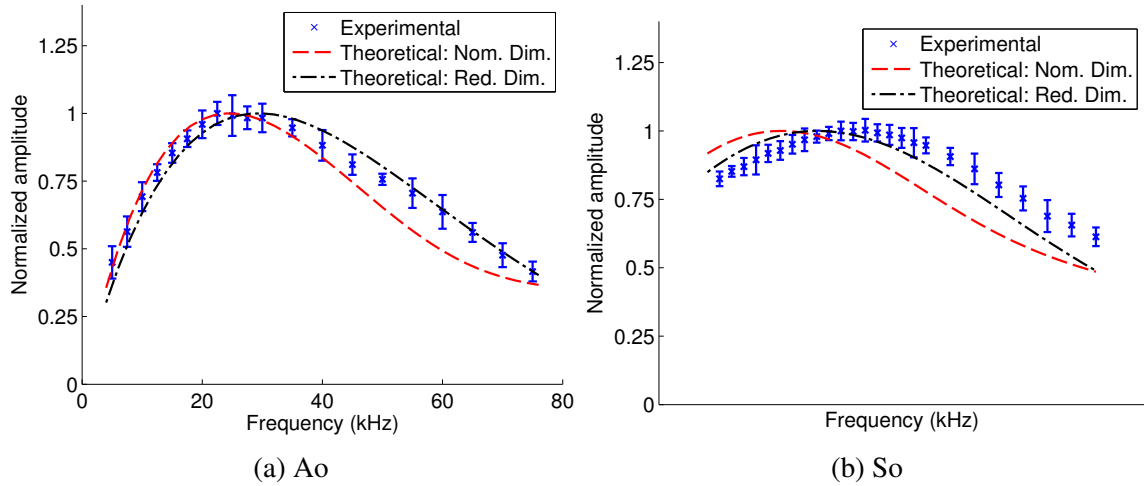


Figure 5.30: Comparison between experimental and theoretical sensor response amplitudes in the rectangular actuator experiment at different center frequencies for: (a) S_o mode and (b) A_o mode [46].

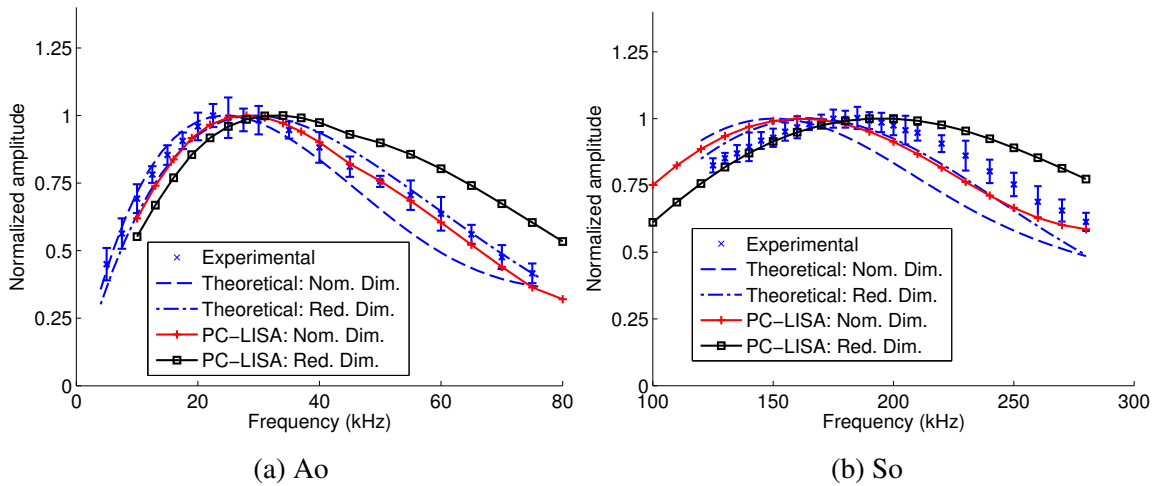


Figure 5.31: Comparison between experimental, theoretical and UM-LISA (PC method) sensor response amplitudes in the rectangular actuator experiment at different center frequencies for: (a) S_o mode and (b) A_o mode.

and the experimental data. The experimental results are encapsulated between the UM-LISA results for nominal dimensions and reduced dimensions. This was expected since perfect bonding between the actuator and substrate was considered. However, reducing the actuator dimensions by 20% is an overestimation. It can be said with confidence that reducing the actuator dimensions by a value less than 20 % will result in better agreement between the

UM-LISA simulations and experiments. One can see that the UM-LISA sensor response for the A_o mode at lower frequencies (10 - 30 kHz) tends to have reduced correlation with reduced dimensions. This discrepancy might be a result of large impedance mismatch between the actuator and substrate, whose effect might be predominant at lower frequencies.

CHAPTER 6

Concluding Remarks

This chapter first presents a summary of the main accomplishments in this dissertation. Key contributions are then presented based upon the results from the numerical analysis. Finally recommendations for future studies and improvements are suggested.

6.1 Summary

The main objective of this work was to develop a numerical framework to model the GW generation, propagation, and sensing in thin-walled structures. The literature survey revealed the need for an efficient and accurate modeling tool for the development of structural health monitoring architecture. The UM-LISA framework was developed in response to it.

Iterative equations form the core of the UM-LISA framework. They were derived from the electro-static/elasto-dynamic equilibrium equations by incorporating the constitutive relations and the compatibility conditions. Customary FD relations were used to resolve the spatial and temporal derivatives. Sharp interface model (SIM), a key feature of the formulation, distinguishes LISA from the traditional FD methods. SIM enforces the continuity of displacement and stress field, which enables the seamless transition of the propagating waves between the material interfaces.

Previous to this study, other researchers implementing the LISA formulation utilized predominantly an out-of-plane prescribed displacement as input excitation. In this work,

a better representation for actuator was proposed as an in-plane displacement input excitation. This also enabled the modeling of CLoVER and other MFC based transducers.

Although prescribed-displacement-actuation-based LISA formulation captured the essence of the GW propagation, it over-simplified the GW generation by not accounting for the electromechanical coupling between the piezoelectric transducer and the substrate. This dissertation addressed the shortcoming by extending the LISA's capability to model piezoelectric materials by including the electromechanical coupling in the governing equilibrium equations with appropriate constitutive and compatibility conditions. The final iterative equations calculate mechanical displacements in an explicit time-marching manner, whereas the electric potentials are calculated using an implicit scheme.

The architecture of the code was illustrated via detailed flow charts and block diagrams, highlighting different modules included in the UM-LISA code. The code was presented in a step-wise fashion to describe the structure of the setup and expedite future developments to the framework.

There are a vast number of parameters affecting the accuracy and stability of the numerical simulations. This dissertation addressed the ones that influence the GW generation and propagation characteristics. Studies were performed to determine the rate of convergence of the numerical method. As the GW are dispersive in nature, and the wave characteristics are dependent on frequency-thickness, several cases were considered in determining the convergence of the methodology. Suggestions regarding the optimal parameters while implementing UM-LISA for wave propagation were presented.

Numerical analyses were conducted on several thin-walled specimens: isotropic plates, composite laminates and a sandwich panel. GW propagation studies were carried out using uni-directional $[0]_{12T}$, cross-ply $[0/90]_{3S}$ and quasi-isotropic $[0/45/-45/90/90/-45/45/0]_S$ laminates. The laminates were manufactured in-house using a prepreg/autoclave procedure. The out-of-plane displacement was used as the reference parameter for the experimental comparison studies. Laser vibrometry experiments were used to measure the GW

propagation field, and the results were compared against the UM-LISA simulations. For the comparison studies, the GW were generated using piezo ceramic and CLoVER transducers. Preliminary experimental and numerical studies were conducted on a composite foam core sandwich panel to investigate the possibility of using GW for SHM-related applications.

Comparison studies between simulations and experiments indicate that UM-LISA simulations were able to capture the GW propagation in different composite laminates in non-principal reference axis. Important features such as energy steering and energy spreading were captured by the simulations. The new iterative equations were also able to successfully incorporate the effect of ply-angle rotation on stiffness matrix and will be able to model structures with complex material properties in varying reference axis. Also, the study showed UM-LISA's ability to model the directional characteristics of the CLoVER transducer. The sandwich panel studies indicated that lower frequencies of excitation are suitable for GW testing as more energy propagates to the bottom facesheet as compared to the higher frequencies.

A simulated damage study was performed on the quasi-isotropic laminate. The damage was introduced to the structure using a concentrated mass in the form of a steel bar. This particular "damage" was selected because of its mobility to different radial and azimuthal positions on the structure, and also to avoid any permanent damage to the laminate. A combination of circular piezo transducers and CLoVER transducers were used in the simulations. Good correlation was observed between the simulated results and the experimental data, based on consistent higher amplitudes observed in the sectors aligned to the damage site. The CLoVER transducer was effective in identifying the azimuthal location of the simulated damage and rejecting transverse signals coming to it (filtering effect).

Studies were also carried out to investigate the difference between different actuation methods to generate GW in UM-LISA. While two of the methods are indirect representation of the actuator effects through prescribed displacement, the third one is a direct representation of the electromechanical coupled effects of the piezo actuator by the piezo-

coupled implementation. The advantages of using a piezo-coupled formulation was illustrated by monitoring actuator nodes. Comparisons with the laser vibrometry experiments validated the improvements in the GW generation using piezo-coupled actuation. Finally, frequency response studies were carried out for piezoelectric sensors in an isotropic plate and compared with experimental data. Better correlation was observed between the experiments and simulation data as the piezo-coupled solution within UM-LISA incorporated the electromechanical coupling between the transducer and the substrate.

6.2 Key Contributions

The key contributions of this dissertation are summarized as follows.

- I Creation of UM-LISA framework as an effective way to model GW propagation, simulation and damage interaction in thin-walled composite structures. Incorporating the effects of ply-angle rotation on stiffness matrix in the UM-LISA framework, which enables the modeling of structures with complex material properties in varying reference axis.
- II Development of a unified UM-LISA framework to model piezo-coupled transducers for GW generation and sensing, by accounting for the electromechanical coupling between the piezo transducers and the substrate.
- III Validation of the new formulation against various metallic and composite laminate experiments, showing that it is capable of accurately capturing the wave generation and propagation, as well as the energy steering effects of anisotropic substrates.
- IV Systematic development of discretization parameter guidelines to obtain convergent and accurate guided-wave generation and propagation solutions in composite structures.

- V Demonstration that piezoelectric-coupled LISA formulation best captures the induced piezoelectric actuator effects when generating guided waves, and that the prescribed displacement approaches may introduce significant error to this process.

6.3 Recommendations for Future Work

Since the development of efficient and accurate numerical tools for GW propagation is an ongoing process, several areas have been identified for future studies based on the research conducted in this thesis:

- I Damage interaction: A preliminary damage interaction study was performed as part of this dissertation. The framework can be used to model delaminations and low velocity impacts, which tend to be critical in composite thin-walled structures. The framework can be utilized to build a database of GW interaction with damage features to enable damage identification and characterization for SHM systems.
- II Advanced parallelization: The current study implements an OPENMP based parallelization, which utilized the number of physical cores in a processor. Based on the structure of the numerical framework, employing GPU computing will be beneficial in increasing the performance and reducing the computational time.
- III Hybrid formulation: To leverage the advantages of other methods for wave propagation, like FE methods and semi-analytical methods, development of a hybrid LISA formulation should be pursued to obtain more flexibility in modeling capability.
- IV Coupled 2D and 3D LISA: In certain scenarios a 2D LISA formulation would be more appropriate for GW simulation, such as narrow waveguides and honey comb cores. A coupled 2D-3D LISA framework would be extremely useful in modeling sandwich and complex structures. This could be obtained by developing transitional elements from a 2D to a 3D structure.

- V Damping: In the current formulation, material damping effects were not included in the numerical formulation. This would be an important addition to obtain better correlation with experimental data for wave propagation and damage interaction studies.
- VI Grid transformation: The current UM-LISA framework utilizes cuboid grids in the numerical implementation. Although the current formulation is capable of modeling engineering structures and transducers, extending the UM-LISA to incorporate grid transformations will be beneficial in modeling curved panels and complex features.
- VII Higher-order formulation: Although the current UM-LISA framework is close to a second-order convergence rate, developing a higher-order formulation will provide more accurate results in high impedance variation scenarios. The higher-order formulation can also be used to capture non-linear wave propagation features.

APPENDIX

Details of UM-LISA Derivation

Steps involved between setting up the governing equations (Eq. 2.24), and deriving the final iterative equations (Eqs. 2.29-2.32) are presented in this section. The stress and electric displacement continuity relations given in Eq. 2.28 are used along with customary finite difference transformations listed in Eqs. 2.9-2.11 and Eqs. 2.25-2.27.

Detailed derivation is provided for w_1 and the remaining displacement components (w_2, w_3) and induced potential (ψ) can be obtained in a similar fashion. To obtain the iterative equations for w_1 , first the coupled elastodynamic equations are considered for the eight points as shown in Fig. 2.5(a). For brevity, the superscript index terms (i, j, k) indicating a general node in space are dropped, but will be presented in the final equations for completeness. The coupled elastodynamic equations are multiplied by $\Delta x_1^\alpha \Delta x_2^\beta \Delta x_3^\gamma$ with appropriate choice of $(\alpha, \beta, \gamma) = \pm 1$, given as:

$$\Delta x_1^{+1} \Delta x_2^{+1} \Delta x_3^{+1} \left(S_{V(1l)V(mn)}^{+\delta,+\delta,+\delta} w_{m,nl}^{+\delta,+\delta,+\delta} + e_{V(1l)m}^{+\delta,+\delta,+\delta} \psi_{,ml}^{+\delta,+\delta,+\delta} = \rho^{+\delta,+\delta,+\delta} \ddot{w}_1^{+\delta,+\delta,+\delta} \right) \quad (1)$$

$$\Delta x_1^{-1} \Delta x_2^{+1} \Delta x_3^{+1} \left(S_{V(1l)V(mn)}^{-\delta,+\delta,+\delta} w_{m,nl}^{-\delta,+\delta,+\delta} + e_{V(1l)m}^{-\delta,+\delta,+\delta} \psi_{,ml}^{-\delta,+\delta,+\delta} = \rho^{-\delta,+\delta,+\delta} \ddot{w}_1^{-\delta,+\delta,+\delta} \right) \quad (2)$$

$$\Delta x_1^{+1} \Delta x_2^{-1} \Delta x_3^{+1} \left(S_{V(1l)V(mn)}^{+\delta,-\delta,+\delta} w_{m,nl}^{+\delta,-\delta,+\delta} + e_{V(1l)m}^{+\delta,-\delta,+\delta} \psi_{,ml}^{+\delta,-\delta,+\delta} = \rho^{+\delta,-\delta,+\delta} \ddot{w}_1^{+\delta,-\delta,+\delta} \right) \quad (3)$$

$$\Delta x_1^{+1} \Delta x_2^{+1} \Delta x_3^{-1} \left(S_{V(1l)V(mn)}^{+\delta,+\delta,-\delta} w_{m,nl}^{+\delta,+\delta,-\delta} + e_{V(1l)m}^{+\delta,+\delta,-\delta} \psi_{,ml}^{+\delta,+\delta,-\delta} = \rho^{+\delta,+\delta,-\delta} \ddot{w}_1^{+\delta,+\delta,-\delta} \right) \quad (4)$$

$$\Delta x_1^{+1} \Delta x_2^{-1} \Delta x_3^{-1} \left(S_{V(1l)V(mn)}^{+\delta,-\delta,-\delta} w_{m,nl}^{+\delta,-\delta,-\delta} + e_{V(1l)m}^{+\delta,-\delta,-\delta} \psi_{,ml}^{+\delta,-\delta,-\delta} = \rho^{+\delta,-\delta,-\delta} \ddot{w}_1^{+\delta,-\delta,-\delta} \right) \quad (5)$$

$$\Delta x_1^{-1} \Delta x_2^{+1} \Delta x_3^{-1} \left(S_{V(1l)V(mn)}^{-\delta,+\delta,-\delta} w_{m,nl}^{-\delta,+\delta,-\delta} + e_{V(1l)m}^{-\delta,+\delta,-\delta} \psi_{,ml}^{-\delta,+\delta,-\delta} = \rho^{-\delta,+\delta,-\delta} \ddot{w}_1^{-\delta,+\delta,-\delta} \right) \quad (6)$$

$$\Delta x_1^{-1} \Delta x_2^{-1} \Delta x_3^{+1} \left(S_{V(1l)V(mn)}^{-\delta,-\delta,+\delta} w_{m,nl}^{-\delta,-\delta,+\delta} + e_{V(1l)m}^{-\delta,-\delta,+\delta} \psi_{,ml}^{-\delta,-\delta,+\delta} = \rho^{-\delta,-\delta,+\delta} \ddot{w}_1^{-\delta,-\delta,+\delta} \right) \quad (7)$$

$$\Delta x_1^{-1} \Delta x_2^{-1} \Delta x_3^{-1} \left(S_{V(1l)V(mn)}^{-\delta,-\delta,-\delta} w_{m,nl}^{-\delta,-\delta,-\delta} + e_{V(1l)m}^{-\delta,-\delta,-\delta} \psi_{,ml}^{-\delta,-\delta,-\delta} = \rho^{-\delta,-\delta,-\delta} \ddot{w}_1^{-\delta,-\delta,-\delta} \right) \quad (8)$$

To employ sharp interface model (SIM) for the continuity of mechanical displacements for the entire numerical model, prescribed displacement field is used for the first two time steps, and for the subsequent time steps the acceleration (\ddot{w}_1) is enforced to be the same at the eight additional points shown in Fig. 2.5(a), represented as:

$$\ddot{w}_1^{\alpha\delta,\beta\delta,\gamma\delta} = \ddot{w}_1 \quad \alpha, \beta, \gamma = \pm 1 \quad (9)$$

In addition to the spatial derivatives, the temporal derivatives in Eqs. .1-8 can be re-solved as:

$$\ddot{w}_1^t = \frac{w_1^{t+1} - 2w_1^t + w_1^{t-1}}{2\Delta t^2} \quad (10)$$

where Δt is the time step used in the simulation, and superscript represents the temporal iterative step in the equations. Next, the SIM for the continuity of stress is implemented by considering additional points shown as black squares in Fig. 2.5(b). The selective stress continuity equations are multiplied by appropriate $\Delta x_i \Delta x_j$ ($(i, j) = \pm 1$) terms, given by:

$$-2\Delta x_2^{+1} \Delta x_3^{+1} \left(\tau_{11}^{+\varepsilon,+\delta,+\delta} - \tau_{11}^{-\varepsilon,+\delta,+\delta} = 0 \right) \quad (11)$$

$$-2\Delta x_2^{+1}\Delta x_3^{-1}\left(\tau_{11}^{+\varepsilon,+\delta,-\delta}-\tau_{11}^{-\varepsilon,+\delta,-\delta}=0\right) \quad (.12)$$

$$-2\Delta x_2^{-1}\Delta x_3^{+1}\left(\tau_{11}^{+\varepsilon,-\delta,+\delta}-\tau_{11}^{-\varepsilon,-\delta,+\delta}=0\right) \quad (.13)$$

$$-2\Delta x_2^{-1}\Delta x_3^{-1}\left(\tau_{11}^{+\varepsilon,-\delta,-\delta}-\tau_{11}^{-\varepsilon,-\delta,-\delta}=0\right) \quad (.14)$$

$$-2\Delta x_1^{+1}\Delta x_3^{+1}\left(\tau_{12}^{+\delta,+\varepsilon,+\delta}-\tau_{12}^{+\delta,-\varepsilon,+\delta}=0\right) \quad (.15)$$

$$-2\Delta x_1^{-1}\Delta x_3^{+1}\left(\tau_{12}^{-\delta,+\varepsilon,+\delta}-\tau_{12}^{-\delta,-\varepsilon,+\delta}=0\right) \quad (.16)$$

$$-2\Delta x_1^{+1}\Delta x_3^{-1}\left(\tau_{12}^{+\delta,+\varepsilon,-\delta}-\tau_{12}^{+\delta,-\varepsilon,-\delta}=0\right) \quad (.17)$$

$$-2\Delta x_1^{-1}\Delta x_3^{-1}\left(\tau_{12}^{-\delta,+\varepsilon,-\delta}-\tau_{12}^{-\delta,-\varepsilon,-\delta}=0\right) \quad (.18)$$

$$-2\Delta x_1^{+1}\Delta x_2^{+1}\left(\tau_{13}^{+\delta,+\delta,+\varepsilon}-\tau_{13}^{+\delta,+\delta,-\varepsilon}=0\right) \quad (.19)$$

$$-2\Delta x_1^{+1}\Delta x_2^{-1}\left(\tau_{13}^{+\delta,-\delta,+\varepsilon}-\tau_{13}^{+\delta,-\delta,-\varepsilon}=0\right) \quad (.20)$$

$$-2\Delta x_1^{-1}\Delta x_2^{+1}\left(\tau_{13}^{-\delta,+\delta,+\varepsilon}-\tau_{13}^{-\delta,+\delta,-\varepsilon}=0\right) \quad (.21)$$

$$-2\Delta x_1^{-1}\Delta x_2^{-1}\left(\tau_{13}^{-\delta,-\delta,+\varepsilon}-\tau_{13}^{-\delta,-\delta,-\varepsilon}=0\right) \quad (.22)$$

The expressions for stress tensor terms in Eqs. .11-.22 are obtained from Eq. 2.20. The customary finite difference transformations (Eqs. 2.9-2.11) are used to resolve the spatial derivatives in Eqs. .1-.8 and Eqs. .11-.22. Next, the modified governing equations in Eqs. .1-.8 are added to the stress continuity equations Eqs. .11-.22 and re-arranged to obtain the displacement field w_1 , given as:

$$\begin{aligned}
w_1^{i,j,k,t+1} &= -w_1^{i,j,k,t-1} + 2w_1^{i,j,k} \\
&- \frac{\bar{\chi}}{4} w_1^{i,j,k} \sum_{\alpha,\beta,\gamma=\pm 1} \left[\frac{\Delta x_2^\beta \Delta x_3^\gamma}{\Delta x_1^\alpha} \tilde{S}_{11} + \frac{\Delta x_1^\alpha \Delta x_3^\gamma}{\Delta x_2^\beta} \tilde{S}_{66} + \frac{\Delta x_1^\alpha \Delta x_2^\beta}{\Delta x_3^\gamma} \tilde{S}_{55} \right] \\
&+ \frac{\bar{\chi}}{4} \sum_{\alpha,\beta,\gamma=\pm 1} \left[\Delta x_1^\alpha \Delta x_2^\beta \Delta x_3^\gamma \left(\frac{\tilde{S}_{11} w_1^{i+\alpha,j,k}}{(\Delta x_1^\alpha)^2} + \frac{\tilde{S}_{66} w_1^{i,j+\beta,k}}{(\Delta x_2^\beta)^2} + \frac{\tilde{S}_{55} w_1^{i,j,k+\gamma}}{(\Delta x_3^\gamma)^2} \right) \right] \\
&+ \frac{\bar{\chi}}{8} \sum_{\alpha,\beta,\gamma=\pm 1} \left[\alpha\beta \Delta x_3^\gamma (\tilde{S}_{12} + \tilde{S}_{66}) (w_2^{i+\alpha,j+\beta,k} - w_2^{i,j,k}) \right] \\
&+ \frac{\bar{\chi}}{8} \sum_{\alpha,\beta,\gamma=\pm 1} \left[\alpha\beta \Delta x_3^\gamma (\tilde{S}_{12} - \tilde{S}_{66}) (w_2^{i,j+\beta,k} - w_2^{i+\alpha,j,k}) \right] \\
&+ \frac{\bar{\chi}}{8} \sum_{\alpha,\beta,\gamma=\pm 1} \left[\alpha\gamma \Delta x_2^\beta (\tilde{S}_{13} + \tilde{S}_{55}) (w_3^{i+\alpha,j,k+\gamma} - w_3^{i,j,k}) \right] \\
&+ \frac{\bar{\chi}}{8} \sum_{\alpha,\beta,\gamma=\pm 1} \left[\alpha\gamma \Delta x_2^\beta (\tilde{S}_{13} - \tilde{S}_{55}) (w_3^{i,j,k+\gamma} - w_3^{i+\alpha,j,k}) \right] \\
&- \frac{\bar{\chi}}{4} \sum_{\alpha,\beta,\gamma=\pm 1} \left[\alpha\beta \Delta x_3^\gamma \tilde{S}_{16} (w_1^{i,j,k} - w_1^{i+\alpha,j+\beta,k}) \right] \\
&- \frac{\bar{\chi}}{4} w_2^{i,j,k} \sum_{\alpha,\beta,\gamma=\pm 1} \left[\frac{\Delta x_2^\beta \Delta x_3^\gamma}{\Delta x_1^\alpha} \tilde{S}_{16} + \frac{\Delta x_1^\alpha \Delta x_3^\gamma}{\Delta x_2^\beta} \tilde{S}_{26} \right] \\
&- \frac{\bar{\chi}}{8} \sum_{\alpha,\beta,\gamma=\pm 1} \left[\beta\gamma \Delta x_1^\alpha (\tilde{S}_{36} + \tilde{S}_{45}) w_3^{i,j,k} \right] \\
&+ \frac{\bar{\chi}}{4} \sum_{\alpha,\beta,\gamma=\pm 1} \left[\frac{\Delta x_2^\beta \Delta x_3^\gamma}{\Delta x_1^\alpha} \tilde{S}_{16} w_2^{i+\alpha,j,k} + \frac{\Delta x_1^\alpha \Delta x_3^\gamma}{\Delta x_2^\beta} \tilde{S}_{26} w_2^{i,j+\beta,k} \right] \\
&+ \frac{\bar{\chi}}{8} \sum_{\alpha,\beta,\gamma=\pm 1} \left[\beta\gamma \Delta x_1^\alpha \tilde{S}_{36} (w_3^{i,j+\beta,k+\gamma} + w_3^{i,j,k+\gamma} - w_3^{i,j+\beta,k}) \right] \\
&+ \frac{\bar{\chi}}{8} \sum_{\alpha,\beta,\gamma=\pm 1} \left[\beta\gamma \Delta x_1^\alpha \tilde{S}_{45} (w_3^{i,j+\beta,k+\gamma} - w_3^{i,j,k+\gamma} + w_3^{i,j+\beta,k}) \right] \\
&+ \frac{\bar{\chi}}{4} \sum_{\alpha,\beta,\gamma=\pm 1} \left[\frac{\Delta x_1^\alpha \Delta x_2^\beta}{\Delta x_3^\gamma} \tilde{S}_{45} (w_2^{i,j,k+\gamma} - w_2^{i,j,k}) \right] \\
&+ \frac{\bar{\chi}}{8} \sum_{\alpha,\beta,\gamma=\pm 1} \left[\alpha\gamma \Delta x_2^\beta (\tilde{e}_{15} + \tilde{e}_{31}) (\psi^{i+\alpha,j,k+\gamma} - \psi^{i,j,k}) \right] \\
&- \frac{\bar{\chi}}{8} \sum_{\alpha,\beta,\gamma=\pm 1} \left[\alpha\gamma \Delta x_2^\beta (\tilde{e}_{15} - \tilde{e}_{31}) (\psi^{i,j,k+\gamma} - \psi^{i+\alpha,j,k}) \right]
\end{aligned} \tag{23}$$

Similarly the other mechanical displacement components can be written as:

$$\begin{aligned}
w_2^{i,j,k,t+1} &= -w_2^{i,j,k,t-1} + 2w_2^{i,j,k} \\
&- \frac{\bar{\chi}}{4} w_2^{i,j,k} \sum_{\alpha,\beta,\gamma=\pm 1} \left[\frac{\Delta x_2^\beta \Delta x_3^\gamma}{\Delta x_1^\alpha} \tilde{S}_{66} + \frac{\Delta x_1^\alpha \Delta x_3^\gamma}{\Delta x_2^\beta} \tilde{S}_{22} + \frac{\Delta x_1^\alpha \Delta x_2^\beta}{\Delta x_3^\gamma} \tilde{S}_{44} \right] \\
&+ \frac{\bar{\chi}}{4} \sum_{\alpha,\beta,\gamma=\pm 1} \left[\Delta x_1^\alpha \Delta x_2^\beta \Delta x_3^\gamma \left(\frac{\tilde{S}_{66} w_2^{i+\alpha,j,k}}{(\Delta x_1^\alpha)^2} + \frac{\tilde{S}_{22} w_2^{i,j+\beta,k}}{(\Delta x_2^\beta)^2} + \frac{\tilde{S}_{44} w_2^{i,j,k+\gamma}}{(\Delta x_3^\gamma)^2} \right) \right] \\
&+ \frac{\bar{\chi}}{8} \sum_{\alpha,\beta,\gamma=\pm 1} \left[\alpha\beta \Delta x_3^\gamma (\tilde{S}_{12} + \tilde{S}_{66}) (w_1^{i+\alpha,j+\beta,k} - w_1^{i,j,k}) \right] \\
&+ \frac{\bar{\chi}}{8} \sum_{\alpha,\beta,\gamma=\pm 1} \left[\alpha\beta \Delta x_3^\gamma (\tilde{S}_{12} - \tilde{S}_{66}) (w_1^{i+\alpha,j,k} - w_1^{i,j+\beta,k}) \right] \\
&+ \frac{\bar{\chi}}{8} \sum_{\alpha,\beta,\gamma=\pm 1} \left[\beta\gamma \Delta x_1^\alpha (\tilde{S}_{23} + \tilde{S}_{44}) (w_3^{i,j+\beta,k+\gamma} - w_3^{i,j,k}) \right] \\
&+ \frac{\bar{\chi}}{8} \sum_{\alpha,\beta,\gamma=\pm 1} \left[\beta\gamma \Delta x_1^\alpha (\tilde{S}_{23} - \tilde{S}_{44}) (w_3^{i,j,k+\gamma} - w_3^{i,j+\beta,k}) \right] \\
&- \frac{\bar{\chi}}{4} \sum_{\alpha,\beta,\gamma=\pm 1} \left[\alpha\beta \Delta x_3^\gamma \tilde{S}_{26} (w_2^{i,j,k} - w_2^{i+\alpha,j+\beta,k}) \right] \\
&- \frac{\bar{\chi}}{4} w_1^{i,j,k} \sum_{\alpha,\beta,\gamma=\pm 1} \left[\frac{\Delta x_2^\beta \Delta x_3^\gamma}{\Delta x_1^\alpha} \tilde{S}_{16} + \frac{\Delta x_1^\alpha \Delta x_3^\gamma}{\Delta x_2^\beta} \tilde{S}_{26} \right] \\
&+ \frac{\bar{\chi}}{4} \sum_{\alpha,\beta,\gamma=\pm 1} \left[\frac{\Delta x_2^\beta \Delta x_3^\gamma}{\Delta x_1^\alpha} \tilde{S}_{16} w_1^{i+\alpha,j,k} + \frac{\Delta x_1^\alpha \Delta x_3^\gamma}{\Delta x_2^\beta} \tilde{S}_{26} w_1^{i,j+\beta,k} \right] \\
&- \frac{\bar{\chi}}{8} \sum_{\alpha,\beta,\gamma=\pm 1} \left[\alpha\gamma \Delta x_2^\beta (\tilde{S}_{36} + \tilde{S}_{45}) w_3^{i,j,k} \right] \\
&+ \frac{\bar{\chi}}{8} \sum_{\alpha,\beta,\gamma=\pm 1} \left[\alpha\gamma \Delta x_2^\beta \tilde{S}_{36} (w_3^{i+\alpha,j,k+\gamma} + w_3^{i,j,k+\gamma} - w_3^{i+\alpha,j,k}) \right] \\
&+ \frac{\bar{\chi}}{8} \sum_{\alpha,\beta,\gamma=\pm 1} \left[\alpha\gamma \Delta x_2^\beta \tilde{S}_{45} (w_3^{i+\alpha,j,k+\gamma} - w_3^{i,j,k+\gamma} + w_3^{i+\alpha,j,k}) \right] \\
&+ \frac{\bar{\chi}}{4} \sum_{\alpha,\beta,\gamma=\pm 1} \left[\frac{\Delta x_1^\alpha \Delta x_2^\beta}{\Delta x_3^\gamma} \tilde{S}_{45} (w_1^{i,j,k+\gamma} - w_1^{i,j,k}) \right] \\
&+ \frac{\bar{\chi}}{8} \sum_{\alpha,\beta,\gamma=\pm 1} \left[\beta\gamma \Delta x_1^\alpha (\tilde{e}_{24} + \tilde{e}_{32}) (\psi^{i,j+\beta,k+\gamma} - \psi^{i,j,k}) \right] \\
&- \frac{\bar{\chi}}{8} \sum_{\alpha,\beta,\gamma=\pm 1} \left[\beta\gamma \Delta x_1^\alpha (\tilde{e}_{24} - \tilde{e}_{32}) (\psi^{i,j,k+\gamma} - \psi^{i,j+\beta,k}) \right]
\end{aligned} \tag{24}$$

$$\begin{aligned}
w_3^{i,j,k,t+1} &= -w_3^{i,j,k,t-1} + 2w_3^{i,j,k} \\
&- \frac{\bar{\chi}}{4} w_3^{i,j,k} \sum_{\alpha,\beta,\gamma=\pm 1} \left[\frac{\Delta x_2^\beta \Delta x_3^\gamma}{\Delta x_1^\alpha} \tilde{S}_{55} + \frac{\Delta x_1^\alpha \Delta x_3^\gamma}{\Delta x_2^\beta} \tilde{S}_{44} + \frac{\Delta x_1^\alpha \Delta x_2^\beta}{\Delta x_3^\gamma} \tilde{S}_{33} \right] \\
&+ \frac{\bar{\chi}}{4} \sum_{\alpha,\beta,\gamma=\pm 1} \left[\Delta x_1^\alpha \Delta x_2^\beta \Delta x_3^\gamma \left(\frac{\tilde{S}_{55} w_3^{i+\alpha,j,k}}{(\Delta x_1^\alpha)^2} + \frac{\tilde{S}_{44} w_3^{i,j+\beta,k}}{(\Delta x_2^\beta)^2} + \frac{\tilde{S}_{33} w_3^{i,j,k+\gamma}}{(\Delta x_3^\gamma)^2} \right) \right] \\
&+ \frac{\bar{\chi}}{8} \sum_{\alpha,\beta,\gamma=\pm 1} \left[\beta \gamma \Delta x_1^\alpha (\tilde{S}_{23} + \tilde{S}_{44}) (w_2^{i,j+\beta,k+\gamma} - w_2^{i,j,k}) \right] \\
&+ \frac{\bar{\chi}}{8} \sum_{\alpha,\beta,\gamma=\pm 1} \left[\beta \gamma \Delta x_1^\alpha (\tilde{S}_{23} - \tilde{S}_{44}) (w_2^{i,j+\beta,k} - w_2^{i,j,k+\gamma}) \right] \\
&+ \frac{\bar{\chi}}{8} \sum_{\alpha,\beta,\gamma=\pm 1} \left[\alpha \gamma \Delta x_2^\beta (\tilde{S}_{13} + \tilde{S}_{55}) (w_1^{i+\alpha,j,k+\gamma} - w_1^{i,j,k}) \right] \\
&+ \frac{\bar{\chi}}{8} \sum_{\alpha,\beta,\gamma=\pm 1} \left[\alpha \gamma \Delta x_2^\beta (\tilde{S}_{13} - \tilde{S}_{55}) (w_1^{i+\alpha,j,k} - w_1^{i,j,k+\gamma}) \right] \\
&- \frac{\bar{\chi}}{8} \sum_{\alpha,\beta,\gamma=\pm 1} \left[\beta \gamma \Delta x_1^\alpha (\tilde{S}_{36} + \tilde{S}_{45}) (w_1^{i,j,k} - w_1^{i,j+\beta,k+\gamma}) \right] \\
&- \frac{\bar{\chi}}{8} \sum_{\alpha,\beta,\gamma=\pm 1} \left[\alpha \gamma \Delta x_2^\beta (\tilde{S}_{36} + \tilde{S}_{45}) (w_2^{i,j,k} - w_2^{i+\alpha,j,k+\gamma}) \right] \\
&- \frac{\bar{\chi}}{8} \sum_{\alpha,\beta,\gamma=\pm 1} \left[\beta \gamma \Delta x_1^\alpha (\tilde{S}_{36} - \tilde{S}_{45}) (w_1^{i,j,k+\gamma} - w_1^{i,j+\beta,k}) \right] \\
&- \frac{\bar{\chi}}{8} \sum_{\alpha,\beta,\gamma=\pm 1} \left[\alpha \gamma \Delta x_2^\beta (\tilde{S}_{36} - \tilde{S}_{45}) (w_2^{i,j,k+\gamma} - w_2^{i+\alpha,j,k}) \right] \\
&+ \frac{\bar{\chi}}{4} \sum_{\alpha,\beta,\gamma=\pm 1} \left[\alpha \beta \Delta x_3^\gamma \tilde{S}_{45} (w_3^{i+\alpha,j+\beta,k} - w_3^{i,j,k}) \right] \\
&- \frac{\bar{\chi}}{4} \sum_{\alpha,\beta,\gamma=\pm 1} \left[\left(\frac{\Delta x_2^\beta \Delta x_3^\gamma}{\Delta x_1^\alpha} \tilde{e}_{15} + \frac{\Delta x_1^\alpha \Delta x_3^\gamma}{\Delta x_2^\beta} \tilde{e}_{24} + \frac{\Delta x_1^\alpha \Delta x_2^\beta}{\Delta x_3^\gamma} \tilde{e}_{33} \right) \psi^{i,j,k} \right] \\
&+ \frac{\bar{\chi}}{4} \sum_{\alpha,\beta,\gamma=\pm 1} \left[\Delta x_1^\alpha \Delta x_2^\beta \Delta x_3^\gamma \left(\frac{\tilde{e}_{15} \psi^{i+\alpha,j,k}}{(\Delta x_1^\alpha)^2} + \frac{\tilde{e}_{24} \psi^{i,j+\beta,k}}{(\Delta x_2^\beta)^2} + \frac{\tilde{e}_{33} \psi^{i,j,k+\gamma}}{(\Delta x_3^\gamma)^2} \right) \right]
\end{aligned} \tag{25}$$

where current time t is assumed where it is not mentioned, $\tilde{e}_{15} = e_{15}(i + \alpha, j + \beta, k + \gamma)$ represents piezoelectric stress material property for one of the eight cells surrounding point C depending on the choice of (α, β, γ) from $(+1, -1)$ and similar expressions hold for other

mechanical stiffness, piezoelectric stress matrix and permittivity terms. Also, $\bar{\chi} = \frac{\Delta t^2}{\bar{\rho}}$ where, $\bar{\rho} = \frac{1}{8} \sum_{\alpha,\beta,\gamma=\pm 1} \left(\Delta x_1^\alpha \Delta x_2^\beta \Delta x_3^\gamma \rho^{\alpha,\beta,\gamma} \right)$.

The implicit relation to calculate the induced potentials is obtained by substituting the elastodynamic equilibrium equations with the charge equations for electrostatics, and stress continuity with electric displacement continuity, and following the derivation steps listed above for w_1 . The implicit equation to calculate induced potentials is represented as:

$$F(\psi) = g(w_1, w_2, w_3) \quad (26)$$

where $F(\psi)$ and $g(w_1, w_2, w_3)$ are functions defined as:

$$\begin{aligned} F(\psi) = & -2 \sum_{\alpha,\beta,\gamma=\pm 1} \left[\left(\frac{\Delta x_2^\beta \Delta x_3^\gamma}{\Delta x_1^\alpha} \tilde{\kappa}_{11} + \frac{\Delta x_1^\alpha \Delta x_3^\gamma}{\Delta x_2^\beta} \tilde{\kappa}_{22} + \frac{\Delta x_1^\alpha \Delta x_2^\beta}{\Delta x_3^\gamma} \tilde{\kappa}_{33} \right) \psi^{i,j,k} \right] \\ & + 2 \sum_{\alpha,\beta,\gamma=\pm 1} \left[\Delta x_1^\alpha \Delta x_2^\beta \Delta x_3^\gamma \left(\frac{\tilde{\kappa}_{11} \psi^{i+\alpha,j,k}}{(\Delta x_1^\alpha)^2} + \frac{\tilde{\kappa}_{22} \psi^{i,j+\beta,k}}{(\Delta x_2^\beta)^2} + \frac{\tilde{\kappa}_{33} \psi^{i,j,k+\gamma}}{(\Delta x_3^\gamma)^2} \right) \right] \\ g(w_1, w_2, w_3) = & - \sum_{\alpha,\beta,\gamma=\pm 1} \left[\alpha \gamma \eta_x \eta_z (\tilde{e}_{15} + \tilde{e}_{31}) w_1^{i,j,k} \right] \\ & + \sum_{\alpha,\beta,\gamma=\pm 1} \left[\alpha \gamma \eta_x \eta_z (\tilde{e}_{15} - \tilde{e}_{31}) (w_1^{i,j,k+\gamma} - w_1^{i+\alpha,j,k}) \right] \\ & - \sum_{\alpha,\beta,\gamma=\pm 1} \left[\beta \gamma \eta_y \eta_z (\tilde{e}_{24} + \tilde{e}_{32}) w_2^{i,j,k} \right] \\ & + \sum_{\alpha,\beta,\gamma=\pm 1} \left[\beta \gamma \eta_y \eta_z (\tilde{e}_{24} - \tilde{e}_{32}) (w_2^{i,j,k+\gamma} - w_2^{i,j+\beta,k}) \right] \\ & - 2 \sum_{\alpha,\beta,\gamma=\pm 1} \left[\left(\frac{\Delta x_2^\beta \Delta x_3^\gamma}{\Delta x_1^\alpha} \tilde{e}_{15} + \frac{\Delta x_1^\alpha \Delta x_3^\gamma}{\Delta x_2^\beta} \tilde{e}_{24} + \frac{\Delta x_1^\alpha \Delta x_2^\beta}{\Delta x_3^\gamma} \tilde{e}_{33} \right) w_3^{i,j,k} \right] \\ & + 2 \sum_{\alpha,\beta,\gamma=\pm 1} \left[\Delta x_1^\alpha \Delta x_2^\beta \Delta x_3^\gamma \left(\frac{\tilde{e}_{15} w_3^{i+\alpha,j,k}}{(\Delta x_1^\alpha)^2} + \frac{\tilde{e}_{24} w_3^{i,j+\beta,k}}{(\Delta x_2^\beta)^2} + \frac{\tilde{e}_{33} w_3^{i,j,k+\gamma}}{(\Delta x_3^\gamma)^2} \right) \right] \end{aligned} \quad (27)$$

It should be noted that Eqs. .23-.25 are solved explicitly whereas Eq. .26 should be solved implicitly for induced potentials.

BIBLIOGRAPHY

- [1] Inman, D. J., Farrar, C. R., Lopes, V., and Steffen, V., *Damage Prognosis*, Wiley Online Library, 2005.
- [2] Maley, S., Plets, J., and Phan, N. D., “US Navy Roadmap to Structural Health and Usage Monitoring - The Present and Future,” *American Helicopter Society International 63rd Annual Forum - Riding the Wave of New Vertical Flight Technology*, Vol. 2, 2007, pp. 1456 – 1467.
- [3] Anonymous, “UH-60 Airframe Condition Evaluation (ACE) Technical Review,” Tech. rep., Aircraft Support Branch, Maintenance Engineering Division, Army Aviation and Missile Command, 2010.
- [4] Auld, B. A., *Acoustic Fields and Waves in Solids*, Wiley, New York, 1973.
- [5] Graff, K. F., *Wave Motion in Elastic Solids*, Dover Publications, New York, 1991.
- [6] Rose, J. L., *Ultrasonic Waves in Solid Media*, Cambridge University Press, 1999.
- [7] Achenbach, J. D., *Wave Propagation in Elastic Solids*, North-Holland Pub., 1984.
- [8] Doyle, J. F., *Wave Propagation in Structures: An FFT-based Spectral Analysis Methodology*, Springer-Verlag, New York, 1989.
- [9] Liu, G. R. and Xi, Z. C., *Elastic Waves in Anisotropic Laminates*, CRC Press, Boca Raton, FL, 2002.
- [10] Viktorov, I. A., *Rayleigh and Lamb waves: Physical Theory and Applications*, Plenum press, New York, 1967.
- [11] Zurn, B. and Mantell, S. C., “Nondestructive Evaluation of Laminated Composites Using Rayleigh Waves,” *Journal of Composite Materials*, Vol. 35, No. 12, 2001, pp. 1026 – 1044.
- [12] Herrmann, J., Kim, J. Y., Jacobs, L. J., Qu, J., Littles, J. W., and Savage, M. F., “Assessment of Material Damage in a Nickel-base Superalloy Using Nonlinear Rayleigh Surface Waves,” *Journal of Applied Physics*, Vol. 99, No. 12, 2006, pp. 124913 (1–9).

- [13] Matlack, K. H., Kim, J. Y., Jacobs, L. J., Qu, J., and Singh, P. M., “Nonlinear Rayleigh Waves to Detect Initial Damage Leading to Stress Corrosion Cracking in Carbon Steel,” *AIP Conference Proceedings*, Vol. 1430, USA, 2012, pp. 1452 – 1459.
- [14] Liu, M., Kim, J. Y., Jacobs, L., and Qu, J., “Experimental Study of Nonlinear Rayleigh Wave Propagation in Shot-peened Aluminum Plates-Feasibility of Measuring Residual Stress,” *NDT&E International*, Vol. 44, No. 1, 2011, pp. 67 – 74.
- [15] Pruell, C., Kim, J. Y., Qu, J., and Jacobs, L. J., “Evaluation of Fatigue Damage Using Nonlinear Guided Waves,” *Smart Materials and Structures*, Vol. 18, No. 3, 2009, pp. 035003 (1–7).
- [16] Walker, S. V., Kim, J. Y., Qu, Y., and Jacobs, L. J., “Fatigue Damage Evaluation in A36 Steel Using Nonlinear Rayleigh Surface Waves,” *NDT&E International*, Vol. 48, 2012, pp. 10 – 15.
- [17] Goueygou, M., Piwakowski, B., Fnine, A., Kaczmarek, M., and Buyle-Bodin, F., “NDE of Two-layered Mortar Samples Using High-frequency Rayleigh Waves,” *Ultrasonics*, Vol. 42, Granada, Spain, 2004, pp. 889 – 895.
- [18] Gazis, D. C., “Exact Analysis of the Plane-strain Vibrations of Thick-walled Hollow Cylinders,” *Journal of the Acoustical Society of America*, Vol. 30, No. 8, 1958, pp. 786 – 794.
- [19] Firestone, F. A. and Ling, D. S., “Method and Means for Generating and Utilizing Vibrational Waves in Plates,” Jan 1951, US Patent 2,536,128.
- [20] Firestone, F. A. and Ling, D. S., “Propagation of Waves in Plates,” Tech. rep., Sperry Products, Danbury, CT, USA, 1945.
- [21] Raghavan, A. and Cesnik, C. E. S., “Review of Guided-wave Structural Health Monitoring,” *Shock and Vibration Digest*, Vol. 39, No. 2, 2007, pp. 91 – 114.
- [22] Wilkie, W. K., Bryant, R. G., High, J. W., Fox, R. L., Hellbaum, R. F., Jalink, A. J., Little, B. D., and Mirick, P. H., “Low-cost Piezocomposite Actuator for Structural Control Applications,” *Smart Structures and Materials 2000: Industrial and Commercial Applications of Smart Structures Technologies*, Vol. 3991, 2000, pp. 323 – 334.
- [23] Matt, H. M. and Scalea, F. L., “Macro-fiber Composite Piezoelectric Rosettes for Acoustic Source Location in Complex Structures,” *Smart Materials and Structures*, Vol. 16, No. 4, 2007, pp. 1489 – 1499.
- [24] Liu, J., Wang, X., Yuan, S., and Li, G., “On Hilbert-Huang Transform Approach for Structural Health Monitoring,” *Journal of Intelligent Material Systems and Structures*, Vol. 17, 2006, pp. 721 – 728.

- [25] Yu, L., Giurgiutiu, V., and Kendall, J. R., “Omnidirectional Guided Wave PWAS Phased Array for Thin-wall Structure Damage Detection,” *Sensors and Smart Structures Technologies for Civil, Mechanical, and Aerospace Systems*, Vol. 6529, SPIE - The International Society for Optical Engineering, USA, 2007.
- [26] Fromme, P., Wilcox, P. D., Lowe, M., and Cawley, P., “On the Development and Testing of a Guided Ultrasonic Wave Array for Structural Integrity Monitoring,” *IEEE Transactions on Ultrasonics, Ferroelectrics and Frequency Control*, Vol. 53, No. 4, 2006, pp. 777 – 784.
- [27] Wilcox, P., Lowe, M., and Cawley, P., “Omnidirectional Guided Wave Inspection of Large Metallic Plate Structures using an EMAT Array,” *IEEE Transactions on Ultrasonics, Ferroelectrics and Frequency Control*, Vol. 52, No. 4, 2005, pp. 653 – 665.
- [28] Wilcox, P., Lowe, M., and Cawley, P., “Lamb and SH Wave Transducer Arrays for the Inspection of Large Areas of Thick Plates,” *Review of Progress in Quantitative Nondestructive Evaluation*, AIP, 2000, pp. 1049 – 1056.
- [29] Salas, K. I. and Cesnik, C. E. S., “CLOVER: An Alternative Concept for Damage Interrogation in Structural Health Monitoring Systems,” *Aeronautical Journal*, Vol. 113, No. 1144, 2009, pp. 339 – 356.
- [30] Salas, K. I. and Cesnik, C. E. S., “Guided Wave Structural Health Monitoring Using CLOVER Transducers in Composite Materials,” *Smart Materials and Structures*, Vol. 19, No. 1, 2010, pp. 015014 (1–25).
- [31] Nayfeh, A. H., “The General Problem of Elastic Wave Propagation in Multilayered Anisotropic Media,” *Journal of the Acoustical Society of America*, Vol. 89, No. 4, 1991, pp. 1521 – 1531.
- [32] Nayfeh, A. H. and Chimenti, D. E., “Free Wave Propagation in Plates of General Anisotropic Media,” *Journal of Applied Mechanics*, Vol. 56, No. 4, 1989, pp. 881 – 886.
- [33] Yuan, F. G. and Wang, L., “Group Velocity and Characteristic Wave Curves of Lamb Waves in Composites: Modeling and Experiments,” *Composites Science and Technology*, Vol. 67, No. 7-8, 2007, pp. 1370 – 1384.
- [34] Mindlin, R. D. and Yang, J., *An Introduction to the Mathematical Theory of Vibrations of Elastic Plates*, World Scientific, Hackensack, N.J., 2006.
- [35] Yang, P., Norris, C. H., and Stavsky, Y., “Elastic Wave Propagation in Heterogeneous Plates,” *International Journal of Solids and Structures*, Vol. 2, No. 4, 1966, pp. 665 – 684.
- [36] Lin, X. and Yuan, F. G., “Diagnostic Lamb Waves in an Integrated Piezoelectric Sensor/actuator Plate: Analytical and Experimental Studies,” *Smart Materials and Structures*, Vol. 10, No. 5, 2001, pp. 907 – 913.

- [37] Crawley, E. F. and Lazarus, K. B., “Induced Strain Actuation of Isotropic and Anisotropic Plates,” *AIAA Journal*, Vol. 29, No. 6, 1991, pp. 944 – 951.
- [38] Rose, L. R. F. and Wang, C. H., “Mindlin Plate Theory for Damage Detection: Source Solutions,” *Journal of the Acoustical Society of America*, Vol. 116, No. 1, 2004, pp. 154 – 171.
- [39] Rose, L. R. F. and Wang, C. H., “Mindlin Plate Theory for Damage Detection: Imaging of Flexural Inhomogeneities,” *Journal of the Acoustical Society of America*, Vol. 127, No. 2, 2010, pp. 754 – 763.
- [40] Whitney, J. M. and Sun, C. T., “A Higher Order Theory for Extensional Motion of Laminated Composites,” *Journal of Sound and Vibration*, Vol. 30, No. 1, 1973, pp. 85 – 97.
- [41] Reddy, J. N., “A Simple Higher-order Theory for Laminated Composite Plates,” *Transactions of the ASME. Journal of Applied Mechanics*, Vol. 51, No. 4, 1984, pp. 745 – 752.
- [42] Yang, S. and Yuan, F. G., “Transient Wave Propagation of Isotropic Plates using a Higher-order Plate Theory,” *International Journal of Solids and Structures*, Vol. 42, No. 14, 2005, pp. 4115 – 4153.
- [43] Lowe, M. J. S., “Matrix Techniques for Modeling Ultrasonic Waves in Multilayered Media,” *IEEE Transactions on Ultrasonics, Ferroelectrics, and Frequency Control*, Vol. 42, No. 4, 1995, pp. 525 – 542.
- [44] Sornette, D., Macon, L., and Coste, J., “Transfer Matrix Theory of Leaky Guided Waves,” *Journal de Physique*, Vol. 49, No. 10, 1988, pp. 1683 – 1689.
- [45] Lih, S. S. and Mal, A. K., “On the Accuracy of Approximate Plate Theories for Wave Field Calculations in Composite Laminates,” *Wave Motion*, Vol. 21, No. 1, 1995, pp. 17 – 34.
- [46] Raghavan, A. and Cesnik, C. E. S., “Finite-dimensional Piezoelectric Transducer Modeling for Guided Wave Based Structural Health Monitoring,” *Smart Materials and Structures*, Vol. 14, No. 6, 2005, pp. 1448 – 1461.
- [47] Nadella, K. S., Salas, K. I., and Cesnik, C. E. S., “Characterization of Guided-wave Propagation in Composite Plates,” *The Society of Photo-Optical Instrumentation Engineers (SPIE)*, Vol. 7650, San Diego, CA, United States, 2010.
- [48] Salas, K. I., Nadella, K. S., and Cesnik, C. E. S., “Characterization of Guided-wave Excitation and Propagation in Composite Plates,” *Proceedings of the 7th International Workshop on Structural Health Monitoring*, Vol. 1, 2009, pp. 651 – 658.
- [49] Lee, B. C. and Staszewski, W. J., “Modelling of Lamb Waves for Damage Detection in Metallic Structures: Part I. Wave Propagation,” *Smart Materials and Structures*, Vol. 12, No. 5, 2003, pp. 804 – 814.

- [50] Hildebrand, F. B., *Finite-difference Equations and Simulations*, Prentice-Hall, Englewood Cliffs, N.J., 1968.
- [51] Mitchell, A. R. and Griffiths, D. F., *The Finite Difference Method in Partial Differential Equations*, Wiley, Chichester [Eng.]; New York, 1980.
- [52] Baumeister, K. J. and USA, *Finite-difference Theory for Sound Propagation in a Lined Duct with Uniform Flow using the Wave Envelope Concept*, National Aeronautics and Space Administration, Scientific and Technical Information Office, Washington, Springfield, Va., 1977.
- [53] Levy, H. and Lessman, F., *Finite Difference Equations*, I. Pitman, London, 1959.
- [54] Strikwerda, J. C., *Finite Difference Schemes and Partial Differential Equations*, Wadsworth & Brooks/Cole Advanced Books & Software, Pacific Grove, Calif., 1989.
- [55] Virieux, J., “P-SV Wave Propagation in Heterogeneous Media: Velocity-stress Finite-difference Method,” *Geophysics*, Vol. 51, No. 4, 1986, pp. 889 – 901.
- [56] Bathe, K. J., *Finite element procedures*, Prentice Hall, Englewood Cliffs, N.J., 1996.
- [57] Ciarlet, P. G., *The Finite Element Method for Elliptic Problems*, North-Holland Pub. Co., New York, 1978.
- [58] Hughes, T. J. R., *The Finite Element Method: Linear Static and Dynamic Finite Element Analysis*, Dover Publications, Mineola, NY, 2000.
- [59] Brenner, S. C. and Scott, L. R., *The Mathematical Theory of Finite Element Methods*, Springer-Verlag, New York, 1994.
- [60] Zienkiewicz, O. C., Taylor, R. L., Zhu, J. Z., and Nithiarasu, P., *The Finite Element Method*, Elsevier Butterworth Heinemann, Burlington, Mass., 2005.
- [61] Ihlenburg, F., *Finite Element Analysis of Acoustic Scattering*, Springer, New York, 1998.
- [62] Panji, M., Kamalian, M., Marnani, J. A., and Jafari, M. K., “Transient Analysis of Wave Propagation Problems by Half-plane BEM,” *Geophysical Journal International*, Vol. 194, No. 3, 2013, pp. 1849 – 1865.
- [63] Chen, J. and Zhao, J., “Application of the Nearly Perfectly Matched Layer to Seismic-wave Propagation Modeling in Elastic Anisotropic Media,” *Bulletin of the Seismological Society of America*, Vol. 101, No. 6, 2011, pp. 2866 – 2871.
- [64] Toyokuni, G. and Takenaka, H., “Accurate and Efficient Modeling of Global Seismic Wave Propagation for an Attenuative Earth Model Including The Center,” *Physics of the Earth and Planetary Interiors*, Vol. 200 - 201, 2012, pp. 45 – 55.

- [65] Hall, F. and Wang, Y., “Elastic Wave Modelling by an Integrated Finite Difference Method,” *Geophysical Journal International*, Vol. 177, No. 1, 2009, pp. 104 – 114.
- [66] Petrov, P. V. and Newman, G. A., “3D Finite-difference Modeling of Elastic Wave Propagation in the Laplace-Fourier Domain,” *Geophysics*, Vol. 77, No. 4, 2012, pp. 137 – 155.
- [67] Delsanto, P. P., Schechter, R. S., Chaskelis, H. H., Mignogna, R. B., and Kline, R., “Connection Machine Simulation of Ultrasonic Wave Propagation in Materials. II: The Two-dimensional Case,” *Wave Motion*, Vol. 20, No. 4, 1994, pp. 295 – 314.
- [68] Subbaraj, K. and Dokainish, M. A., “A Survey of Direct Time-integration Methods in Computational Structural Dynamics. II. Implicit Methods,” *Computers and Structures*, Vol. 32, No. 6, 1989, pp. 1387 – 1401.
- [69] Dokainish, M. A. and Subbaraj, K., “A Survey of Direct Time-integration Methods in Computational Structural Dynamics. I. Explicit Methods,” *Computers and Structures*, Vol. 32, No. 6, 1989, pp. 1371 – 1386.
- [70] Idesman, A. V., Schmidt, M., and Foley, J. R., “Accurate 3-D Finite Element Simulation of Elastic Wave Propagation With the Combination of Explicit and Implicit Time-integration Methods,” *Wave Motion*, Vol. 48, No. 7, 2011, pp. 625 – 633.
- [71] Noh, G. and Bathe, K. J., “An Explicit Time Integration Scheme for the Analysis of Wave Propagations,” *Computers and Structures*, Vol. 129, 2013, pp. 178 – 193.
- [72] Brebbia, C. A., Telles, J. C. F., and Wrobel, L. C., *Boundary Element Techniques: Theory and Applications in Engineering*, Springer-Verlag, Berlin; New York, 1984.
- [73] Cho, Y. and Rose, J. L., “A Boundary Element Solution for a Mode Conversion Study on the Edge Reflection of Lamb Waves,” *Journal of the Acoustical Society of America*, Vol. 99, No. 4, 1996, pp. 2097 – 2109.
- [74] Galan, J. M. and Abascal, R., “Lamb Mode Conversion at Edges. A Hybrid Boundary Element-finite-element Solution,” *Journal of the Acoustical Society of America*, Vol. 117, No. 4 I, 2005, pp. 1777 – 1784.
- [75] Aimi, A., Diligenti, M., Frangi, A., and Guardasoni, C., “A Stable 3D Energetic Galerkin BEM Approach for Wave Propagation Interior Problems,” *Engineering Analysis with Boundary Elements*, Vol. 36, No. 12, 2012, pp. 1756 – 1765.
- [76] Rizos, D. C. and Zhou, S., “An Advanced Direct Time Domain BEM for 3-D Wave Propagation in Acoustic Media,” *Journal of Sound and Vibration*, Vol. 293, No. 1-2, 2006, pp. 196 – 212.
- [77] Israil, A. S. M. and Banerjee, P. K., “Two-dimensional Transient Wave-propagation Problems by Time-domain BEM,” *International Journal of Solids and Structures*, Vol. 26, No. 8, 1990, pp. 851 – 864.

- [78] Arias, I. and Achenbach, J. D., “Use of Reciprocity Considerations for the Two-dimensional BEM Analysis of Wave Propagation in an Elastic Half-space With Applications to Acoustic Emission,” *Wave Motion*, Vol. 39, No. 4, 2004, pp. 281 – 294.
- [79] Rizos, D. C. and Zhou, S., “An Advanced Direct Time Domain BEM for 3-D Wave Propagation in Acoustic Media,” *Journal of Sound and Vibration*, Vol. 293, No. 1-2, 2006, pp. 196 – 212.
- [80] Tadeu, A., Antonio, J., and Castro, I., “Coupling the BEM/TBEM and the MFS for the Numerical Simulation of Acoustic Wave Propagation,” *Engineering Analysis with Boundary Elements*, Vol. 34, No. 4, 2010, pp. 405 – 416.
- [81] Patera, A. T., “A Spectral Element Method for Fluid Dynamics: Laminar Flow in a Channel Expansion,” *Journal of Computational Physics*, Vol. 54, No. 3, 1984, pp. 468 – 488.
- [82] Narayanan, G. V. and Beskos, D. E., “Use of Dynamic Influence Coefficients in Forced Vibration Problems With the Aid of Fast Fourier Transform,” *Computers and Structures*, Vol. 9, No. 2, 1978, pp. 145 – 150.
- [83] Doyle, J. F., “A Spectrally Formulated Finite Element for Longitudinal Wave Propagation,” *International Journal of Analytical and Experimental Modal Analysis*, Vol. 3, 1988, pp. 1 – 5.
- [84] Martin, M., Gopalakrishnan, S., and Doyle, J. F., “Wave Propagation in Multiply Connected Deep Waveguides,” *Journal of Sound and Vibration*, Vol. 174, No. 4, 1994, pp. 521 – 538.
- [85] Mahapatra, R. D. and Gopalakrishnan, S., “A Spectral Finite Element Model for Analysis of Axial-flexural-shear Coupled Wave Propagation in Laminated Composite Beams,” *Composite Structures*, Vol. 59, No. 1, 2003, pp. 67 – 88.
- [86] Mahapatra, R. D., Gopalakrishnan, S., and Sankar, T. S., “Spectral-element-based Solutions for Wave Propagation Analysis of Multiply Connected Unsymmetric Laminated Composite Beams,” *Journal of Sound and Vibration*, Vol. 237, No. 5, 2000, pp. 819 – 836.
- [87] Krawczuk, M., Palacz, M., and Ostachowicz, W., “The Dynamic Analysis of a Cracked Timoshenko Beam by the Spectral Element Method,” *Journal of Sound and Vibration*, Vol. 264, No. 5, 2003, pp. 1139 – 1153.
- [88] Gopalakrishnan, S., Chakraborty, A., and Mahapatra, D. R., *Spectral Finite Element Method: Wave Propagation, Diagnostics and Control in Anisotropic and Inhomogeneous Structures*, Springer, 2008.
- [89] Ostachowicz, W., Kudela, P., Krawczuk, M., and Zak, A., *Spectral Finite Element Method*, John Wiley & Sons, Ltd, 2012, pp. 47 – 92.

- [90] Stepinski, T., Uhl, T., and Staszewski, W. J., *Advanced Structural Damage Detection*, chap. Numerical Simulation of Elastic Wave Propagation, John Wiley & Sons, Ltd, 2013, pp. 17 – 56.
- [91] Delsanto, P. P., Whitcombe, T., Chaskelis, H. H., and Mignogna, R. B., “Connection Machine Simulation of Ultrasonic Wave Propagation in Materials. I. The One-dimensional Case,” *Wave Motion*, Vol. 16, No. 1, 1992, pp. 65 – 80.
- [92] Delsanto, P. P., Schechter, R. S., and Mignogna, R. B., “Connection Machine Simulation of Ultrasonic Wave Propagation in Materials. III. The Three-dimensional Case,” *Wave Motion*, Vol. 26, No. 4, 1997, pp. 329 – 339.
- [93] Agostini, V., Baboux, J. C., Delsanto, P. P., Monnier, T., and Olivero, D., “Application of Lamb Waves for the Characterization of Composite Plates,” *AIP Conference Proceedings*, No. 497, 1999, pp. 455 – 460.
- [94] Agostini, V., Delsanto, P. P., Genesisio, I., and Olivero, D., “Simulation of Lamb Wave Propagation for the Characterization of Complex Structures,” *IEEE Transactions on Ultrasonics, Ferroelectrics and Frequency Control*, Vol. 50, No. 4, 2003, pp. 441 – 448.
- [95] Lee, B. C. and Staszewski, W. J., “Modelling of Lamb Waves for Damage Detection in Metallic Structures: Part II. Wave Interactions With Damage,” *Smart Materials and Structures*, Vol. 12, No. 5, 2003, pp. 815 – 824.
- [96] Ruzzene, M., Jeong, S. M., Michaels, T. E., Michaels, J. E., and Mi, B., “Simulation and Measurement of Ultrasonic Waves in Elastic Plates Using Laser Vibrometry,” *AIP Conference Proceedings*, No. 760, 2005, pp. 172 – 179.
- [97] Dobie, G., Spencer, A., Burnham, K., Pierce, G. S., Worden, K., Galbraith, W., and Hayward, G., “Simulation of Ultrasonic Lamb Wave Generation, Propagation and Detection for a Reconfigurable Air Coupled Scanner,” *Ultrasonics*, Vol. 51, No. 3, 2011, pp. 258 – 269.
- [98] Borkowski, L., Fard, M. Y., and Chattopadhyay, A., “Modeling Lamb Wave Propagation for Damage Detection in a Complex Metallic Aerospace Structural Component,” *53rd AIAA/ASME/ASCE/AHS/ASC Structures, Structural Dynamics and Materials Conference*, Honolulu, HI, United States, 2012.
- [99] Spencer, A. B., Worden, K., Staszewski, W. J., Rongong, J. A., and Sims, N. D., “An Optimisation Scheme Based on the Local Interaction Simulation Approach and Lamb Waves for Elastic Property Estimation in Multi-layered Composites,” *Shock and Vibration*, Vol. 19, No. 5, 2012, pp. 1027 – 1040.
- [100] Stepinski, T., Ambrozinski, L., and Uhl, T., “Designing 2D Arrays for SHM of Planar Structures: A Review,” *Proceedings of the SPIE - The International Society for Optical Engineering*, Vol. 8694, USA, 2013, pp. 86941R (1–12).

- [101] Hirsekorn, M., Delsanto, P. P., Batra, N. K., and Matic, P., “Modelling and Simulation of Acoustic Wave Propagation in Locally Resonant Sonic Materials,” *Ultrasonics*, Vol. 42, No. 1-9, 2004, pp. 231 – 235.
- [102] Scalerandi, M., Agostini, V., Delsanto, P. P., Abeele, V. D. K., and Johnson, P. A., “Local Interaction Simulation Approach to Modelling Nonclassical, Nonlinear Elastic Behavior in Solids,” *Journal of the Acoustical Society of America*, Vol. 113, No. 6, 2003, pp. 3049 – 3059.
- [103] Scalerandi, M., Pescarmona, G. P., Delsanto, P. P., and Sansone, C. B., “Local Interaction Simulation Approach for the Response of the Vascular System to Metabolic Changes of Cell Behavior,” *Physical Review E - Statistical, Nonlinear, and Soft Matter Physics*, Vol. 63, No. 1, 2001, pp. 011901 (1–9).
- [104] Scalerandi, M. and Agostini, V., “Simulation of the Propagation of Ultrasonic Pulses in Nonlinear and/or Attenuative Media,” *Journal of Computational Acoustics*, Vol. 10, No. 3, 2002, pp. 275 – 294.
- [105] Scalerandi, M., Delsanto, P. P., and Pirri, C. F., “A Local Interaction Simulation Approach to the Analysis of Thin-film Growth,” *Philosophical Magazine B*, Vol. 80, No. 4, 2000, pp. 507 – 514.
- [106] Sundararaman, S. and Adams, D. E., “Modeling Guided Waves for Damage Identification in Isotropic and Orthotropic Plates Using a Local Interaction Simulation Approach,” *Journal of Vibration and Acoustics*, Vol. 130, No. 4, 2008, pp. 041009 (1–16).
- [107] Moore, G. E., “Cramming More Components onto Integrated Circuits,” *Proceedings of the IEEE*, Vol. 86, No. 1, 1998, pp. 82 – 85.
- [108] Prasad, R. P., “End of an Era: Moore’s Law,” *SMT Surface Mount Technology Magazine*, Vol. 18, No. 7, 2004.
- [109] Courtland, R., “The End of the Shrink (Keeping up With Moore’ Law),” *IEEE Spectrum*, Vol. 50, No. 11, 2013, pp. 26 – 29.
- [110] Owens, J. D., Houston, M., Luebke, D., Green, S., Stone, J. E., and Phillips, J. C., “GPU Computing,” *Proceedings of the IEEE*, Vol. 96, No. 5, 2008, pp. 879 – 899.
- [111] Huaguo, Y., Xingwu, H., and Honglin, Z., “Ultrasound Pulsed Wave Doppler Based on CUDA,” *Computer Engineering and Applications*, Vol. 48, No. 19, 2012, pp. 140 – 144.
- [112] Breitbart, J. and Tsitouras, C. E., “An Exploration of CUDA and CBEA for Gravitational Wave Data-analysis,” *AIP Conference Proceedings*, Vol. 1168, USA, 2009, pp. 1065 – 1067.

- [113] Campos, S. R., Amorim, M. R., Oliveira, B. L., Rocha, B. M., Sundnes, J., Barra, D. L. P., Lobosco, M., and Santos, W. R., “3D Heart Modeling with Cellular Automata, Mass-Spring System and CUDA,” *Parallel Computing Technologies. 12th International Conference, PaCT 2013.*, Berlin, Germany, 2013, pp. 296 – 309.
- [114] Webb, C. J. and Bilbao, S., “Computing Room Acoustics with CUDA 3D FDTD Schemes With Boundary Losses and Viscosity,” *2011 IEEE International Conference on Acoustics, Speech and Signal Processing (ICASSP)*, Piscataway, NJ, USA, 2011, pp. 317 – 320.
- [115] Micikevicius, P., “3D Finite Difference Computation on GPUs using CUDA,” *Proceedings of 2nd Workshop on General Purpose Processing on Graphics Processing Units, GPGPU-2*, Washington, D.C., United States, 2009, pp. 79 – 84.
- [116] Komatitsch, D., Michea, D., and Erlebacher, G., “Porting a High-order Finite-element Earthquake Modeling Application to NVIDIA Graphics Cards using CUDA,” *Journal of Parallel and Distributed Computing*, Vol. 69, No. 5, 2009, pp. 451 – 460.
- [117] Bielak, T., Packo, P., Spencer, A., Staszewski, W. J., Uhl, T., and Worden, K., “CUDA Technology for Lamb Wave Simulations,” Vol. 7984, San Diego, CA, United States, 2011, pp. 79842Z (1–8).
- [118] Paćko, P., Bielak, T., Spencer, A. B., Staszewski, W. J., Uhl, T., and Worden, K., “Lamb Wave Propagation Modelling and Simulation using Parallel Processing Architecture and Graphical Cards,” *Smart Materials and Structures*, Vol. 21, No. 7, 2012, pp. 075001 (1–13).
- [119] Sinor, M., “Numerical Modelling and Visualisation of Elastic Wave Propagation in Arbitrary Complex Media,” *Proceedings of the Eighth Workshop on Multimedia in Physics Teaching and Learning of the European Physical Society*, 2004.
- [120] Alleyne, D. N., *The Nondestructive Testing of Plates Using Ultrasonic Lamb Waves*, Thesis, Imperial College of Science, Technology and Medicine, 1991.
- [121] Lee, B. C. and Staszewski, W. J., “Lamb Wave Propagation Modelling for Damage Detection: I. Two-dimensional Analysis,” *Smart Materials and Structures*, Vol. 16, No. 2, 2007, pp. 249 – 259.
- [122] Nadella, K. S. and Cesnik, C. E. S., “Local Interaction Simulation Approach for Modeling Wave Propagation in Composite Structures,” *CEAS Aeronautical Journal*, Vol. 4, No. 1, 2013, pp. 35 – 48.
- [123] Crawley, E. F. and Luis, D. J., “Use of Piezoelectric Actuators as Elements of Intelligent Structures,” *AIAA Journal*, Vol. 25, No. 10, 1987, pp. 1373 – 1385.
- [124] Sundararaman, S. and Adams, D. E., “Accuracy and Convergence Using a Local Interaction Simulation Approach in One, Two, and Three Dimensions,” *Journal of Applied Mechanics, Transactions ASME*, Vol. 76, No. 3, 2009, pp. 031008 (1–10).

- [125] Tiersten, H. F., “Hamilton’s Principle for Linear Piezoelectric Media,” *Proceedings of the IEEE*, Vol. 55, No. 8, 1967, pp. 1523 – 1524.
- [126] Nadella, K. S. and Cesnik, C. E. S., “Piezoelectric Coupled LISA for Guided Wave Generation and Propagation,” *Proceedings of SPIE - The International Society for Optical Engineering*, Vol. 8695, 2013, pp. 86951R (1–16).
- [127] Anonymous, “An American National Standard-IEEE Standard on Piezoelectricity,” *IEEE Transactions on Sonics and Ultrasonics*, Vol. 31, No. 2, 1984, pp. 1 – 55.
- [128] Delsanto, P. P. and Scalerandi, M., “A Spring Model for the Simulation of the Propagation of Ultrasonic Pulses Through Imperfect Contact Interfaces,” *The Journal of the Acoustical Society of America*, Vol. 104, No. 5, 1998, pp. 2584–2591.
- [129] P., D. P., Gliozzi, A. S., Hirsekorn, M., and M, N., “A 2D Spring Model for the Simulation of Ultrasonic Wave Propagation in Nonlinear Hysteretic Media,” *Ultrasonics*, Vol. 44, No. 3, 2006, pp. 279 – 286.
- [130] Shannon, C. E., “Communication in the Presence of Noise,” *Proceedings of the IRE*, Vol. 37, No. 1, 1949, pp. 10 – 21.
- [131] Iordache, D., Delsanto, P. P., and Scalerandi, M., “Pulse Distortions in the FD Simulation of Elastic Wave Propagation,” *Mathematical and Computer Modelling*, Vol. 25, No. 6, 1997, pp. 31 – 43.
- [132] Harker, A. H., “Numerical Modelling of the Scattering of Elastic Waves in Plates,” *Journal of Nondestructive Evaluation*, Vol. 4, No. 2, 1984, pp. 89–106.
- [133] “CYCOM 977-3 Epoxy Resin System,” Technical data sheet, Cytec Engineered Materials, 2012.
- [134] Company, G. P. M., “FR-6710 product data sheet. Technical report,” Tech. rep., 2006.
- [135] Ji, W., *Static and Dynamic Response of a Sandwich Structure Under Axial Compression*, Ph.D. thesis, The University of Michigan, Ann Arbor, Michigan, 2008.
- [136] Obenchain, M. B. and Cesnik, C. E. S., “Producing Accurate Wave Propagation Time Histories Using the Global Matrix Method,” *Smart Materials and Structures*, Vol. 22, No. 12, 2013, pp. 125024 (1–11).